CALT-68-1920
DOE RESEARCH AND
DEVELOPMENT REPORT

A Measurement of the Mass of the Tau Lepton

Thesis by

Lawrence Aston Jones

In Partial Fulfillment of the Requirements

for the Degree of

Doctor of Philosophy

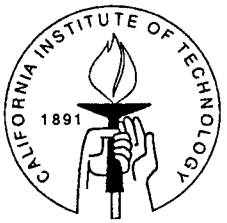

California Institute of Technology

Pasadena, California

1995

(Submitted October 4, 1994)

Acknowledgments

Many people have been of great, even essential, help in the production of this thesis. I would like to thank all the members of the BES Collaboration and the BEPC staff. It has been a privilege to work with the team. In addition, there are a few individuals I would like to mention.

My advisor, Frank Porter, has been a source of encouragement and experience. I greatly appreciate the independence he allowed me and the support he provided.

My office mates, Michael Kelsey and Ernest Prabhakar, have been invaluable in helping me along the road despite its many detours, circuitous routes, and dead-ends. Many of the ideas in this thesis would not be here without them.

My colleagues—Jim Panetta, Makoto Hatanaka, Bob Nolty, James Oyang, Eric Soderstrom, Helmut Marsiske, David Hitlin, Walter Toki, and Bill Dunwoodie—have provided many hours of useful discussion and have been a source of inspiration and constructive criticism.

I formed many friendships in China in the course of working on this experiment. Liu Ye, Yao Hongbin, Li Yushan, Ma Donghong, Hu Tao, and Li Fang all provided a new perspective on life and work, for which I am very grateful.

Man does not live by work alone. My friends and family provided the support and enthusiasm I needed to keep working and a place to relax when I didn't.

Last, but never least, my wife, Erin, has been the source of all my hope, the alleviator of all my fears, a friend, a partner, and a soul mate. The time, assistance, and love she has lavished on me are irreplaceable. This thesis is dedicated to her:

"All these things I would share with you ..."

Abstract

For a conventional charged lepton l under the Standard Model, the electronic branching ratio B_l^e, lifetime τ_l, mass m_l, the dimensionless weak coupling constant g_l and the W-boson mass m_W are related by $B_l^e/\tau_l = g_l^2 g_e^2 m_l^5/6144\pi^3 m_W^4$ up to small radiative and electroweak corrections. This implies the following relationship among the above parameters for the τ and μ leptons: $g_\tau^2/g_\mu^2 = m_\mu^5 B_\tau^e \tau_\mu / m_\tau^5 B_\mu^e \tau_\tau$. In 1992, world averages for the above quantities yielded $g_\tau^2/g_\mu^2 = 0.941 \pm 0.025$, implying a 2.4 standard deviation disagreement with lepton universality.

A measurement of the $\tau^+\tau^-$ production cross section in the region most sensitive to the τ mass—a few MeV around threshold—provides the opportunity to measure the τ mass with greatly improved precision. This thesis presents such a measurement made using the Beijing Spectrometer at the Beijing Electron Positron Collider.

A search was conducted for threshold assuming a parameterized form for the $\tau^+\tau^-$ cross section. After each search point a likelihood was generated using all the information from the search so far. This identified the energy where it would be most efficient to search next. The mass value is obtained from a fit to the energy dependence of the cross section. The measurement is independent of the ν_τ mass.

A likelihood-driven search was carried out at BES based on $e\mu$ events. The data has been re-analysed to take into account the additional decay modes ee, $e\pi$, $\mu\mu$, $\mu\pi$, and $\pi\pi$. This new analysis yields $m_\tau = 1776.87^{+0.20+0.22}_{-0.22-0.18}$ MeV.

Using contemporary values for B_τ^e and τ_τ and the result above, the ratio of the weak coupling constants becomes $g_\tau^2/g_\mu^2 = 1.001 \pm 0.012$, and lepton universality is supported.

Table of Contents

List of Figures

List of Tables

Part I
Introduction

"I can trace my ancestry back to a proto-plasmal primordial atomic globule. Consequently, my family pride is something inconceivable."

W. S. Gilbert
The Mikado

Chapter 1 The Standard Model

Section 1.1 Fermions and Bosons

A boson is any particle whose spin quantum number is an integer. A fermion is any particle whose spin quantum number is half of an odd integer. The Standard Model* requires twelve fundamental fermions which constitute matter and twelve fundamental bosons which transmit three of the four forces via which matter interacts.† The three forces are designated electromagnetic, weak, and strong. In addition there is an extra fundamental boson, the Higgs boson, which is responsible for the existence of mass.

Of the fermions, six have not only electrical and weak charges, but also a charge associated with the strong force referred to as colour. These six are called quarks. The strong force has three different types of charges denoted red, green, and blue. To present knowledge quarks exist in nature in all three colours in equal numbers but are never uncharged. Hence they always experience the strong force. The six quarks are

$$\begin{pmatrix} u \\ d \end{pmatrix}, \begin{pmatrix} c \\ s \end{pmatrix}, \begin{pmatrix} t \\ b \end{pmatrix}. \tag{1.1}$$

The remaining six, the leptons, have no colour charge and hence do not experience the strong force. The three electrically neutral leptons, the neutrinos ν, experience

---

⋆ Throughout this thesis the phrase "Standard Model" will refer to the Minimal Standard Model unless explicitly noted otherwise.

† The Standard Model does not describe the fourth force, gravity, but on this scale it is so weak as to have negligible effect.

only the weak force; the other three experience both the weak and electromagnetic forces. The six leptons are

$$\binom{\nu_e}{e}, \binom{\nu_\mu}{\mu}, \binom{\nu_\tau}{\tau}. \tag{1.2}$$

The quarks and leptons are grouped into the three known generations on the basis of SU(2) doublets (see Section 1.2). Strong evidence exists that there are no more low mass generations to be discovered.[1,2]

The twelve spin 1 messenger particles are: the photon γ mediating the electromagnetic force, three mediators of the weak force W^+, W^-, and Z^0, and an octet of gluons $\{g\}$ to mediate the strong force. The remaining boson has spin 0 and derives from a complex Higgs doublet $\phi = \binom{\phi^+}{\phi^0}$.

To date only the Higgs boson and the tau neutrino have escaped direct detection. There is, however, extreme evidence in favour of the Higgs boson‡ from the existence of mass, and for the tau neutrino in the form of energy conservation for tau decay.

Additionally, evidence for the existence of the top quark t has only recently been presented by the CDF Collaboration.[3] Their statistics are very low and the evidence is quite weak. Nevertheless interpreting their data as top quark decays they find a value for m_t of $174 \pm 10^{+13}_{-12}$ GeV which is within the expected theoretical range.

Section 1.2 Fundamental Parameters

The interactions between the fermions and bosons can be represented in the form of a Lagrangian. This thesis will mainly be concerned with the electromagnetic and weak

‡ Not necessarily in its minimal form.

(electroweak) interactions between the fermions and the bosons, *i.e.*, we will ignore gluonic (strong) interactions. The Lagrangian for the electroweak portion of the Standard Model $(\mathrm{SU}(2)_L \times \mathrm{U}(1)_Y)$, after spontaneous symmetry breaking, is shown below:

$$\begin{aligned}
\mathcal{L}_F = & \sum_i \bar{\psi}_i \Big(i\partial\!\!\!/ - m_i - \frac{g m_i H}{2 m_W} \Big) \psi_i \\
& - \sum_i \frac{g}{2\sqrt{2}} \bar{\psi}_i \gamma^\mu (1 - \gamma^5)(T^+ W_\mu^+ + T^- W_\mu^-) \psi_i \\
& - \sum_i e q_i \bar{\psi}_i \gamma^\mu \psi_i A_\mu \\
& - \sum_i \frac{g}{2 \cos\theta_W} \bar{\psi}_i \gamma^\mu (V^i - A^i \gamma^5) \psi_i Z_\mu
\end{aligned} \tag{1.3}$$

where ψ_i are $\binom{\nu_i}{l_i^-}$ and $\binom{u_i}{d_i'}$, the i^{th} fermion family, and where $g \sin\theta_W = e$.[§] The ψ_i vectors transform as SU(2) doublets and the d_i' are related to the d_i of Equation (1.1) via $d_i' = \sum_j V_{ij} d_j$ where V is the Cabibbo-Kobayashi-Maskawa (CKM) mixing matrix. T^+ and T^- are the weak isospin raising and lowering operators, and the vector and axial couplings, V^i and A^i, are given by

$$\begin{aligned}
V^i &= t_{3L}(i) - 2 q_i \sin^2\theta_W \\
A^i &= t_{3L}(i)
\end{aligned} \tag{1.4}$$

where $t_{3L}(i)$ is the weak isospin of fermion i and q_i is the charge of ψ_i in units of e.[4]

The q_i and $t_{3L}(i)$ are known. Other than those, the above portion of the Standard Model requires seventeen independent parameters: twelve are the masses of the fermions m_i, four parameterize the CKM matrix, the remaining three are m_W the

§ Note that g here is a coupling constant, not to be confused with the octet of gluons $\{g\}$ on page 3.

mass of the W-boson, θ_W the electromagnetic-weak mixing angle, and g the weak coupling constant. m_Z can be defined in terms of m_W and θ_W; $e = g \sin\theta_W$ as noted above.

This thesis will not investigate the masses of the quarks or the electroweak parameters, m_W and θ_W. g will be of interest when I investigate lepton universality in Section 1.3.

The Minimal Standard Model requires that all the neutrinos are massless. The experimental limits on the masses in 1992 were:

$$\begin{aligned} m_{\nu_e} &< 5.1 \text{ eV at a 95\% confidence level;}^{[4]} \\ m_{\nu_\mu} &< 0.27 \text{ MeV at a 90\% confidence level;}^{[5]} \\ m_{\nu_\tau} &< 35 \text{ MeV at a 95\% confidence level.}^{[6]} \end{aligned} \tag{1.5}$$

This leaves the three massive leptons, the electron e, the muon μ, and the tau τ. The 1992 Review of Particle Properties[4] quoted the uncertainties on the masses of the electron and the muon as approximately 3×10^{-5}%. In contrast, the value for the tau mass was $m_\tau = 1784.1^{+2.7}_{-3.6}$ MeV, *i.e.*, an uncertainty of 0.15 to 0.2%. This thesis will not investigate m_e or m_μ. However, estimates given in Chapter 6 show that we can expect to achieve uncertainties of the order of a few tenths of an MeV for m_τ. The opportunity to reduce the errors on a fundamental parameter of the Standard Model by almost an order of magnitude is one motivation for this experiment.

Section 1.3 Lepton Universality

An application of smaller uncertainties on the tau mass can be found in the study of lepton universality: assume for the moment that g in Equation (1.3) is different for

each lepton family l, *i.e.*, g becomes g_l. Then consider the decay $l \rightarrow e\bar{\nu}_e\nu_l$ where one of the decay products has a small mass m and the others are massless.

For a conventional charged lepton l under the Standard Model the width Γ_l for such a decay can be calculated as[7,8]:

$$\Gamma_l = \frac{g_l^2 g_e^2 m_l^5}{6144\pi^3 m_W^4} f(y_l) \tag{1.6}$$

where m_l is the lepton mass, $y_l = m^2/m_l^2$ and

$$f(y) = 1 - 8y + 8y^3 - y^4 - 12y^2 \ln y \ . \tag{1.7}$$

Note that $f(y)$ approaches one monotonically as y approaches zero.

The limit on m_{ν_τ} is larger than the electron mass m_e. So for τ decay one equates m with m_{ν_τ} and approximates the electron mass as zero. For μ decay, however, m_e is larger than the limit on m_{ν_μ}, and so one assumes the muon neutrino is massless and puts $m = m_e$, *i.e.*, $y_\tau = m_{\nu_\tau}^2/m_\tau^2$ whereas $y_\mu = m_e^2/m_\mu^2$.

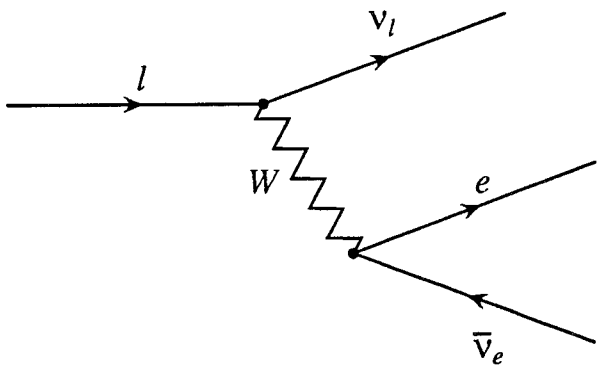

Figure 1.1 Standard Model decay $l \rightarrow e\bar{\nu}_e\nu_l$

Adding in electroweak and radiative corrections implies[8]:

$$\Gamma_l = \frac{g_l^2 g_e^2 m_l^5}{6144\pi^3 m_W^4}\left(1+\frac{3m_l^2}{5m_W^2}\right)\left(1+\frac{\alpha(m_l)}{2\pi}\left(\frac{25}{4}-\pi^2\right)\right)f(y_l) \tag{1.8}$$

and using $\Gamma_l = B_l^e/\tau_l$ yields

$$\frac{B_l^e}{\tau_l} = \frac{g_l^2 g_e^2 m_l^5}{6144\pi^3 m_W^4}\left(1+\frac{3m_l^2}{5m_W^2}\right)\left(1+\frac{\alpha(m_l)}{2\pi}\left(\frac{25}{4}-\pi^2\right)\right)f(y_l)\,. \tag{1.9}$$

This implies the following relationship among the above parameters for the τ and μ leptons:

$$\frac{g_\tau^2}{g_\mu^2} = \frac{m_\mu^5 B_\tau^e \tau_\mu f(y_\mu)}{m_\tau^5 B_\mu^e \tau_\tau f(y_\tau)}\left(\frac{1+3m_\mu^2/5m_W^2}{1+3m_\tau^2/5m_W^2}\right)\left(\frac{1+\alpha(m_\mu)(25/8\pi-\pi/2)}{1+\alpha(m_\tau)(25/8\pi-\pi/2)}\right)\,. \tag{1.10}$$

Using 1992 world averages,[4] $m_\mu = 105.658389$ MeV, $m_\tau = 1784.1$ MeV, and $m_W = 80.22$ GeV, one finds

$$\frac{1+3m_\mu^2/5m_W^2}{1+3m_\tau^2/5m_W^2} - 1 \approx -2.96\times 10^{-4} \tag{1.11}$$

and

$$\frac{1+\alpha(m_\mu)(25/8\pi-\pi/2)}{1+\alpha(m_\tau)(25/8\pi-\pi/2)} - 1 \approx 1.62\times 10^{-4}. \tag{1.12}$$

Also $B_\mu^e - 1 \approx -3.4\times 10^{-5}$ and $m_e = 0.51099906$ MeV which yields $f(y_\mu) - 1 \approx -1.87\times 10^{-4}$. These terms can all be approximated to one with negligible error. Hence Equation (1.10) becomes:

$$\frac{g_\tau^2}{g_\mu^2} = \frac{m_\mu^5 B_\tau^e \tau_\mu}{m_\tau^5 \tau_\tau f(y_\tau)}\,. \tag{1.13}$$

Assuming a massless tau neutrino and utilizing 1992 world averages for the other quantities above, $m_\mu = 105.658389 \pm 0.000034$ MeV, $\tau_\mu = 2.19703 \pm 0.00004$ μs,

$m_\tau = 1784.1^{+2.7}_{-3.6}$ MeV, $\tau_\tau = 0.305 \pm 0.006$ ps, and $B^e_\tau = 17.93 \pm 0.26\%$, yields

$$g^2_\tau / g^2_\mu = 0.941 \pm 0.025. \tag{1.14}$$

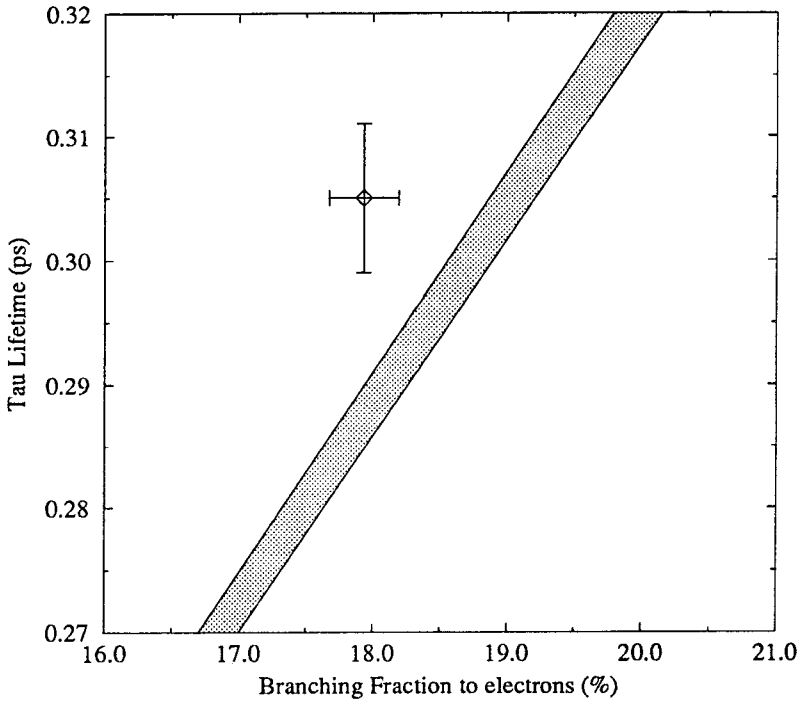

Figure 1.2 The variation of τ_τ with B^e_τ for $m_\tau = 1784.1^{+2.7}_{-3.6}$ MeV compared with the 1992 world average values.

In actuality the Minimal Standard Model allows only one parameter g and requires $g_\tau = g_\mu = g$. The above calculation represents a 2.4 standard deviation disagreement with lepton universality. Figure 1.2 shows this disagreement by plotting the region allowed for τ_τ and B^e_τ for values of m_τ within one standard deviation of 1784.1 MeV. The point with error bars shows the 1992 world average values for τ_τ and B^e_τ for comparison.

Note, however, that the tau neutrino need not be massless. If m_{ν_τ} has its maximum 1992 value of 35 MeV then $f(y_\tau) = 0.997$ and $g_\tau^2/g_\mu^2 = 0.944 \pm 0.025$. This would represent a 2.3 standard deviation difference.

The uncertainty on the value of the tau mass contributes approximately 38% of the uncertainty in g_τ^2/g_μ^2. Hence a more accurate measurement of the tau lepton mass would provide a better measurement of the disagreement with the Standard Model.

Chapter 2 The Tau Lepton

Section 2.1 Discovery and Brief History

The possibility of a third, heavier, sequential lepton was investigated in detail by Y. S. Tsai[9] in 1971. He predicted decay correlations and branching fractions dependent on the lepton's mass. The first experimental confirmation of its existence took place in 1975 using the Magnetic Detector[10] (Mark I) and the SPEAR storage ring at the Stanford Linear Accelerator Center (SLAC): M. L. Perl *et al.*[11] observed 64 "anomalous events" of the form

$$e^+e^- \rightarrow e^\pm\mu^\mp + \text{missing energy.} \tag{2.1}$$

Several supporting experiments[12–16] followed and, at the same time, various explanations for these events were proposed. Chief among these were that the events derived from the formation and subsequent decay of

1. a heavy, sequential lepton with its own conserved lepton number, or
2. a vector meson.

Analyses of the data from these experiments confirmed hypothesis 1[17–19] and the name of the new lepton, the τ, was proposed in August 1977.[20]

Measurements of some of the decay modes of the tau lepton and a more precise determination of its mass were taken by Brandelik *et al.*[21] at the DASP experiment in 1978. This was followed by further refinements of the mass in the same year via two separate experiments—the DESY[22] experiment at the DORIS storage ring in Ger-

many and the DELCO[23] experiment at SPEAR. Until 1992 this latter measurement dominated the world average.

In addition to the mass, many other properties of the τ were documented: the tau lifetime,[25-42] the Michel parameters,[43-48] limits on the tau neutrino mass,[49-56] and many measurements of various branching fractions. This last brought to light a problem: that the sum of the exclusive one-prong* branching fractions does not equal the inclusive one-prong branching fraction when theoretical predictions are used for the unmeasured modes.[57-63] This problem appears to have been resolved in the latest data from ALEPH[64] and CELLO[65] taken jointly or individually, however the world average still shows this effect.[66]

Section 2.2 The Tau Mass

This thesis will be concerned solely with a measurement of the mass of the tau lepton. The tau mass is used in all experiments which limit the tau neutrino mass m_{ν_τ}. Hence the mass reported by this thesis will affect those limits. No attempt will be made here to re-analyse other collaborations' data to establish a new limit for m_{ν_τ}.

However, the coupling constant ratio g_τ^2/g_μ^2 depends on m_{ν_τ} through $f(y_\tau)$ (see Equation (1.13)). Hence any deviations from lepton universality depend upon assumptions for m_{ν_τ}. I will present the value of g_τ^2/g_μ^2 as a function of m_{ν_τ} in Section 9.2.

---

* A "prong" is defined as a charged track.

Part II
Experimental Details

"Man is a tool–using animal ...
Without tools he is nothing, with tools he is all."

Thomas Carlyle
Sartor Resartus

Chapter 3 The BEPC Accelerator

Section 3.1 Overview

Construction of the Beijing Electron Positron Collider (BEPC) was begun in October, 1984 and the first e^+e^- collisions took place in 1988. It resides at the Institute for High Energy Physics (IHEP) in Beijing.

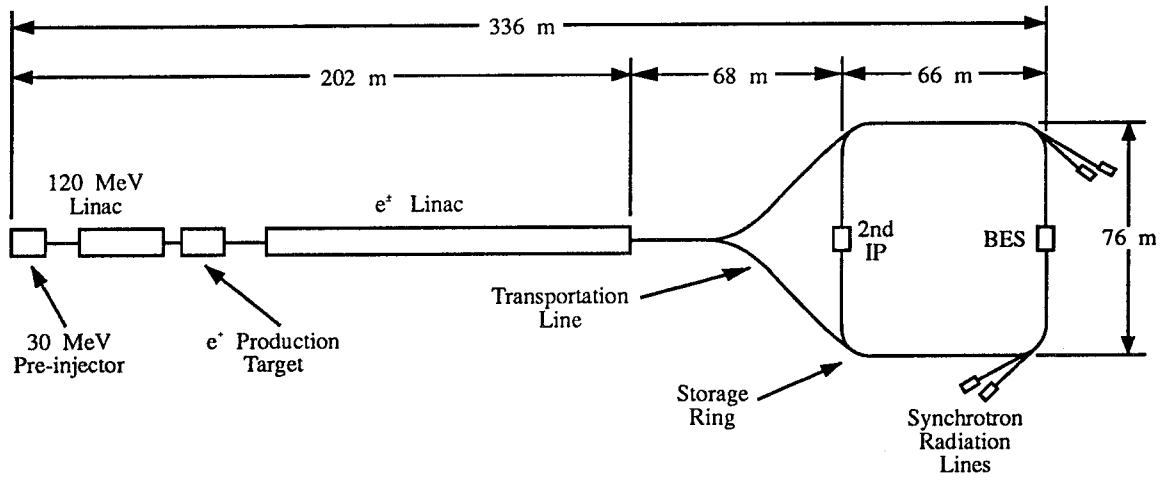

Figure 3.1 Schematic diagram of the BEPC accelerator and storage ring

BEPC is a 202 m linear acclerator feeding a stadium shaped storage ring[67] as shown in Figure 3.1 above. In the storage ring a localized group of electrons (called a bunch) and a similar group of positrons are made to circulate in opposite directions following orbits defined by magnetic fields at various points around the ring. Energy lost through synchrotron radiation in the bending magnets is replaced via electromagnetic fields in two radio-frequency (RF) cavities around the ring where the variation of the fields is timed to coincide with the passage of the bunches. At the

BES interaction point (IP) the two bunches are brought into collision and the BES detector records the results.

The storage ring operates in the 3 to 5 GeV centre of mass energy region making it ideal for studying tau and charm physics. Some operating parameters are shown in Tables 3.1 and 3.2.

Parameter	Symbol	Value	Units
Centre of mass energy	E	3 - 5	GeV
Storage ring circumference	L	240.400	m
Bunch spacing	t_b	801.888	ns
Number of bunches	N	1	
Natural bunch length	σ_l	5.20	cm
Number of particles per bunch at injection	N_b	6.8×10^{10}	
Revolution frequency	f_0	1247.057	kHz
Horizontal beta function at IP	β_x^*	103.00	cm
Vertical beta function at IP	β_y^*	8.50	cm
Horizontal spot size at IP	σ_x^*	592	μm
Vertical spot size at IP	σ_y^*	38.7	μm
Beam–beam linear tune shift	$\Delta\nu_x$	0.035	
Beam–beam linear tune shift	$\Delta\nu_y$	0.035	
Beam–pipe inner radius at IP	r^*	7.5	cm

Table 3.1 Operating parameters for BEPC.

High energy physics topics which can be studied in the BEPC energy range include

1. The search for glueballs and hybrids.

Parameter	Symbol	Value at J/ψ	Value at $\psi(2S)$	Units
Centre of mass energy	E	3.097	3.685	GeV
Centre of mass energy stability	$\sigma_{\langle E \rangle}$	0.09	0.10	MeV
Centre of mass energy spread	Δ_E	0.92	1.40	MeV
Peak luminosity	$\hat{\mathcal{L}}$	2×10^{30}	2.8×10^{30}	$cm^{-2}s^{-1}$
Average integrated luminosity per day	$\langle \mathcal{L} \rangle$	≈ 100	≈ 120	nb^{-1}

Table 3.2 Performance parameters for BEPC at the J/ψ and $\psi(2S)$ resonances.

2. The decay of the charmed mesons (D^0, D^+, D^-):

   (a) Leptonic and semi-leptonic branching fractions,

   (b) Cabibbo-suppressed and allowed branching fractions.

3. Charmonium spectroscopy.

4. Investigation of charmed baryon decay channels.

5. The decay of the D_s meson:

   (a) The D_s cross section,

   (b) Leptonic and semi-leptonic branching fractions.

6. Tau physics:

   (a) A precision measurement of the tau mass,

   (b) The tau one-prong problem,

   (c) The tau neutrino mass.

7. A measurement of R, where

$$R = \frac{\sigma(e^+e^- \rightarrow \text{hadrons})}{\sigma(e^+e^- \rightarrow \mu^+\mu^-)} \tag{3.1}$$

in the energy range 3 to 5 GeV.

Chapter 4 The BES Detector

Section 4.1 Overview

Construction on the Beijing Spectrometer (BES) was started in 1985 and completed in 1988. In October of the same year the first cosmic ray event was obtained and in April 1989 the detector was placed at the primary interaction point of the BEPC storage ring. It is continuing to collect data to date. Table 4.1 shows the major energy regions at which data has been taken during its operation.*

Period	Purpose	Data
Sep. 89 – Jan. 90	Debugging & Calibration	3×10^5 J/ψ's
Jan. 90 – Jun. 90	First J/ψ Run	3×10^6 J/ψ's
Nov. 90 – Jan. 91	Second J/ψ Run	3×10^6 J/ψ's
Apr. 91 – May 91	Third J/ψ Run	3×10^6 J/ψ's
Nov. 91 – Jan. 92	τ Mass Run	5.0 pb^{-1}
Jan. 92 – Jun. 92	First D_s Run	3.2 pb^{-1}
Dec. 92 – May 93	Second D_s Run	7.1 pb^{-1}
Dec. 93 – Jan. 94	$\psi(2S)$ Run	2.3 pb^{-1}
Jan. 94 – May 94	Third D_s Run	14.6 pb^{-1}

Table 4.1 Major energy region *vs.* date for BES.

The BES Collaboration is a joint U.S.–Chinese venture formed in 1991 and our first paper, a measurement of the tau mass,[68] was published in November 1992.

---

* Note that BES is inactive during the summer months each year.

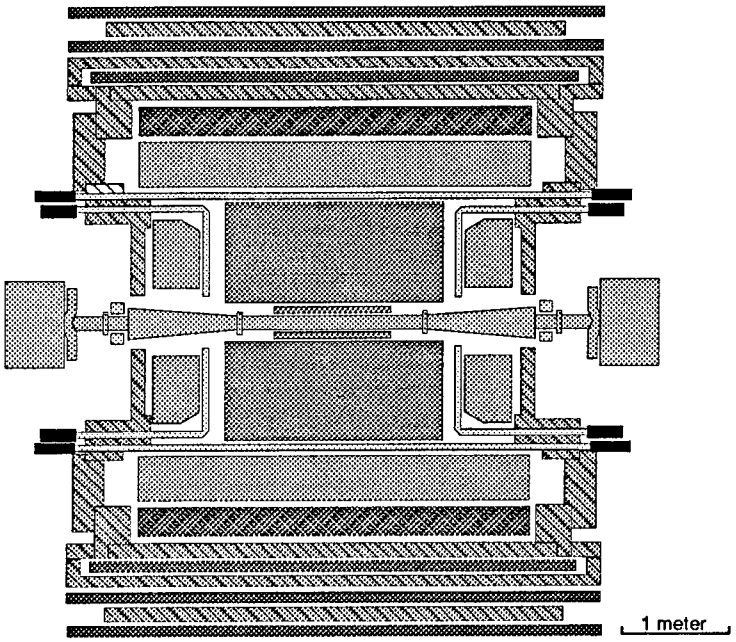

Figure 4.1 Side view of the BES detector

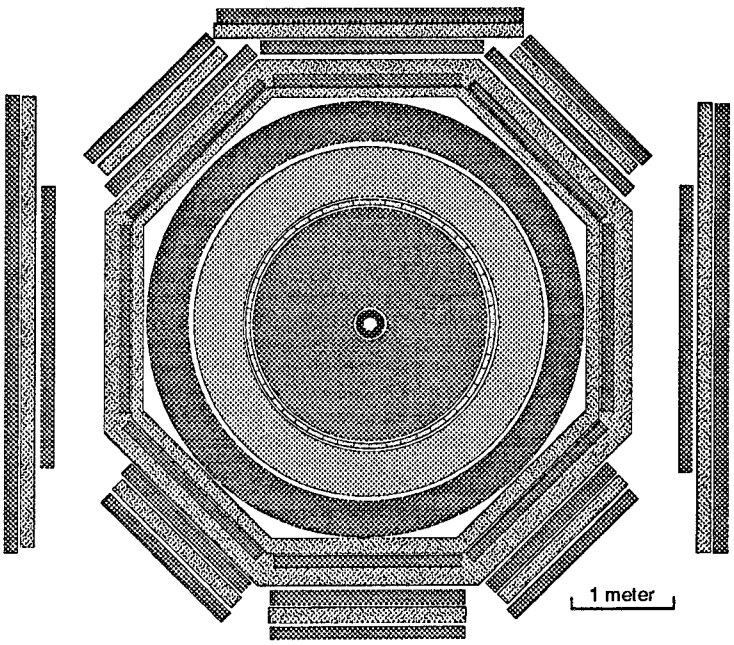

Figure 4.2 Axial view of the BES detector

BES is a general purpose magnetic spectrometer for physics in the 3 to 5 GeV region[67] based strongly on the Mark III detector.[69] Figures 4.1 and 4.2 show the side and axial views of the detector. Going outward radially, the detector consists of an evacuated beampipe in which the collision of the electrons and positrons takes place, a central drift chamber, a main drift chamber, time-of-flight scintillators, shower counters, a coil providing the magnetic field, and a flux return for the coil instrumented with muon detectors. In addition there are endcap versions of the time-of-flight detectors and the shower counters, and a luminosity monitor.

A description of these sub-systems and their nominal operating parameters is given in the following sections.

Section 4.2 The Central Drift Chamber (CDC)

A cylindrical central drift chamber of inner diameter 18.4 cm, outer diameter 30.2 cm, and length 110 cm. There are four layers of sense cells with 48 cells per layer. Each cell has one sense wire read out at both ends. This results in resolutions of $\sigma_{xy} = 150$ μm, and $\sigma_z = 1$ cm (by charge division). The solid angle coverage is 98% of 4π.

Section 4.3 The Main Drift Chamber (MDC)

The main drift chamber is another cylinder of inner diameter 31.0 cm, outer diameter 230.0 cm, and length 220.0 cm. It has ten layers of sense cells, 5 axial and 5 stereo, each cell of which has four sense wires. The number of cells per layer ranges from 48 to 108. Each sense wire provides both time and dE/dx signals, with momentum resolution $\sigma_p/p = 2.1\%\sqrt{1+p^2}$, where p is measured in units of GeV, and dE/dx resolution 8.5% at full width half maximum. The solid angle coverage is 96% of 4π at

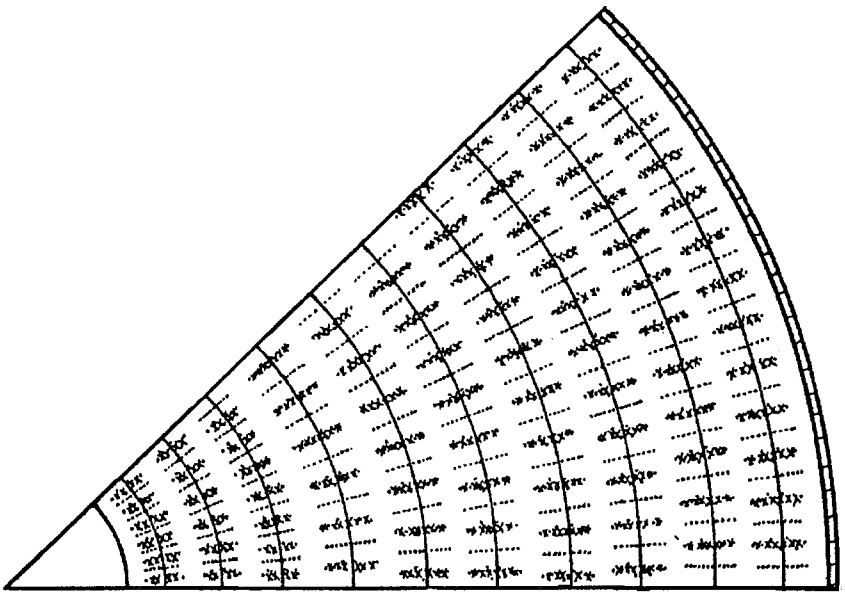

Figure 4.3 The cell structure of the main drift chamber. ×'s are sense wires, ·'s are guard wires.

the second layer. Figure 4.3 shows a cross section in the $r\phi$ plane of the cell structure of the chamber.

Section 4.4 The Time-of-Flight (TOF) System

The barrel time-of-flight counters are trapezoidal pieces of scintillator read out at both ends via photo-multiplier tubes. The main drift chamber is surrounded by 48 such pieces arranged in a cylinder. Each piece is 284 cm in length by 5 cm thick by roughly 15 cm wide. In each endcap there are 24 rectangular pieces each read out at only one end. Each is 2.5 cm thick and they form a disk of inner diameter 75 cm and outer diameter 211 cm. The time resolution provided by this apparatus is nominally 300 ps and the combined solid angle coverage is 96% of 4π. In this analysis a time resolution of between 400 and 450 ps was measured for the barrel; the endcap was used only to detect extraneous charged and neutral tracks.

Section 4.5 The Electromagnetic Calorimeter

The electromagnetic calorimeter consists of shower counters on both the barrel (inner diameter 247.0 cm, outer diameter 338.2 cm, length 385.0 cm) and endcaps (inner diameter 74.6 cm, outer diameter 192.0 cm, thickness 41.0 cm). The counters are 12 radiation lengths thick separated into 24 layers: each a lead plate followed by a gas-counter forming a sandwich-like structure.

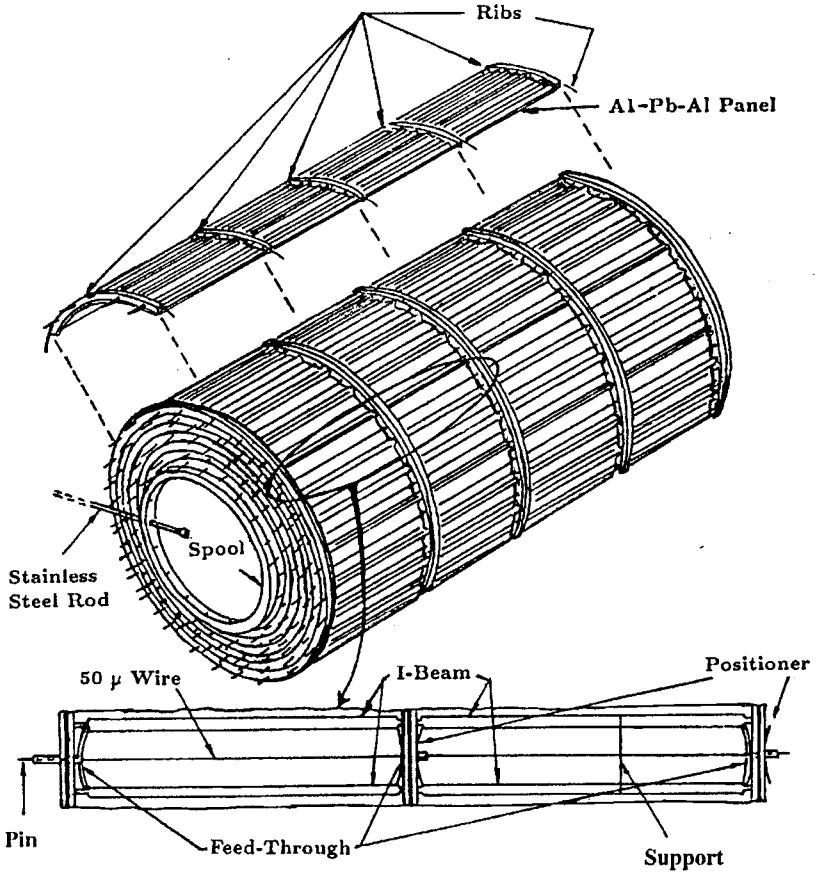

Figure 4.4 A schematic diagram of the barrel shower counter.

The gas used is a 33% Argon–67% CO_2 mixture bubbled through 0°C n-pentane and the counters run in self-quenching streamer mode. Energy and position reso-

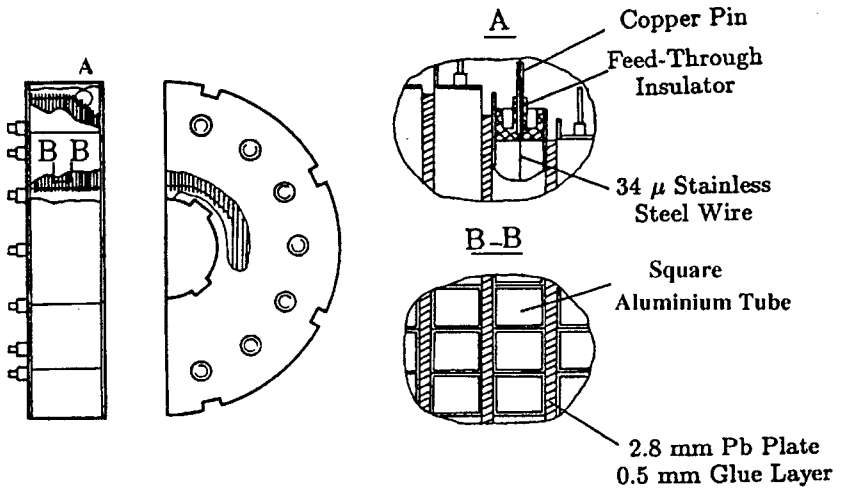

Figure 4.5 A schematic diagram of the endcap shower counter.

lutions are $\sigma_E/E = 25\%/\sqrt{E(\text{GeV})}$, $\sigma_\phi = 4.5$ mrad, $\sigma_z = 2$ cm in the barrel, and $\sigma_x = 0.7$ cm, $\sigma_y = 13\%L$ (where L is the tube length) in the endcaps. The combined solid angle coverage is 94% of 4π. Figures 4.4 and 4.5 show schematic diagrams of the barrel and endcap shower counters. During our data taking the endcap shower counter was not fully calibrated. In this experiment it was used only as a veto on extraneous charged and neutral tracks.

Section 4.6 The Muon System

The muon tracking system resides outside the rest of the detector and consists of three double layers of proportional counter tubes sandwiched with iron absorber (which also acts as a flux return for the magnet) arranged in an octagonal structure. Each wire is read out at both ends to provide z measurement via charge division. The position resolution is $\sigma_z = 5$ cm, $\sigma_{r\phi} = 3$ cm; solid angle coverage is 68% of 4π.

Section 4.7 Additional Apparatus

The Luminosity Monitor

The luminosity monitor[70] consists of four combined scintillator and shower counter telescopes in two opposing pairs placed symmetrically about the interaction point (IP) as shown in Figure 4.6. Their purpose is to measure the number of low angle Bhabha events. Given precision measurements of the positions of the four telescopes one can combine this data with the machine collision parameters from Table 3.1 and calculate the luminosity.

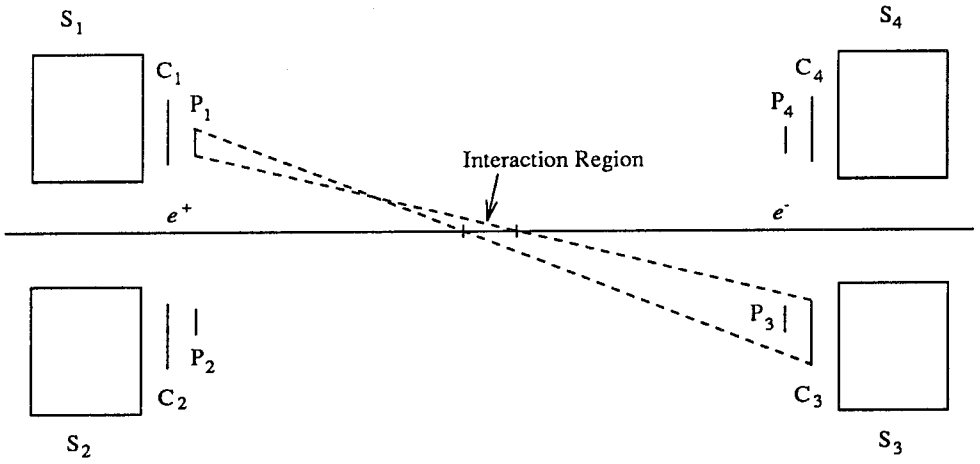

Figure 4.6 A schematic diagram of the luminosity monitor.

As can be seen from the figure, each telescope consists of three parts—the P, C, and S counters. Both P and C counters are pieces of scintillator read out via light pipes and photo-multiplier tubes. They provide a yes/no answer to "Was I hit?" The S counters are sandwiched layers of lead and plastic scintillator. The light from the scintillator is guided out via light pipes to a photo-multiplier tube. This yields an estimate of the energy deposited with resolution $\approx 13\%$ at our energy.

The P counters define the angular acceptance of the monitor. The C counters are arranged so that each one covers the angle subtended by the opposite P counter no matter where in the interaction region the collision takes place. Coincidence timing between opposing counters and an energy estimate from the S counters are used to distinguish Bhabha events from beam gas or cosmic backgrounds.

If P_i implies a hit in the P scintillator of counter i, C_i in the C counter, and S_i implies that the energy in the S part of counter i is above a pre-set threshold (beam energy-3.5σ, where σ is the energy resolution) then a readout of the luminosity data is triggered whenever any one of the following three conditions is true:

1. A coincidence of $(P_1 \cdot S_1) \cdot (C_3 \cdot S_3)$, $(P_2 \cdot S_2) \cdot (C_4 \cdot S_4)$, $(P_3 \cdot S_3) \cdot (C_1 \cdot S_1)$, or $(P_4 \cdot S_4) \cdot (C_2 \cdot S_2)$ within a 50 ns gate of the beam crossing.

2. A coincidence of $(P_1 \cdot S_1) \cdot (C_3 \cdot S_3)_{\mathrm{del}}$, $(P_2 \cdot S_2) \cdot (C_4 \cdot S_4)_{\mathrm{del}}$, $(P_3 \cdot S_3) \cdot (C_1 \cdot S_1)_{\mathrm{del}}$, or $(P_4 \cdot S_4) \cdot (C_2 \cdot S_2)_{\mathrm{del}}$ where "del" implies a coincidence from the previous beam crossing.

3. Every 10^6 beam crossings regardless of any other trigger.

Trigger 1 measures the number of true plus fake Bhabha events. Trigger 2 provides an estimate of the number of fake Bhabha events *i.e.*, those accidental coincidences which do not derive from real Bhabha events but from two opposing counters experiencing independent triggers at the same time. This rate is subtracted from that measured by Trigger 1 to leave a number proportional to the luminosity. Trigger 3 helps to measure the random background in order to study any correlations among the counters.

The Beam Pipe

The beam pipe is an aluminium cylinder of inner diameter 15.0 cm and outer diameter 15.4 cm. This is equivalent to 0.0225 radiation lengths. During running periods the beam pipe in the region of the IP is evacuated to a pressure of 5×10^{-10} torr.

The Magnetic Field

A magnetic field of 0.4 Tesla is provided by an aluminium coil of inner diameter 3.48 m, outer diameter 4.14 m, and length 3.60 m. The inhomogeneity of the field within the tracking volume is less than 3%.

The Trigger

The trigger for the detector (as opposed to for the luminosity monitor) takes information from all the sub-detectors and combines them to see whether the event is worth writing to tape. For the duration of the tau run data a logical OR of the charged and endcap shower counter (ESC) triggers was used.

The charged trigger implies that at least one charged track is detected by the main drift chamber, that there are hits in layers 3 or 4 of the CDC, that at least one TOF counter is hit, and there is at least 200 MeV of energy in the barrel shower counter. The ESC trigger detects events which have hits in the CDC, pass an energy threshold in the endcap shower counters, and have at least one hit in each of the east and west endcap TOF counters.

Part III
Theoretical Details

"There is a theory which states that if ever anyone discovers exactly what the Universe is for and why it is here, it will instantly disappear and be replaced by something even more bizarre and inexplicable.

There is another which states that this has already happened."

Douglas Adams
The Restaurant at the End of the Universe

Chapter 5 The Search Method

Section 5.1 Outline of the Tau Mass Estimation

The method for measuring the mass of the tau lepton presented in this thesis is to measure the tau pair production threshold energy via a likelihood-driven search. This threshold is the lowest energy at which tau production is possible* and is directly related to the tau mass via $E_{\text{threshold}} = 2m_\tau$. Because of this, this measurement is independent of the mass of the tau neutrino m_{ν_τ}.

In order to measure this energy we will take data at various energies E_i. At each energy we record (i) the integrated luminosity $\mathcal{L}_i$ accumulated at that energy, and (ii) the number of $\tau^+\tau^-$ events detected during that running period n_i. At the end of the search all of this data is fitted to a parameterized form for the cross section via a likelihood function. The value of the tau mass parameter at the peak of the likelihood corresponds to the best estimate for m_τ.

We used a likelihood method during the search to estimate the most efficient energy at which to run next, *i.e.*, E_{i+1} depends on the set of data accumulated thus far, $\{\{E_1, \mathcal{L}_1, n_1\}, \ldots, \{E_i, \mathcal{L}_i, n_i\}\}$. A synopsis of the method describing how each energy is chosen is given below; the full algorithm is described in Section 5.4.

After each search point a likelihood is generated that at each point so far the number of tau events observed n_i fits the number of events expected μ_i at that energy

---

* Note that taus can *appear* to have non-zero cross section at centre of mass energies below threshold. However, this is an illusion caused by smearing of the centre of mass energy. See page 34 for details.

as a function of m_τ. This likelihood is used to identify the energy most sensitive to the tau mass where the tau mass is estimated from the peak of the likelihood.

To find μ_i a parameterized form for the cross section is assumed. As explained in Section 5.2, this implies that the likelihood is a function of the following parameters: the mass of the tau lepton m_τ^*, the product of detection efficiency and relevant branching fractions for the mode in question κ^*, and the effective background cross section for that mode σ_B^*.†

The form of the cross section is such that one would like to choose the set of search energies so that we have some energies below threshold and some above. This gives a more accurate estimate of the tau mass but it does mean that at some of our search points we will expect to observe only background events, if any.

During the search σ_B^* is kept fixed at a level determined from studying background at the J/ψ resonance (see Section 7.2); κ^* is kept fixed at our best estimate from Monte Carlo studies (see Section 7.3). The best estimate for m_τ at any given time is the peak of the likelihood,[71] now a function of m_τ^* only, using all information available up to that point. The next search energy is then derived from the likelihood by calculating the energy most sensitive to the tau mass (see Section 5.4 for details). It is also useful to have some data taken well above threshold, *i.e.*, not as part of the search. This helps to reduce the uncertainty in κ^*.

After the conclusion of the search κ^* and σ_B^* are allowed to vary along with m_τ^* in a three-dimensional likelihood fit to better estimate the systematic errors due to those quantities. In theory it would be possible to swap to a multi-dimensional likelihood before the end of the search, but care must be taken to avoid trying to

† From now on parameters will be distinguished from reported values via the $*$ notation.

fit too many parameters with too little data. In our experiment we did not utilize a multi-dimensional likelihood until after the search was completed.

Having evaluated this final likelihood, the reported value for each of these parameters, in particular the tau mass, is then just the value of that parameter at the peak of the likelihood function. Chapter 8 will show how the uncertainties on these values are calculated.

Section 5.2 The Likelihood Function

Given N search points each of which has a number of $\tau^+\tau^-$ events detected n, a centre of mass energy E, and an integrated luminosity $\mathcal{L}$, one may generate a likelihood L as a product of probabilities as follows:

$$L(m_\tau^*, \kappa^*, \sigma_B^*) = \prod_{i=1}^{N} P(n_i\,;\mu_i), \tag{5.1}$$

where $P(n_i\,;\mu_i)$ is a Poisson probability,

$$P(n_i\,;\mu_i) = \frac{e^{-\mu_i}{\mu_i}^{n_i}}{n_i\,!}, \tag{5.2}$$

and the mean μ_i is given by

$$\mu_i(E_i, \mathcal{L}_i\,; m_\tau^*, \kappa^*, \sigma_B^*) = [\kappa^*\sigma(E_i, m_\tau^*) + \sigma_B^*]\mathcal{L}_i. \tag{5.3}$$

κ^* is the branching fraction efficiency product. For instance, for the single mode $\tau^+\tau^- \rightarrow e\mu$ one can write $\kappa^* = 2B_eB_\mu\epsilon^*$ where B_e and B_μ are the branching fractions of the electronic and muonic decay modes of the tau respectively and ϵ^* is the estimated detection efficiency for that mode including all acceptance effects. σ_B^* is the effective background cross section and σ is the pair production cross section.

Section 5.3 Pair Production Cross Section

The lowest order Feynman diagram for tau pair production is shown in Figure 5.1.

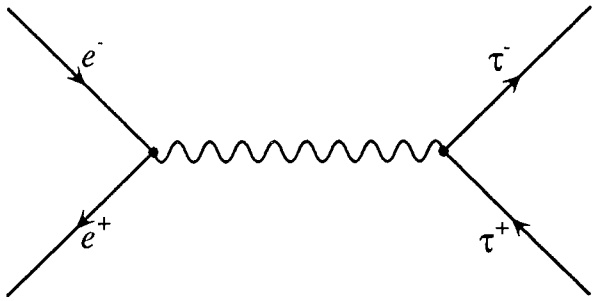

Figure 5.1 Lowest order Feynman diagram for $e^+e^- \rightarrow \tau^+\tau^-$.

This leads to a production cross section σ_0 of

$$\sigma_0 = \frac{4\pi\alpha^2}{3E^2}\frac{\beta(3-\beta^2)}{2} \tag{5.4}$$

where E is the total energy in the centre of mass frame and $\beta = \sqrt{1-\frac{4m_\tau^2}{E^2}}$.

Including Coulomb interactions and final state radiation[72] yields

$$\sigma_1(E, m_\tau) = \sigma_0(E, m_\tau)F_c(\beta)F_r(\beta) \tag{5.5}$$

where

$$F_c(\beta) = \frac{\pi\alpha/\beta}{1-\exp(-\pi\alpha/\beta)} \tag{5.6}$$

and

$$\begin{aligned} F_r(\beta) = 1 + \left(\frac{\alpha}{\pi\beta}\right)\Bigg\{ & (1+\beta^2)\left[\ln\frac{1+\beta}{2}\ln\frac{1+\beta}{1-\beta} + 2l\left(\frac{1-\beta}{1+\beta}\right)\right. \\ & \left. - \frac{\pi^2}{3} + 2l\left(\frac{1+\beta}{2}\right) - 2l\left(\frac{1-\beta}{2}\right) - 4l(\beta) + l(\beta^2)\right] \\ & + \left[\frac{11}{8}(1+\beta^2) - 3\beta + \frac{1}{2}\frac{\beta^4}{3-\beta^2}\right]\ln\left(\frac{1+\beta}{1-\beta}\right) \\ & + 6\beta\ln\left(\frac{1+\beta}{2}\right) - 4\beta\ln\beta + \frac{3}{4}\beta\frac{(5-3\beta^2)}{(3-\beta^2)}\Bigg\} \end{aligned} \tag{5.7}$$

where

$$l(x) = -\int_0^x \frac{\ln(1-t)}{t} dt = \sum_{n=1}^{\infty} x^n/n^2. \tag{5.8}$$

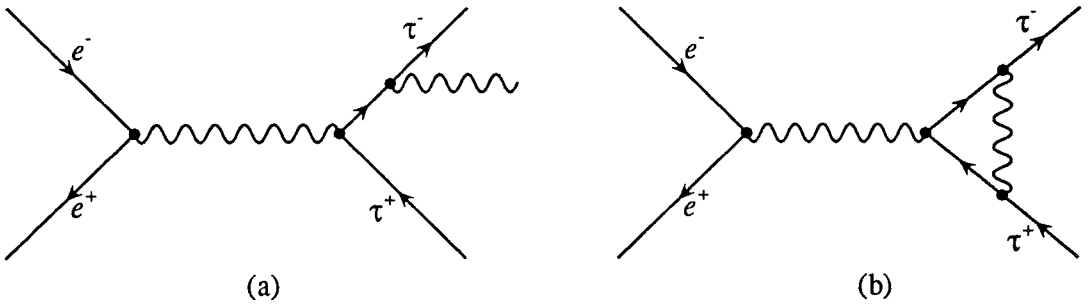

Figure 5.2 Lowest order Feynman diagrams for (a) final state radiation and (b) Coulomb interactions.

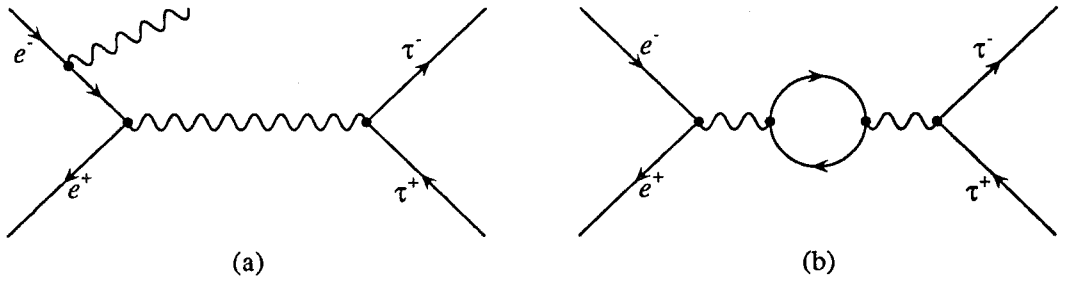

Figure 5.3 Lowest order Feynman diagrams for (a) initial state radiation and (b) vacuum polarization.

Further including initial state radiation and vacuum polarization effects yields

$$\sigma_2(E, m_\tau) = \int_0^{1-(4m_\tau^2/s)} \frac{F(x,s)\ \sigma_1\left(\sqrt{(1-x)s}, m_\tau\right)}{\left\{1 - \Pi[(1-x)s]\right\}^2} dx \tag{5.9}$$

where $s = E^2$ and forms for $F(x,s)$ and $\Pi(s)$ can be found in References 73 and 74.

Finally electrons and positrons in the storage ring bunches are modelled as having a Gaussian distribution in energy.* This is taken into account by a convolution of the previous form for the cross section σ_2 with a Gaussian of width Δ_E (Δ_E is known as the energy spread and can be measured for any given storage ring configuration). This yields a final form for the cross section of:

$$\sigma(E, m_\tau) = \frac{1}{\sqrt{2\pi}\Delta_E} \int_{-\infty}^{\infty} dE' \exp\left[-\frac{(E-E')^2}{2\Delta_E^2}\right] \sigma_2(E', m_\tau). \qquad (5.10)$$

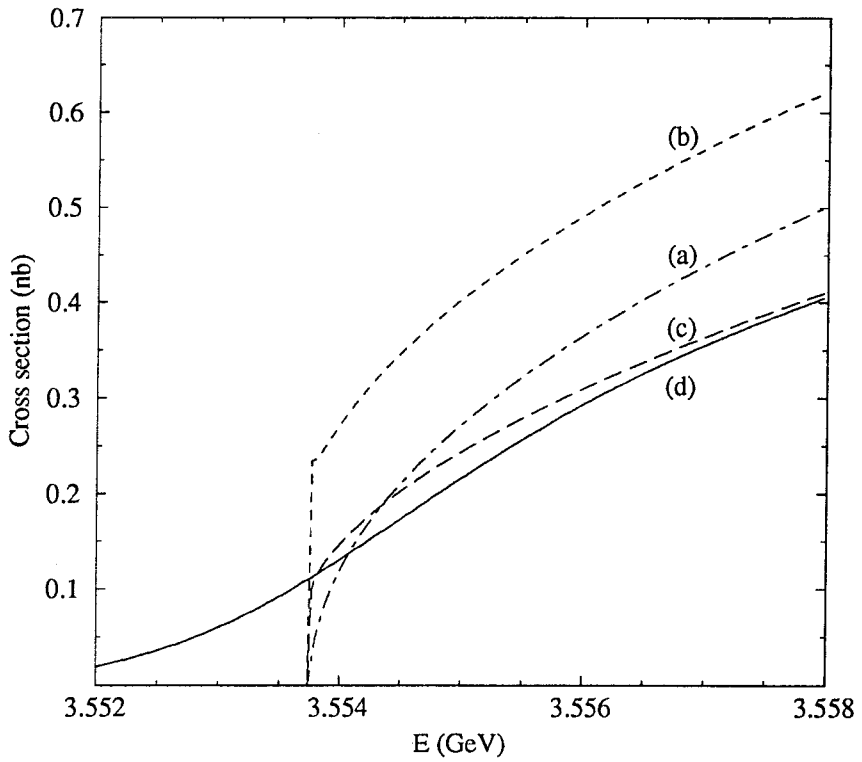

Figure 5.4 A comparison of the cross section (a) uncorrected, (b) after final state radiation and Coulomb interaction corrections, (c) after initial state radiation and vacuum polarization corrections, and (d) after beam smearing.

* Actually there are small non-Gaussian tails to the distribution which will be ignored.

Note two things:

1. In principle Δ_E is a function of energy. In practice this effect is negligible. Systematic uncertainties in Δ_E are considered in Section 8.4.

2. If the two particles that happen to collide have a centre of mass energy above threshold for tau production even though the average centre of mass energy is below, taus may be produced. However, the energy reported for the collision is the average centre of mass energy. Hence it may *appear* that taus are being produced below threshold.

A comparison of the cross section showing the cumulative effect of these corrections is shown in Figure 5.4 for $m_\tau = 1776.9$ MeV and $\Delta_E = 1.4$ MeV. As mentioned above it is the final, beam smearing convolution that causes the cross section to have non-zero values below tau threshold.

Section 5.4 Details of the Search Procedure

The object of the likelihood search procedure is to take as much data as possible as close as possible to the energy most sensitive to the tau mass, *i.e.*, the energy for which the uncertainty in m_τ is minimized assuming a fixed integrated luminosity, detection efficiency and background. δm_τ, the uncertainty in m_τ, is related to that of the threshold energy δE_{thresh} by $\delta m_\tau = 1/2\ \delta E_{\text{thresh}}$. This latter quantity can be estimated as follows:

$$\delta E_{\text{thresh}} = \delta\mu \frac{\partial E}{\partial \mu} = \delta\mu \Big/ \frac{\partial \mu}{\partial E} \tag{5.11}$$

where μ is the expected number of events. The variance of a Poisson distribution is equal to its mean. Hence an estimate for $\delta\mu$ is $\sqrt{\mu}$. Since the expected background is small we can also approximate $\mu \propto \sigma$. Hence $\delta\mu \propto \sqrt{\sigma}$.

At fixed $\mathcal{L}$, κ^*, and σ_B^* we find, using Equation (5.3), that

$$\frac{\partial \mu}{\partial E} \propto \frac{\partial \sigma}{\partial E}. \tag{5.12}$$

Hence if I define

$$\text{Sensitivity} = \frac{1}{(\delta m_\tau)^2} \tag{5.13}$$

then

$$\text{Sensitivity} \propto \frac{1}{\sigma}\left(\frac{\partial \sigma}{\partial E}\right)^2. \tag{5.14}$$

The quantity on the right hand side of Equation (5.14) is plotted in Figure 5.5. This shows that the maximum sensitivity occurs at $E = 2m_\tau - \delta$ where the offset δ is approximately 0.3 MeV in this case. This value is only valid for $m_\tau = 1784.1$ MeV and $\Delta_E = 1.4$ MeV, but varies by only ± 0.05 MeV for $1.772 < m_\tau < 1.7841$ and $1.3 < \Delta_E < 1.5$.* The exact value of the offset is almost irrelevant because the precision with which the centre of mass energy of the storage ring can be tuned, the stepsize s, is only 0.3 MeV. For this experiment a value of 0.3 MeV was used for δ independent of m_τ and Δ_E.

The estimate for the tau mass changes as the search progresses. Hence the estimate for the most sensitive search energy changes also. An algorithm for selecting a new search energy is presented on page 37.

However at the beginning of the search this algorithm is not fully defined. Firstly, no energy for the first point E_1 has been selected. Also, if no events are observed at the first search point then the likelihood is "open-ended" in the sense that $L(m_\tau^*) \to 1$

$\star$ The limits chosen for m_τ and Δ_E are approximately the minima and maxima during our search, see page 116.

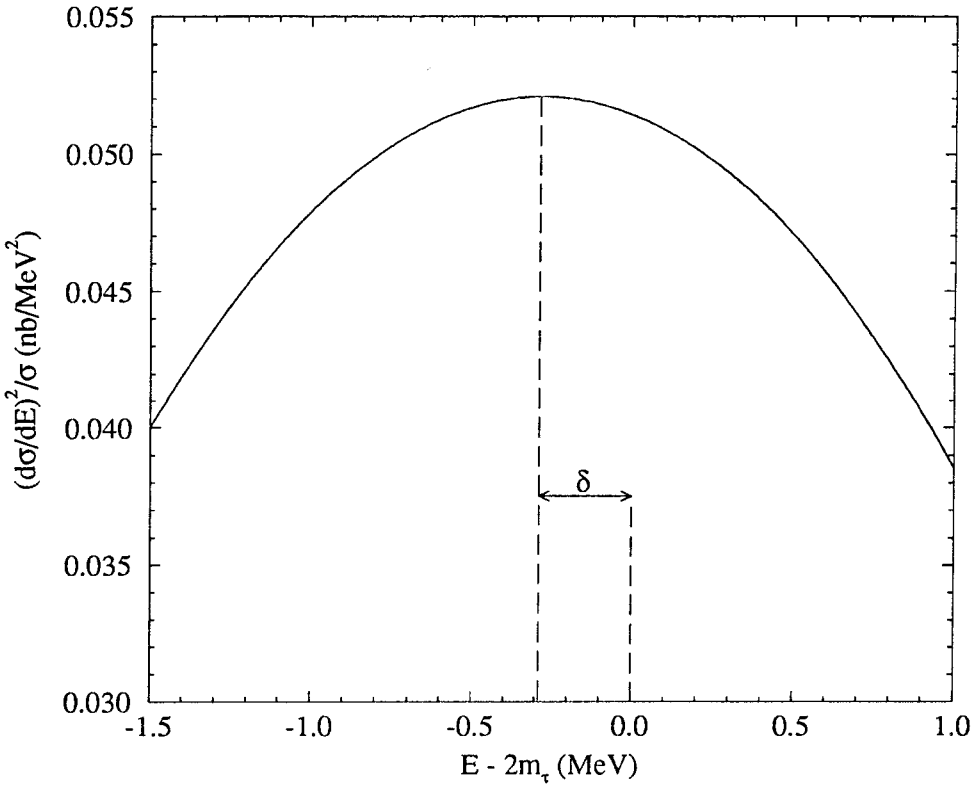

Figure 5.5 $1/\sigma(\partial\sigma/\partial E)^2$ *vs.* $(E - 2m_\tau)$ for m_τ = 1784.1 MeV, Δ_E = 1.4 MeV.

as $m_\tau^* \to \infty$ (see Figure 5.6). In this case there is no well defined peak from which to calculate the next search energy.

In fact this is just an extreme case of the observation that the accuracy† of the algorithm described above is very sensitive to the number of events found at the first search point: if you find zero events the likelihood is "open-ended"; if you find a large number of events the peak of the likelihood thus generated can be as far as 119 MeV from the initial value (see Figure 5.7 and page 71).

The first problem is easily solved: the first search point is chosen at $E_1 = 2m_\tau^0$

† Accuracy is defined as $m_\tau^{\text{final}} - m_\tau^{\text{true}}$ (see Section 6.1).

Algorithm 1.

1. At convenient intervals (approximately every 250 nb^{-1}) we re-calculate a new candidate search energy $E_{\text{cand}} = 2m_\tau^{\text{peak}} - \delta$, where m_τ^{peak} is the value of m_τ at the peak of the most recent likelihood.
2. If $|E_{\text{cand}} - E_i| \geq s$, we set $E_{i+1} = E_{\text{cand}}$ and accumulate data at the new search point.
3. Otherwise the energy is not changed and we continue to accumulate data at E_i.

---

where m_τ^0 is the best estimate for the tau mass at the time when the search is started. In our case $m_\tau^0 = 1784.1$ MeV.

The second problem requires that a different algorithm be applied to the likelihood function until the likelihood is well defined in some sense. The algorithm we chose to apply was to restrict the energy domain in which the search takes place, but to allow this energy domain to expand with increasing integrated luminosity (see page 39).

This procedure restricts the size of the initial step $E_2 - E_1$ and hence the extremely large step in energy shown in Figure 5.7 is avoided. It also allows for the possibility that zero events have been observed so far and thereby avoids the problems associated with the "open-ended" likelihood of Figure 5.6.

The algorithm is followed until it is considered that enough data has been taken. In our case a time limit was imposed and we accumulated as much data as possible during that period. This procedure is shown in Chapter 6 to be robust, reliable and

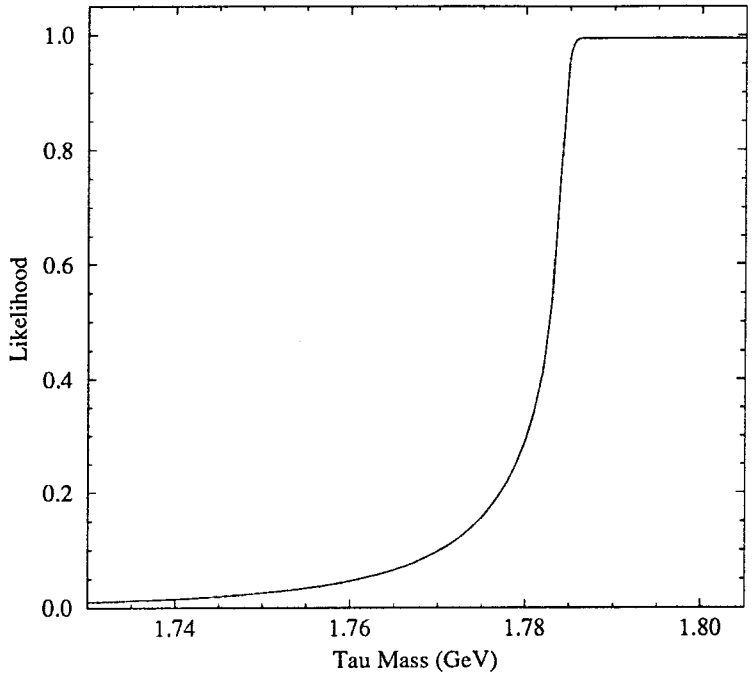

Figure 5.6 An example of an "open-ended" likelihood.

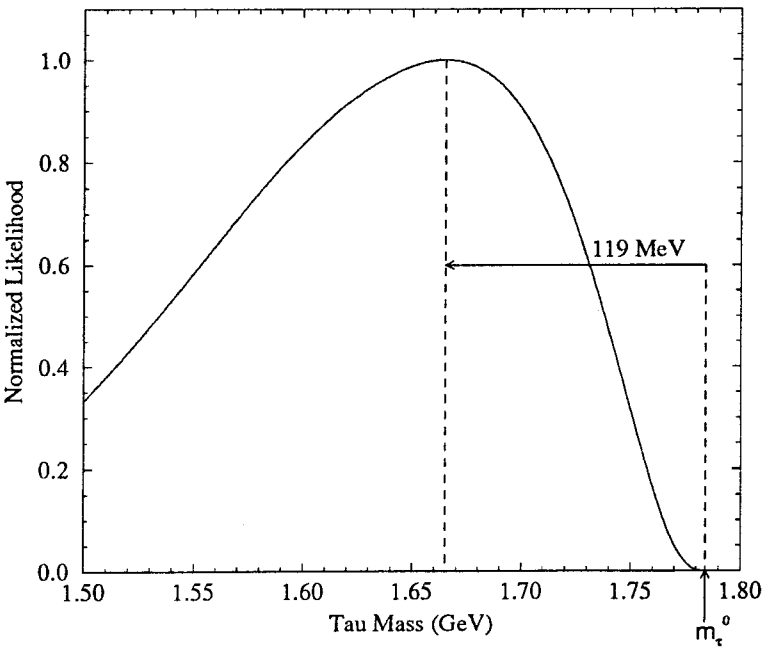

Figure 5.7 The likelihood after seven events are detected at the first search point.

Algorithm 2.

1. Each 250 nb^{-1} re-calculate the likelihood $L(m_\tau^*)$.
2. Construct a new function of $g(m_\tau^*)$ by multiplying the likelihood by a Gaussian whose width σ expands with integrated luminosity and whose centre μ_{exp} is normally equal to m_τ^0, *i.e.*,

$$g(m_\tau^*) = L(m_\tau^*)\exp\Big(-(m_\tau^* - \mu_{\mathrm{exp}})^2 / 2\sigma^2\Big) \tag{5.15}$$

   where $\sigma = \alpha\mathcal{L}$ and $\mathcal{L}$ is the total accumulated integrated luminosity so far.
3. Find the peak of $g(m_\tau)$, $m_\tau^{\mathrm{peak}}(g)$, and define a candidate new energy E_{cand} via

$$E_{\mathrm{cand}} = 2m_\tau^{\mathrm{peak}}(g) - \delta. \tag{5.16}$$

4. If $|E_{\mathrm{cand}} - E_i| \geq s$ then $E_{i+1} = E_{\mathrm{cand}}$.
5. Otherwise $E_{i+1} = E_i$.

efficient. A flow diagram for the search procedure can be found in Figure 5.8.

Several scans of the J/ψ and $\psi(2S)$ resonances were also taken before, during* and after the search (see Figure 8.4). The peak energies of the two resonances are known very accurately and measuring them at frequent intervals is a way of calibrating the scale on which we measure the search point energies. Further details of this procedure can be found in Section 8.4.

$\star$ Between search points.

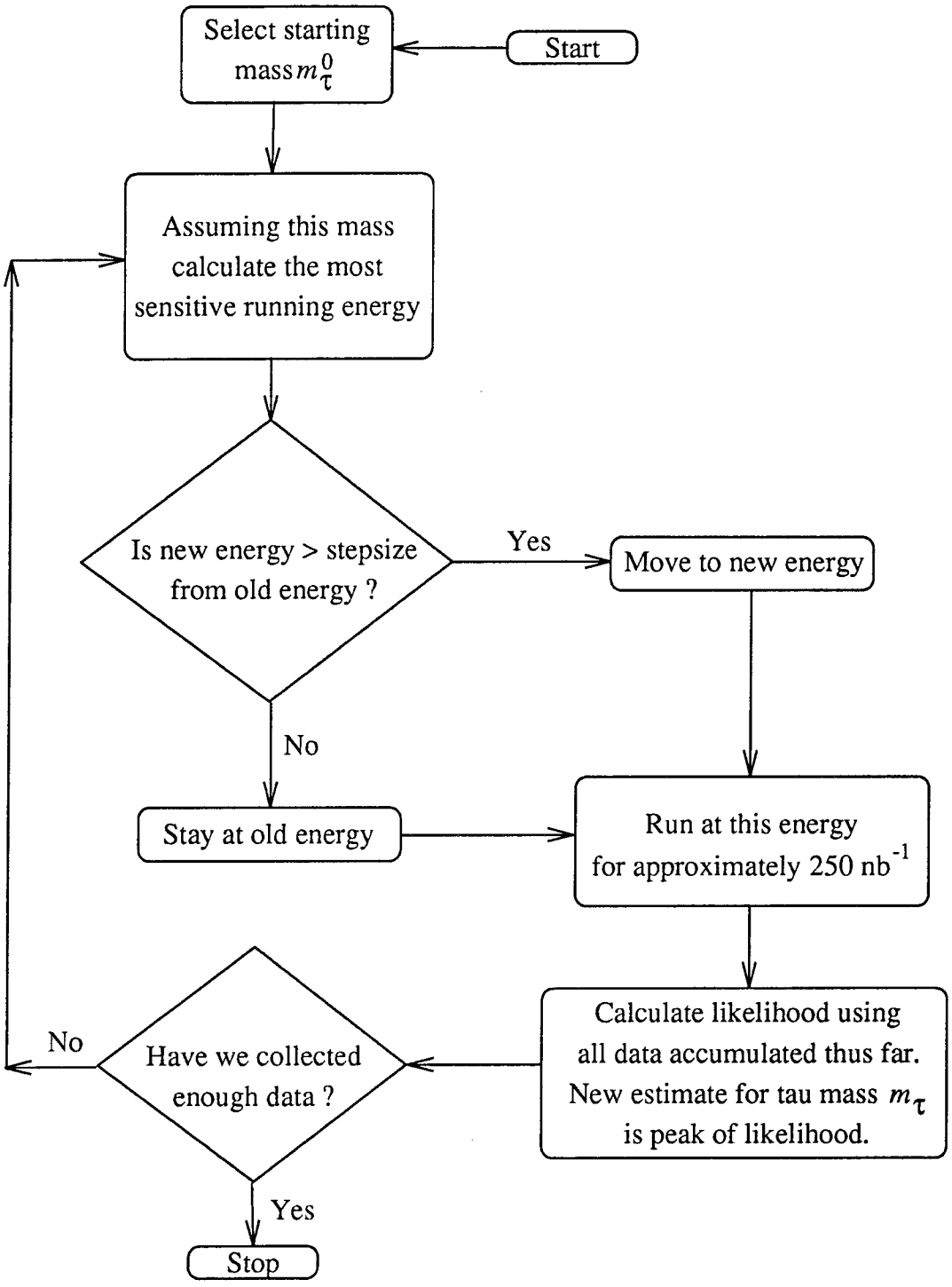

Figure 5.8 A flow diagram for the search procedure.

Chapter 6 Likelihood Studies

Section 6.1 Introduction

For a likelihood function L based on a variable x with a Gaussian distribution of non-zero variance σ^2 and with a value of x at maximum L of $x^{\max}$, one finds that $\ln L$ is a parabola: $\ln L = c - (x - x^{\max})^2/2\sigma^2$ where $c = \max(\ln L)$ is a constant. If one defines the points x^- and x^+ via

$$\begin{aligned} x^- &= x, \text{ where } \ln L = c - 1/2 \text{ and } x < x^{\max} \\ x^+ &= x, \text{ where } \ln L = c - 1/2 \text{ and } x > x^{\max} \end{aligned} \tag{6.1}$$

then it follows that

$$\sigma = x^{\max} - x^- = x^+ - x^{\max} \ . \tag{6.2}$$

For a non-Gaussian variable y a common approach to estimating a measure of the width of the likelihood is to define

$$\sigma^- = y^{\max} - y^- \tag{6.3}$$

$$\sigma^+ = y^+ - y^{\max} \tag{6.4}$$

where $y^{\max}$, y^- and y^+ are defined via the same method as $x^{\max}$, x^- and x^+ above. In the limit that the variable y becomes Gaussian one would expect $\sigma^- = \sigma^+ = \sigma$.

The method used in this thesis, however, is to define such negative and positive widths based on the integrated area under the likelihood function rather than the

value of that function, *i.e.*, define σ_A^+ and σ_A^- via

$$\int_{y^{\max}}^{y^{\max}+\sigma_A^+} L(y)\,dy = 0.6826 \int_{y^{\max}}^{+\infty} L(y)\,dy \tag{6.5}$$

and

$$\int_{y^{\max}-\sigma_A^-}^{y^{\max}} L(y)\,dy = 0.6826 \int_{-\infty}^{y^{\max}} L(y)\,dy \tag{6.6}$$

where 0.6826 is the fraction of area between the peak + σ and the peak − σ for a Gaussian variable. This method is more suitable for my purposes as it yields estimates for uncertainties for which 68.26% of experiments* have the true mass within the range $y^{\max} - \sigma_A^-$ to $y^{\max} + \sigma_A^+$.

However, these are not the only ways of characterizing the likelihood. If L can be normalized such that $\int_{-\infty}^{+\infty} L(y)\,dy = 1$ then some other ways are:

1. To calculate the mean $\bar{y}$ and the standard deviation σ of the likelihood just as for any other one-dimensional distribution,

$$\bar{y} = \int_{-\infty}^{+\infty} yL(y)\,dy, \tag{6.7}$$

$$\sigma^2 = \int_{-\infty}^{+\infty} y^2 L(y)\,dy - \bar{y}^2. \tag{6.8}$$

2. To calculate the median y^{med} of the distribution via

$$\int_{-\infty}^{y^{\text{med}}} L(y)\,dy = 0.5. \tag{6.9}$$

3. Widths can be calculated around the median instead of the peak: one may

* Within statistical uncertainties when modelled by Monte Carlo.

define σ_B^+ and σ_B^- where

$$\int_{y^{\rm med}}^{y^{\rm med}+\sigma_B^+} L(y)\,dy = \int_{y^{\rm med}-\sigma_B^-}^{y^{\rm med}} L(y)\,dy = 0.3413. \tag{6.10}$$

For a Gaussian variable, the peak, mean, and median are identical. Similarly all measures of the width, both postive and negative are equal. For a non-Gaussianly distributed variable any or all of these equalities can be broken.

In addition to the above quantities, but for Monte Carlo data only, I can also calculate the accuracy Δ at any point in the search as:

$$\Delta = m_\tau^{\rm peak} - m_\tau^{\rm true} \tag{6.11}$$

where $m_\tau^{\rm true}$ is the true mass of the tau lepton as input to the Monte Carlo program. $m_\tau^{\rm peak}$ is the estimated value that the program reports as the tau mass at any particular time, *i.e.*, the value of m_τ^* at the peak of the likelihood function. Obviously the value of the accuracy at the end of the search $\Delta^{\rm final}$ is of particular interest, however I shall also be concerned with its value during the search.

The average of $\Delta^{\rm final}$ over a large number of statistically independent experiments is the bias b:

$$b = \left\langle m_\tau^{\rm final} \right\rangle - m_\tau^{\rm true}\ . \tag{6.12}$$

The bias is a function of the true mass and of the search algorithm that the program models. I will present studies of the dependence of the bias on various properties of the algorithm in Section 6.5.

Section 6.2 Typical Likelihoods

For the purposes of discussing a particular typical search, 1000 searches with $m_\tau^0 =$ 1784.1 MeV, $m_\tau^{\text{true}} =$ 1776.9 MeV, $\mu_{\text{exp}} = m_\tau^0$, and $\alpha = 0.04$ MeV/nb^{-1} † were modelled via a Monte Carlo program `mctau` (see Appendix A) and one of those that showed typical attributes (the great majority) chosen at random. Sections 6.4 and 6.5 will discuss average values for many such searches and show that this search is indeed "typical."

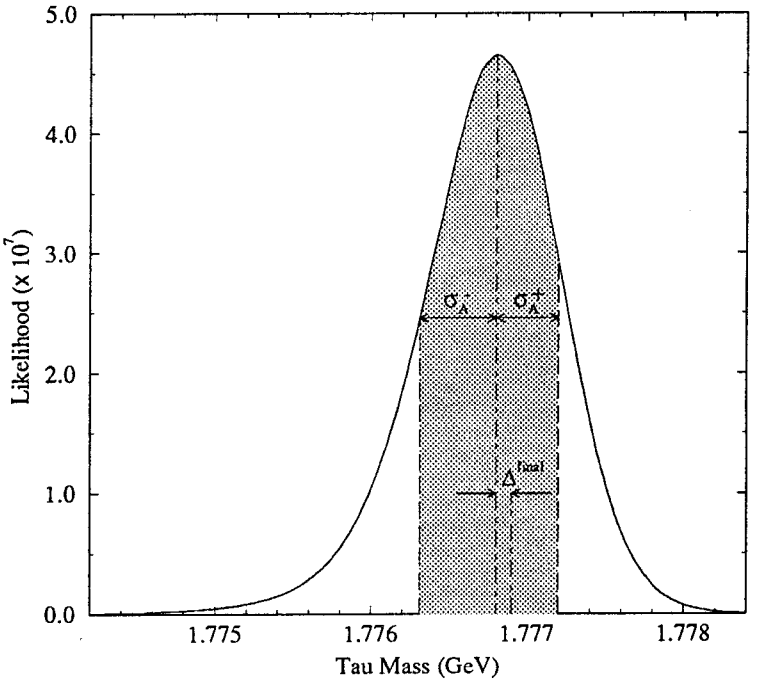

Figure 6.1 A typical final likelihood function showing σ_A^-, σ_A^+, and Δ^{final}.

Table 6.1 shows the values for the centre of mass energies E, the integrated luminosities $\mathcal{L}$, and the number of $\tau^+\tau^-$ events found n at each search point (in

† Note: these parameters were chosen since they represent most closely the search which actually took place.

Search Point	E (GeV)	$\mathcal{L}$ (nb^{-1})	n
1	3.56820	250.0	2
2	3.55770	250.0	0
3	3.55940	250.0	1
4	3.55740	250.0	2
5	3.55190	250.0	0
6	3.55340	250.0	0
7	3.55430	250.0	0
8	3.55480	250.0	2
9	3.55280	250.0	0
10	3.55310	250.0	1
11	3.55230	250.0	0
12	3.55230	250.0	0
13	3.55270	250.0	0
14	3.55270	250.0	0
15	3.55300	250.0	0
16	3.55300	250.0	0
17	3.55300	250.0	0
18	3.59902	499.7	5
19	3.57910	250.0	1

Table 6.1 Data from a typical Monte Carlo search.

this case the Monte Carlo modelled $e\mu$ decays, but that is not necessary). Δ_E was approximated as constant at 1.4 MeV. Figure 6.1 shows the final likelihood function derived using all of this data. The quantities σ_A^+, σ_A^-, and Δ^{final} are indicated.

Some properties of the likelihood to note are: (*i*) the scale of the plot—it is only a few MeV wide, (*ii*) the fact that σ_A^+ and σ_A^- are almost equal, and (*iii*) that the likelihood has only a single peak. These properties will be discussed in detail in Section 6.6 where I will consider some of the problems that can prevent the search from finding the correct mass.

To explain the shape of the likelihood consider how it is formed. At each search point we detect a non-negative number of events which pass the selection criteria. Figure 6.2 shows a comparison between the likelihood functions due to finding zero, one, and two events at search point 1, *i.e.*, $P(0\,;\mu_1)$, $P(1\,;\mu_1)$, and $P(2\,;\mu_1)$. The beam energy (indicated by the vertical dashed line) was 1784.1 MeV, the integrated luminosity was 250 nb^{-1}. κ^* and σ_B^* were kept fixed at 0.008889 and 0.024 pb respectively.

For the zero-event likelihood one may see that L approaches approximately one as m_τ^* becomes large, whereas for non-zero-event likelihoods L approaches approximately zero. In contrast, as m_τ^* decreases both types of likelihood tend to approximately[⋆] zero with lower numbers of events resulting in a faster approach than higher numbers.

Figure 6.3 shows the likelihood function derived from the search data up to and including search point 5. It has an elongated negative tail and a more Gaussian shaped positive end. One can see how it is formed from a product of the shapes described

⋆ All of these approximations would be exact if the background were precisely zero.

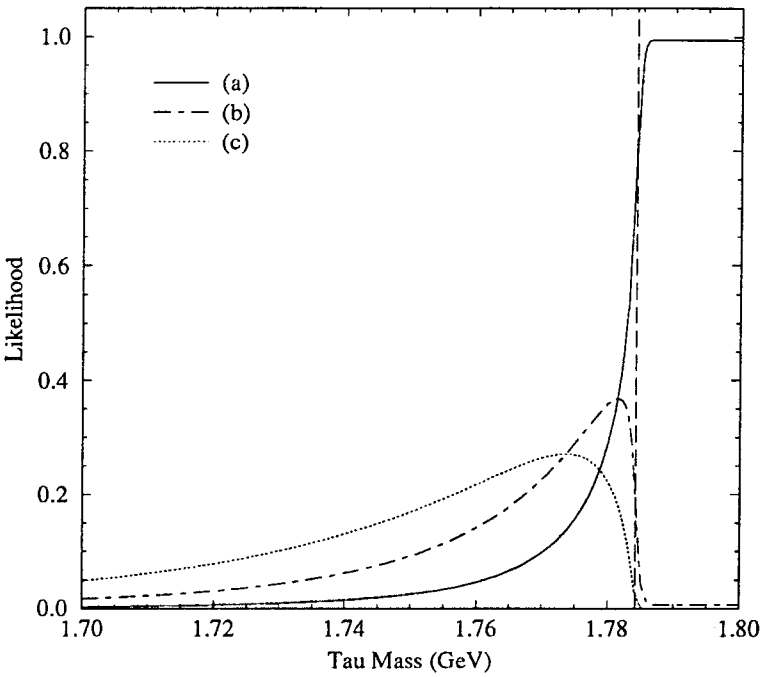

Figure 6.2 A comparison of the likelihood functions due to finding (a) zero, (b) one, and (c) two events at $E_{\text{beam}} = 1784.1$ MeV, $\mathcal{L} = 250\ \text{nb}^{-1}$.

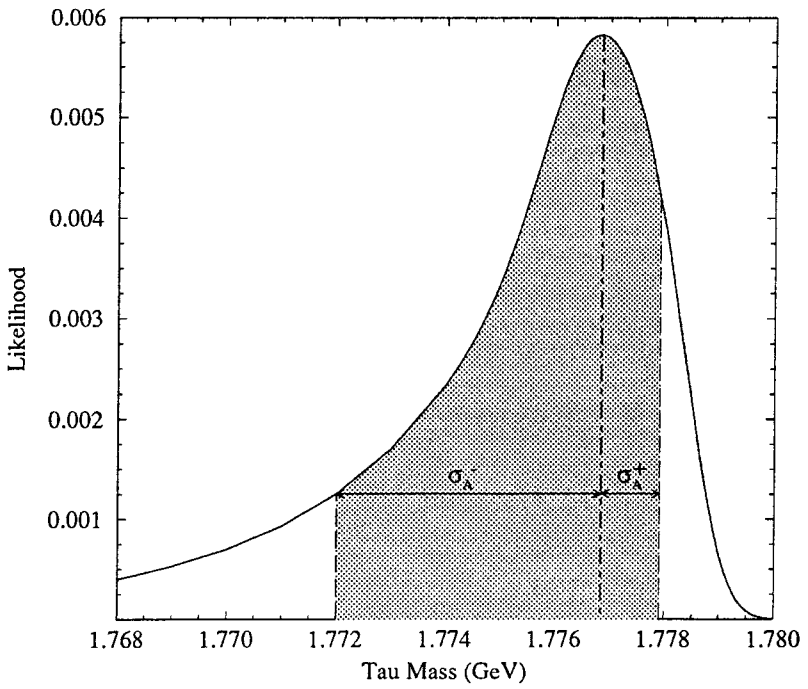

Figure 6.3 Typical likelihood function after 1250 nb^{-1} showing σ_A^- and σ_A^+.

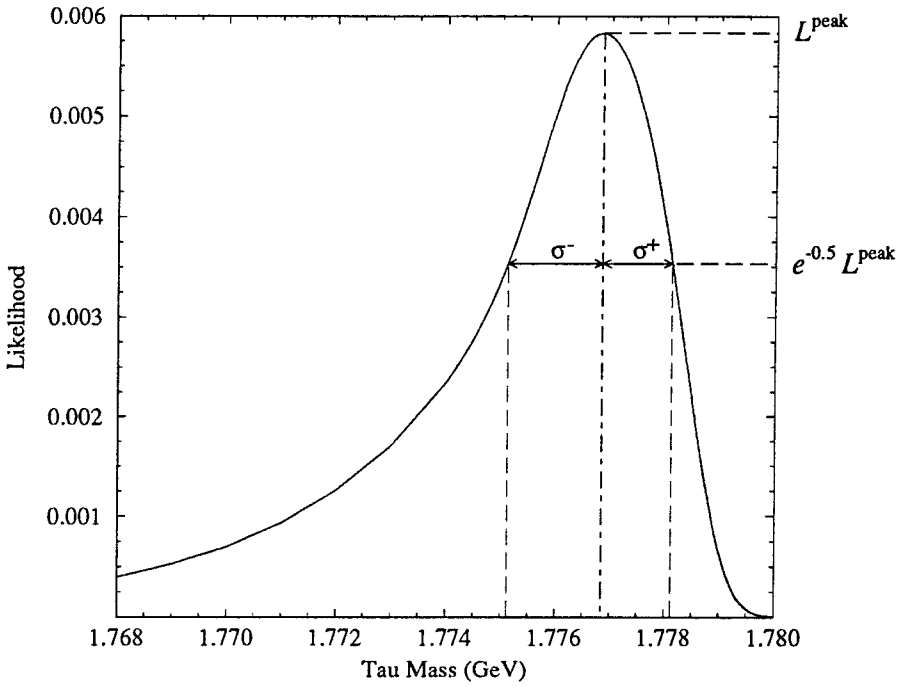

Figure 6.4 Showing σ^- and σ^+ for the same likelihood.

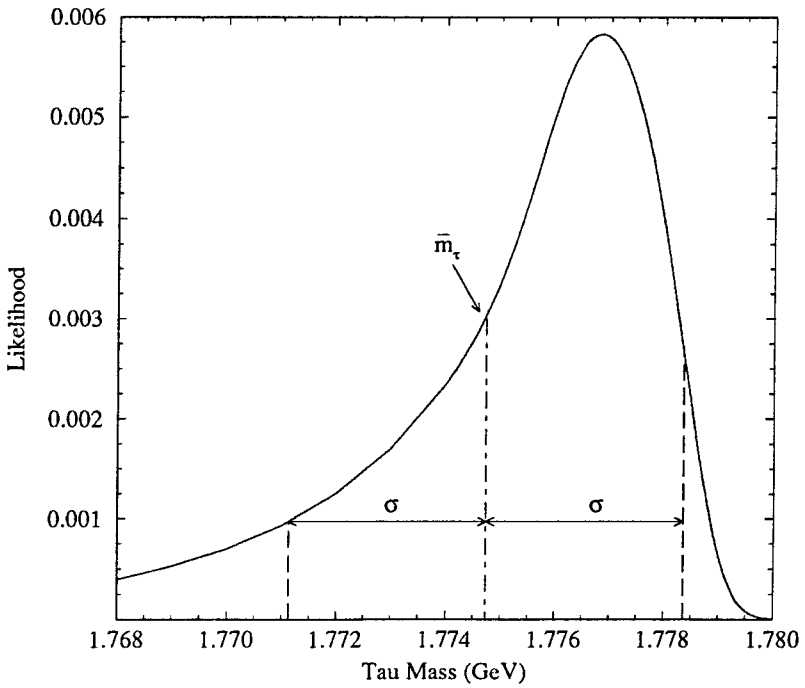

Figure 6.5 Showing the mean and standard deviation of the likelihood.

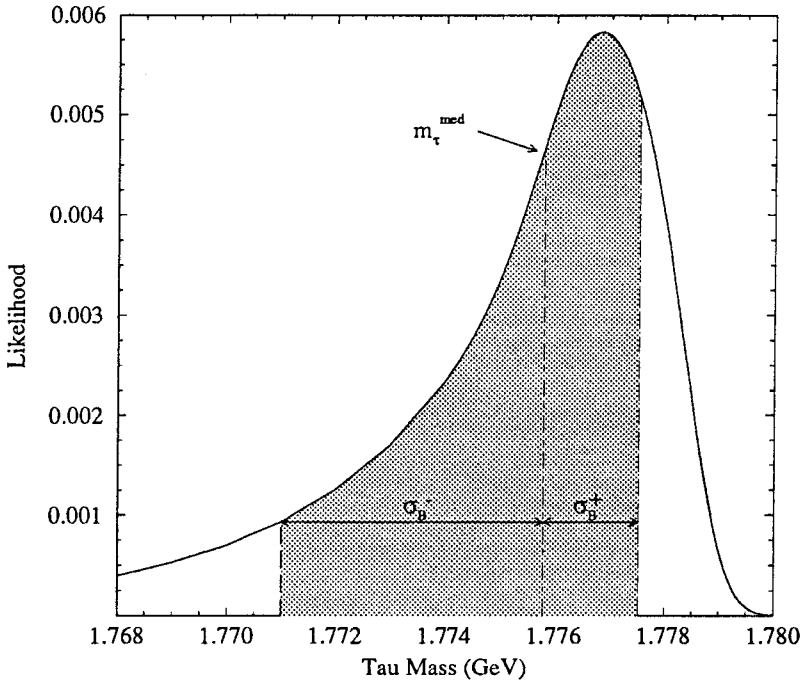

Figure 6.6 Showing the median, σ_B^-, and σ_B^+.

above with the values for E, $\mathcal{L}$, and numbers of detected events from Table 6.1. σ_A^- and σ_A^+ are also indicated on the figure.

As more data is accumulated one may observe that, provided there have been a positive number of events detected at some point in the search, the likelihood assumes the shape shown in Figure 6.1 where the negative width approaches the positive width and the likelihood function becomes almost symmetric.

Figure 6.4 shows the likelihood from Figure 6.3 with the quantities σ^- and σ^+ indicated. Using the same likelihood once again, the mean and standard deviation are shown in Figure 6.5; the median and the area-based widths calculated via the method expounded in Equation (6.10) above are shown in Figure 6.6—the two shaded areas are of equal size and each represent 34.13% of the total area under the graph.

For this typical likelihood we can see that the mean and standard deviation method does not give a good measure of the shape of the likelihood near the beginning of the search. The mean tends to be a long way from the peak and the standard deviation, which by its nature is a single number, cannot measure the different widths in the positive and negative directions.

The median and its associated widths show a little more hope and can be of use under certain unusual situations where the peak, σ^- and σ^+ can be misleading. This will be discussed in Section 6.6.

Section 6.3 Progression of the Likelihood

Given the typical likelihood discussed in Section 6.2 it is natural to consider how it develops with accumulated integrated luminosity, *i.e.*, how does the likelihood progress during a typical search?

Figure 6.7 shows the centre of mass energies from Table 6.1 (in the form of $E_{\text{beam}} = E/2$) plotted against search point and the convergence of the beam energy around the final value for m_τ. (The last two search points are omitted due to the fact that they are not part of the likelihood-driven search, merely extra data taken at fixed energies to help define the final value for κ, see page 29.)

Figures 6.8–6.10 show how the likelihood develops using the algorithm given on page 39 where the likelihoods have been scaled such that they all have height one. One may observe that the initial likelihood is very wide which could have led to the problems observed on page 37 had we not restricted the domain of the search. As more and more data is taken the likelihood becomes more narrow, and the widths of the likelihood (measured by any method) become smaller. Eventually one obtains

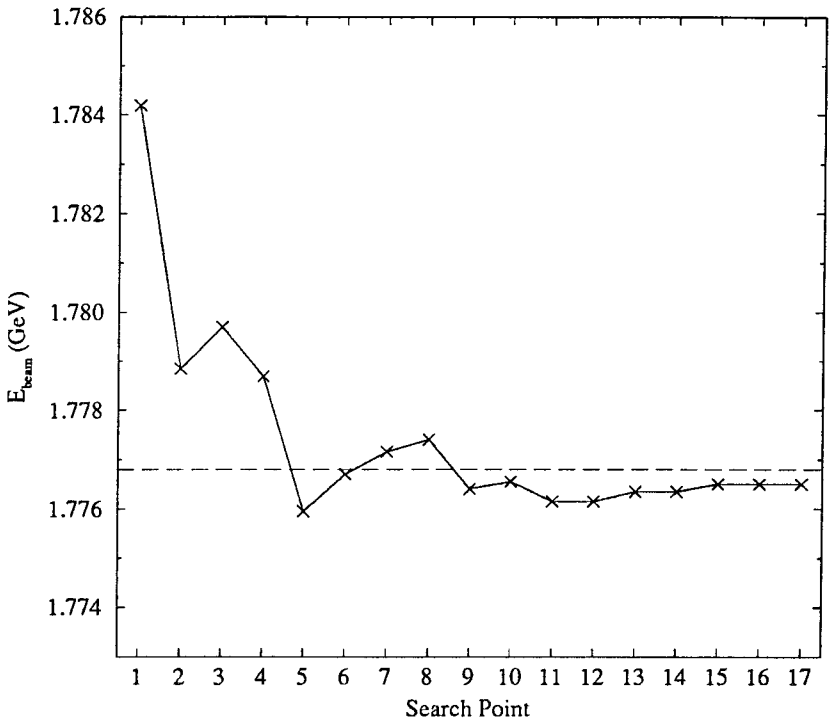

Figure 6.7 Beam energy as a function of search point in a Monte Carlo simulation. The dashed line shows the final value for the tau mass for this search.

the well defined, narrow peak with very small widths of the order of a few tenths of an MeV of Figure 6.1.

Figure 6.10 shows the likelihood after last search point, and after the two extra points at higher energies. One may observe that the addition of these last two points has very little effect on the final likelihood and hence on the estimate for the tau mass.

Tables 6.2 and 6.3 show the values of the previously defined properties of the likelihood function at each stage during the search. Note that

1. all measures of width proceed generally downwards with only temporary departures upwards,

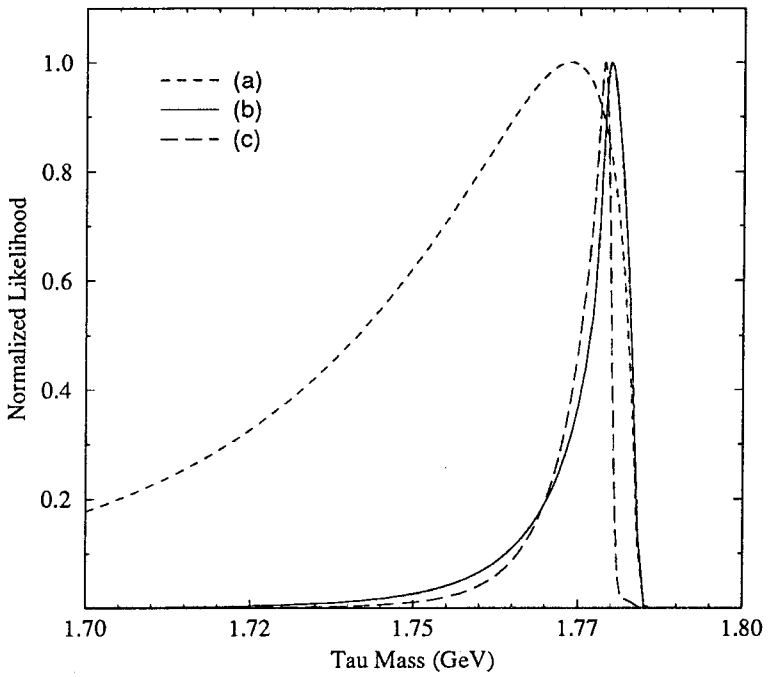

Figure 6.8 The likelihood after search points (a) 1, (b) 2, and (c) 3.

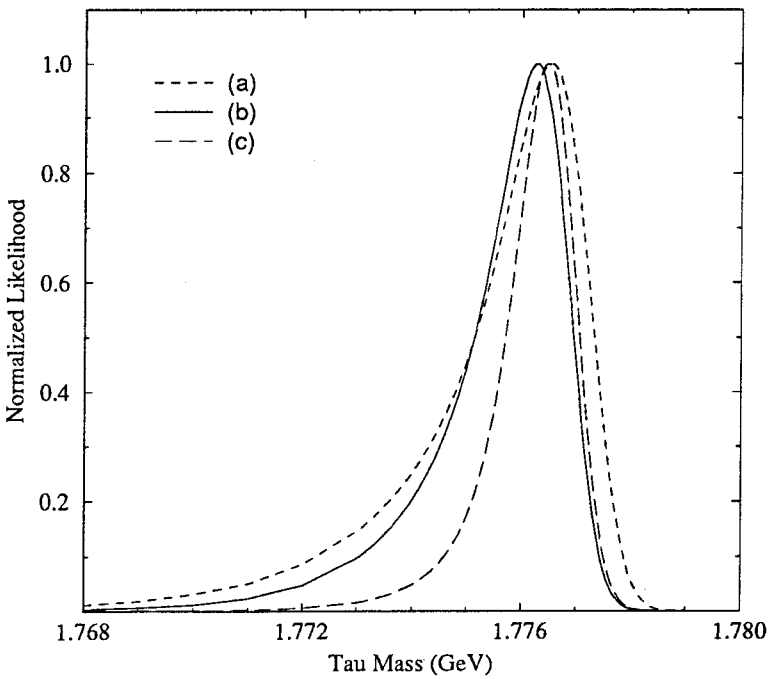

Figure 6.9 The likelihood after search points (a) 8, (b) 10, and (c) 12.

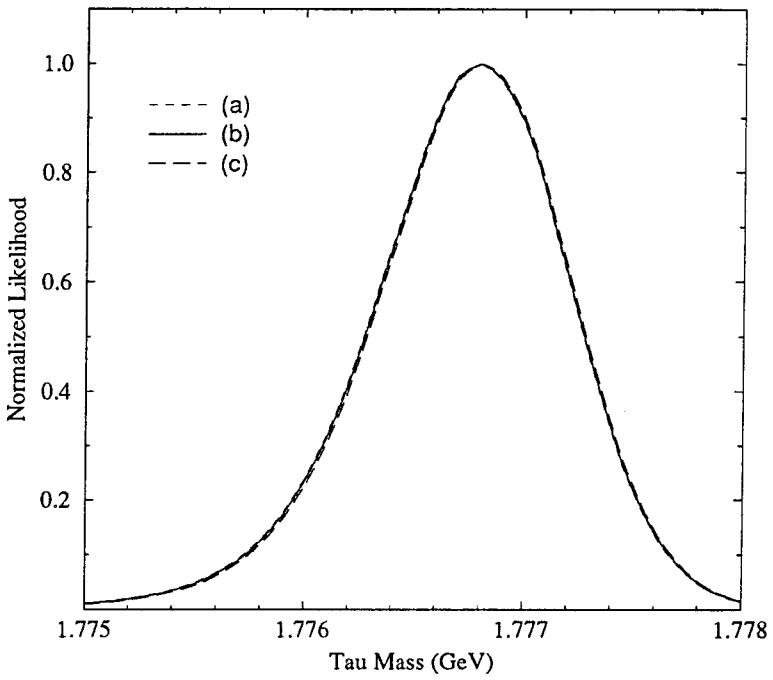

Figure 6.10 The likelihood after search points (a) 17, (b) 18, and (c) 19.

2. typically $\sigma_B^- > \sigma_A^- > \sigma^-$ whereas $\sigma_B^+ > \sigma^+ > \sigma_A^+$,

3. $m_\tau^{\rm med} < m_\tau^{\rm peak}$ throughout the search, but the difference between them decreases with integrated luminosity and at the end of the search they are within 0.1 MeV of one another.

Point 1 shows that the algorithm is converging. This is propitious, but does not guarantee that it is converging on the correct mass. Point 2 is due to the shape of the likelihood—in general it has a long, negative tail and but a sharp, more Gaussian-shaped fall-off on the positive side. Point 3 is in general a very good sign and suggests that the likelihood is converging on the correct value. Likelihoods in which both the peak and the median converge on the wrong mass are very unusual (see Section 6.6 for details).

Search Point	Peak (GeV)	σ^+ (MeV)	σ^- (MeV)	σ_A^+ (MeV)	σ_A^- (MeV)
1	1.77360	8.40	24.60	5.40	49.60
2	1.77985	2.75	2.20	2.25	9.85
3	1.77885	1.00	2.50	0.90	7.85
4	1.77610	1.95	5.10	1.50	8.10
5	1.77685	1.25	1.75	1.05	4.85
6	1.77730	0.95	1.30	0.85	2.10
7	1.77755	0.80	1.05	0.70	1.45
8	1.77655	0.70	1.05	0.65	2.05
9	1.77670	0.60	0.85	0.55	1.40
10	1.77630	0.55	0.95	0.50	1.55
11	1.77635	0.60	0.70	0.50	1.10
12	1.77650	0.50	0.65	0.45	0.90
13	1.77655	0.50	0.55	0.45	0.75
14	1.77665	0.45	0.55	0.40	0.65
15	1.77670	0.45	0.50	0.40	0.60
16	1.77670	0.45	0.40	0.40	0.55
17	1.77680	0.40	0.45	0.40	0.50
18	1.77680	0.40	0.45	0.40	0.50
19	1.77680	0.40	0.45	0.40	0.50

Table 6.2 The peak and widths around the peak of the likelihood after each search point.

Search Point	Mean (GeV)	σ (MeV)	Median (GeV)	σ_B^+ (MeV)	σ_B^- (MeV)
1	1.73787	43.47	1.75100	22.30	51.00
2	1.77429	10.56	1.77780	3.55	11.80
3	1.77393	6.77	1.77600	2.95	8.00
4	1.77129	6.40	1.77200	4.60	7.00
5	1.77474	3.61	1.77575	1.75	4.75
6	1.77622	2.23	1.77670	1.20	2.10
7	1.77693	1.53	1.77720	0.90	1.40
8	1.77539	1.95	1.77585	1.05	2.05
9	1.77601	1.42	1.77630	0.75	1.40
10	1.77547	1.45	1.77580	0.80	1.55
11	1.77588	1.12	1.77605	0.70	1.10
12	1.77614	0.89	1.77625	0.60	0.85
13	1.77632	0.75	1.77640	0.50	0.70
14	1.77646	0.65	1.77650	0.50	0.65
15	1.77656	0.58	1.77655	0.50	0.55
16	1.77665	0.53	1.77665	0.45	0.50
17	1.77672	0.49	1.77670	0.45	0.50
18	1.77673	0.49	1.77670	0.45	0.45
19	1.77674	0.48	1.77670	0.45	0.45

Table 6.3 Other statistical properties of the likelihood after each search point.

Section 6.4 Statistical Measures of the Likelihood

Now that I have studied the progression of one search in detail I can move on to a study of many searches and prove that my selected search is indeed "typical." As mentioned before, 1000 searches were generated using the Monte Carlo program `mctau`. The parameters used to describe the searches were $m_\tau^0 = 1784.1$ MeV, $m_\tau^{\text{true}} = 1776.9$ MeV, $\mu_{\text{exp}} = m_\tau^0$, and $\alpha = 0.04$ MeV/nb^{-1}. The total integrated luminosity was 5 pb^{-1} (as was collected during the true search—see page 116) distributed into 17 search points of 250 nb^{-1} each plus two extra points with integrated luminosities 499.7 and 250 nb^{-1} (see Tables 6.2 and 6.3).

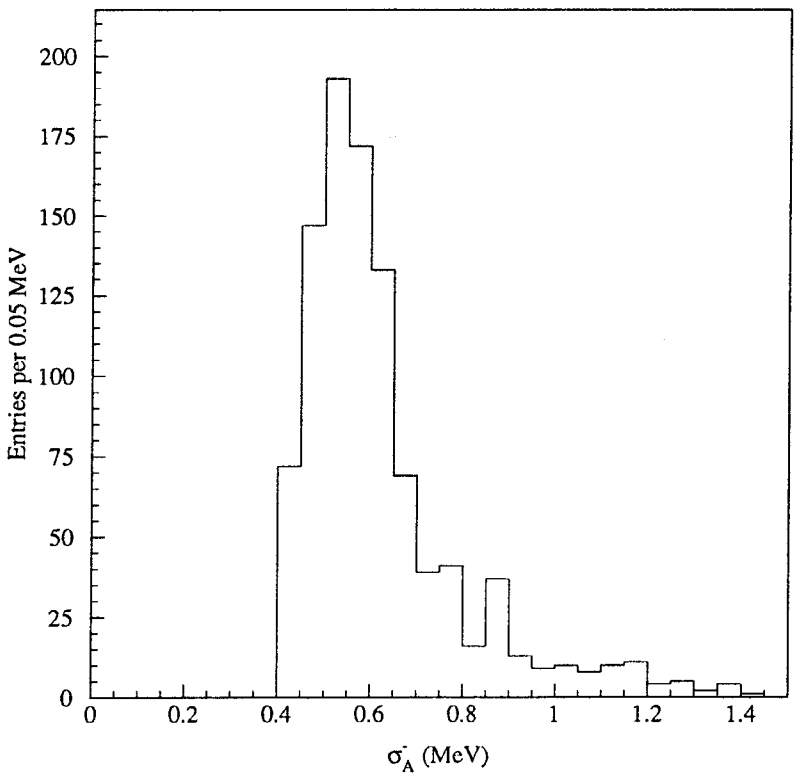

Figure 6.11 The distribution of the final values for σ_A^- for 1000 searches.

A distribution for the 1000 final values of σ_A^- is shown in Figure 6.11. One may

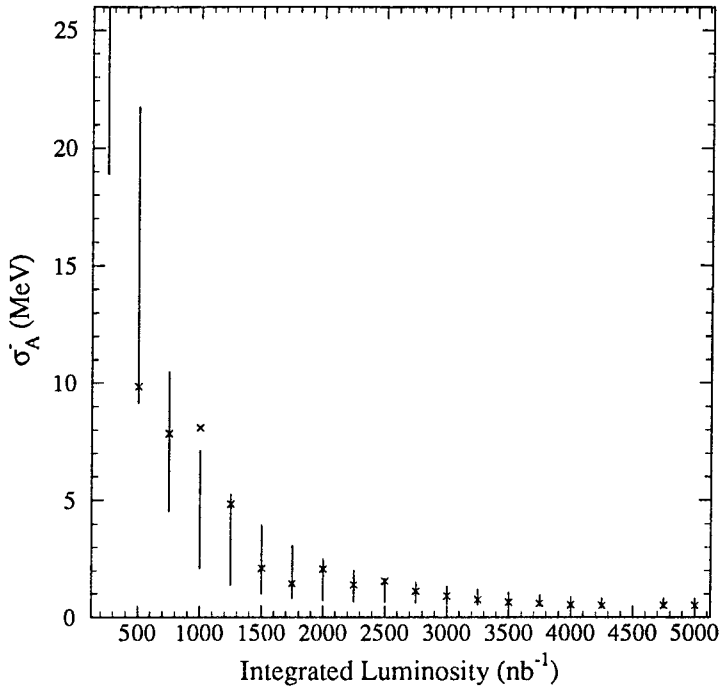

Figure 6.12 The progression of σ_A^- with accumulated integrated luminosity, averaged over 1000 searches.

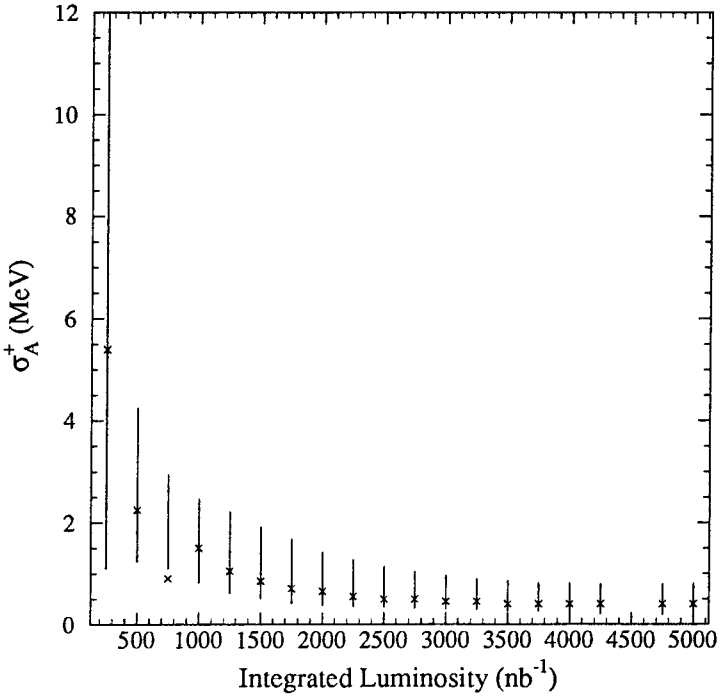

Figure 6.13 The progression of σ_A^+ with accumulated integrated luminosity, averaged over 1000 searches.

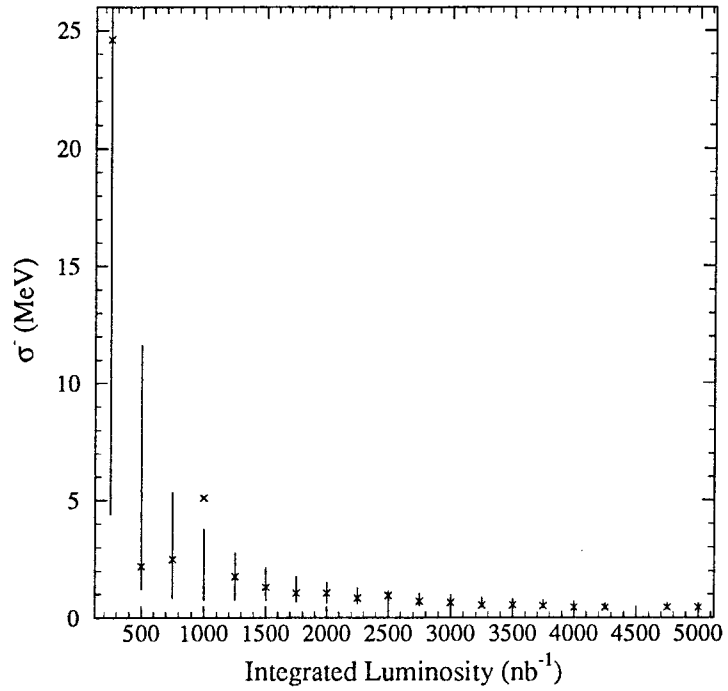

Figure 6.14 The progression of σ^- with accumulated integrated luminosity, averaged over 1000 searches.

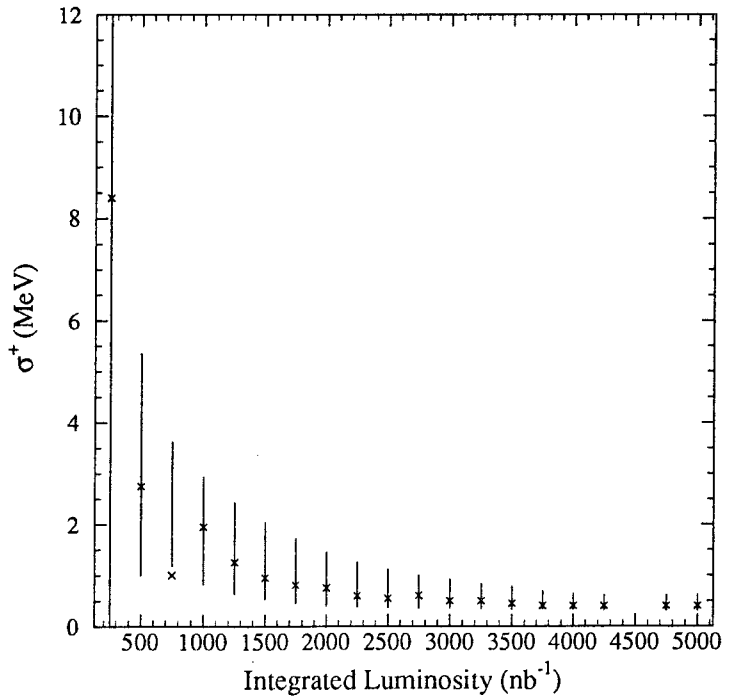

Figure 6.15 The progression of σ^+ with accumulated integrated luminosity, averaged over 1000 searches.

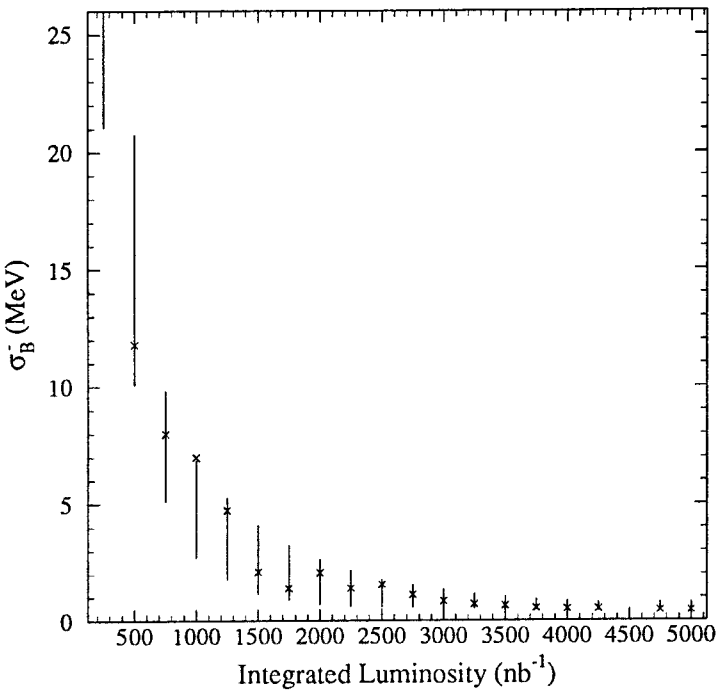

Figure 6.16 The progression of σ_B^- with accumulated integrated luminosity, averaged over 1000 searches.

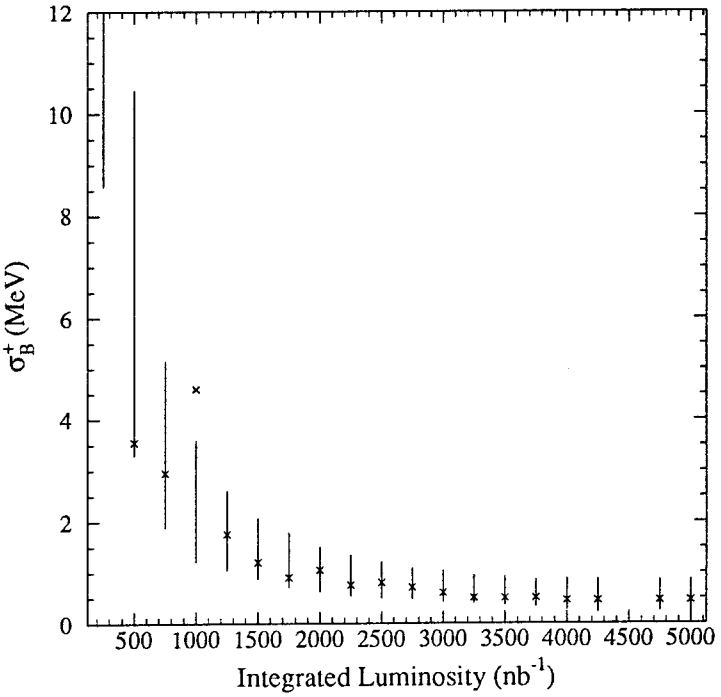

Figure 6.17 The progression of σ_B^+ with accumulated integrated luminosity, averaged over 1000 searches.

observe that the value for my typical search of 0.50 MeV corresponds to approximately the peak of the distribution.

Figures 6.12 and 6.13 show the progression of σ_A^- and σ_A^+ with accumulated integrated luminosity averaged over the 1000 searches. Each vertical bar on the graph represents the mean value for that integrated luminosity plus and minus the root mean square (r.m.s.) of the distribution. The values for my typical search are also plotted (as $\times$'s) and one may observe that those values are within the r.m.s. of the distribution from the mean in all but one case.

For comparison, Figures 6.14–6.17 show the same plots for the value-based widths σ^- and σ^+ and for the area-based widths around the median σ_B^- and σ_B^+. One may observe that all six curves are very similar in shape. They begin with a high positive value with similarly high values for the r.m.s. and approach approximately 0.4 to 0.5 MeV with much smaller values for the r.m.s. as $\mathcal{L}$ approaches 5 pb^{-1}. But, in general, the median-based widths give a larger estimate for the error for any given integrated luminosity and have a larger r.m.s.. This is an indication of the shape of the likelihood—the long negative tail causes negative area-based widths to yield higher values than the value-based one; the positive side is more Gaussian-like but has a sharper cut-off which causes $\sigma_B^+ > \sigma^+ > \sigma_A^+$ as observed before.

The fact that the area-based widths and the value-based widths, both positive and negative, approach one another at the end of the search shows that the likelihoods are becoming Gaussian in shape (see Section 6.1).

On conducting the same experiment with different values for the starting and true masses one finds that, within errors, the average final value of σ_A^- and σ_A^+ is a function only of the difference $(m_\tau^0 - m_\tau^{\text{true}})$ rather than either quantity individually.

Figure 6.18 shows these values with the σ_A^- and σ_A^+ values slightly offset horizontally so that the error bars, which denote the r.m.s. of the distribution, can be distinguished.

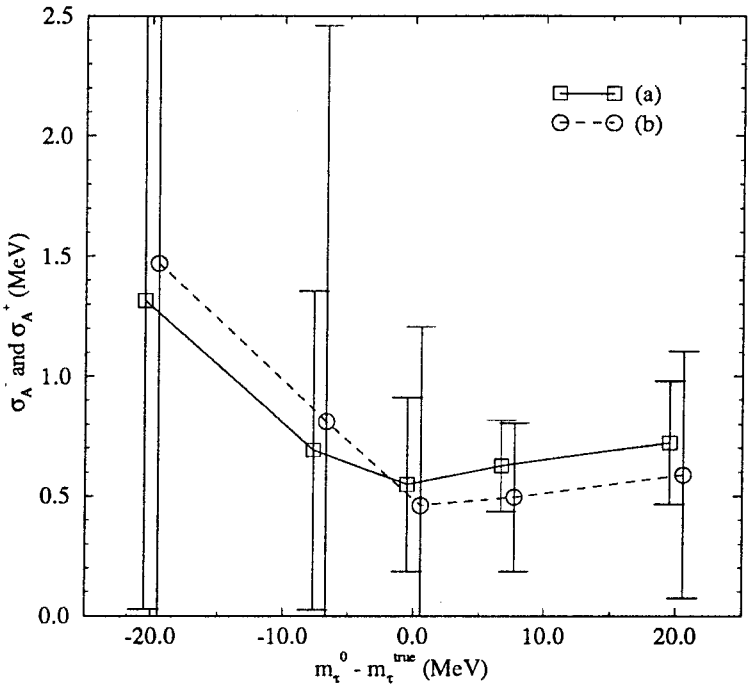

Figure 6.18 The final value of (a) σ_A^- and (b) σ_A^+ as a function of $(m_\tau^0 - m_\tau^{\rm true})$. The error bars show the r.m.s. variation in the two quantities.

One sees that, for $m_\tau^0 > m_\tau^{\rm true}$, the final negative width is larger than the final positive width as was true for the typical search. This is expected given the shape of the likelihoods—although the final peak is sharp and well defined it is not quite Gaussian in that the negative side of the peak approaches zero more slowly than the positive side. However, for $m_\tau^0 < m_\tau^{\rm true}$ the shape of the final likelihood reverses and one finds $\sigma_A^- < \sigma_A^+$.

As might also be expected, the best final value for σ_A^- or σ_A^+ is achieved when you happen to start the search at the true value of the tau mass. This is why the search

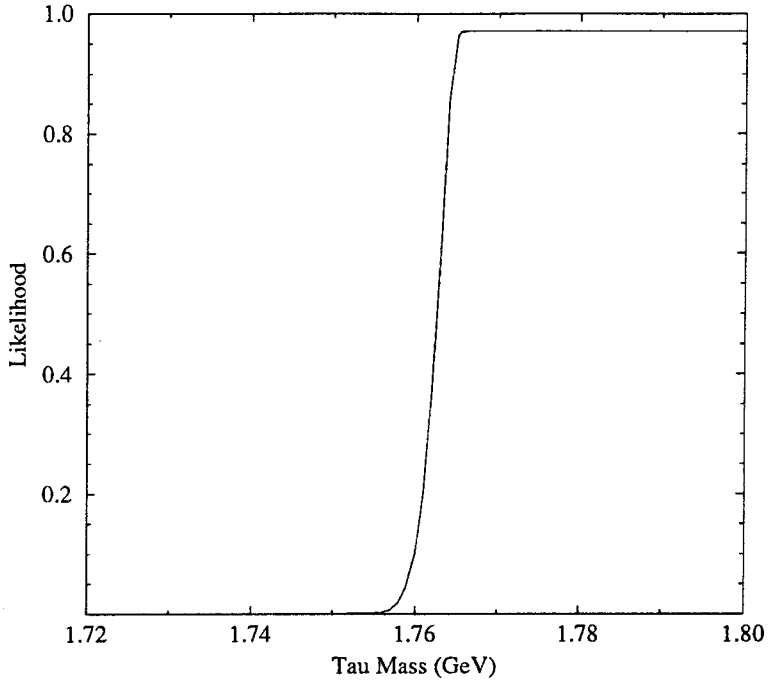

Figure 6.19 A typical likelihood function for $(m_\tau^0 - m_\tau^{\rm true}) = -20$ MeV after 1250 nb^{-1}.

was started at our best estimate for the tau mass at that time, the Particle Data Group value of 1784.1 MeV.[4] However, acceptable values for σ_A^+ and σ_A^- are found provided $(m_\tau^0 - m_\tau^{\rm true}) \gtrsim -10$ MeV. Below this the final values for σ_A^+ and σ_A^- become unacceptably large. This is because if the starting mass is smaller than the true mass by a large amount then limiting the algorithm's energy domain results in a long list of consecutive search points with zero detected events. The likelihood for such a search is shown in Figure 6.19 after 1250 nb^{-1} as before and one can see how the search is experiencing trouble—even after 1250 nb^{-1} the likelihood is still open-ended. In fact for this search 3000 nb^{-1} were needed before an event was found and a clearly defined peak emerged. Hence it is preferable to choose m_τ^0 high than low.

Section 6.5 A Study of the Accuracy

Since I require that the final value of Δ be as small as possible, it is interesting to study its progression and distribution during the search. Figure 6.20 shows the distribution of Δ^{final} for the same 1000 searches as before. The mean of the distribution, the bias b, is 0.08 MeV, the r.m.s. is 0.87 MeV.

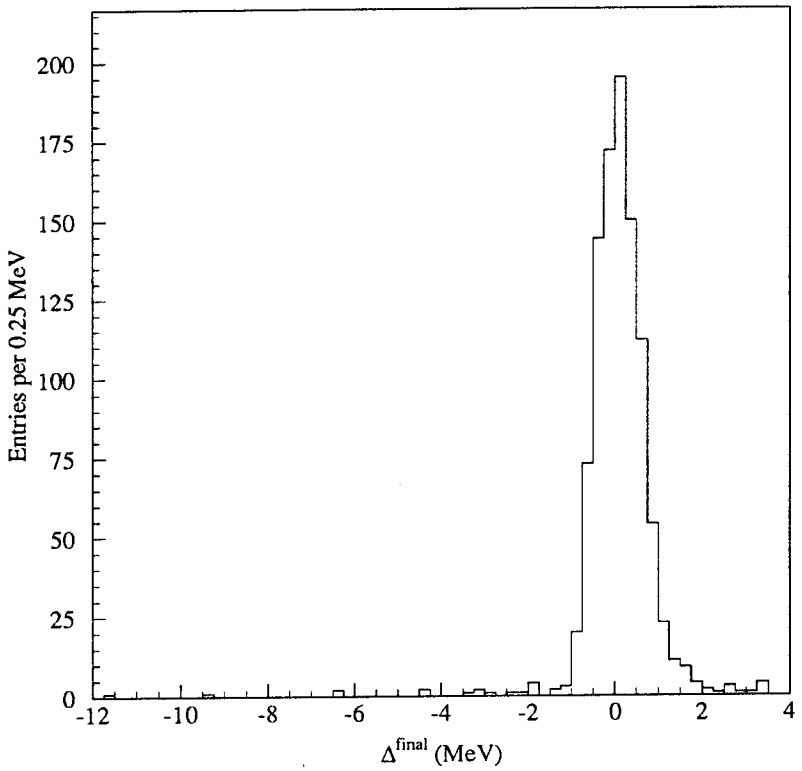

Figure 6.20 The distribution of Δ^{final} for 1000 searches with $m_\tau^0 = 1784.1$ MeV, $m_\tau^{\text{true}} = 1776.9$ MeV, $\mu_{\text{exp}} = m_\tau^0$, and $\alpha = 0.04$ MeV/nb^{-1}.

The ideal distribution for the final accuracy would be $\delta(\Delta^{\text{final}})$, *i.e.*, all experiments report as the final mass the true mass input to the program. One could then guarantee that when applied to the real experiment the answer given at the end of the search would correspond to the true mass of the tau lepton. In practice this

Monte Carlo Parameters				Final Accuracy*	Widths*	
m_τ^0 (MeV)	m_τ^{true} (MeV)	μ_{exp} (MeV)	α (MeV/nb^{-1})	Δ^{final} (MeV)	σ_A^+ (MeV)	σ_A^- (MeV)
1756.9	1776.9	1756.9	0.04	0.15 ± 3.71	1.47 ± 2.79	1.32 ± 1.29
1769.7	1776.9	1769.7	0.04	0.16 ± 1.42	0.81 ± 1.65	0.69 ± 0.66
1776.9	1776.9	1776.9	0.04	0.13 ± 1.06	0.46 ± 0.74	0.55 ± 0.37
1784.1	1776.9	1784.1	0.04	0.08 ± 0.87	0.49 ± 0.31	0.63 ± 0.19
1796.9	1776.9	1796.9	0.04	0.09 ± 1.07	0.59 ± 0.52	0.72 ± 0.26
1784.1	1776.9	1784.1	0.08	-0.01 ± 1.21	0.59 ± 0.58	0.67 ± 0.23
1784.1	1776.9	1784.1	0.02	0.12 ± 0.68	0.46 ± 0.16	0.63 ± 0.18

Table 6.4 Δ^{final}, σ_A^+, and σ_A^- for various expanding Gaussian algorithms.

goal remains unattainable. I shall allow for possible differences between m_τ^{final} and m_τ^{true} via the statistical uncertainty in Section 8.3 and for uncertainty in m_τ due to uncertainty in the bias by including an estimate of the uncertainty in the bias over many different algorithms into the systematic uncertainty in Section 8.4.

Table 6.4 shows a compilation of the values of Δ^{final}, σ_A^+, and σ_A^- for a variety of starting parameters using the expanding Gaussian algorithm.* Note that while small values for the bias (the average of Δ^{final}) are desirable, one must also consider σ_A^+ and σ_A^- and their effect on the statistical uncertainty. In particular, the value for the bias in row 6 of Table 6.4 would would lead one to propose running with a Gaussian which expands very fast. However, this also leads to larger values for σ_A^+ and σ_A^- which in turn imply a larger statistical uncertainty.

---

* The values quoted are the average plus or minus the r.m.s. of the distribution of 1000 Monte Carlo experiments. The uncertainty in the mean itself can be estimated as r.m.s./$\sqrt{1000}$.

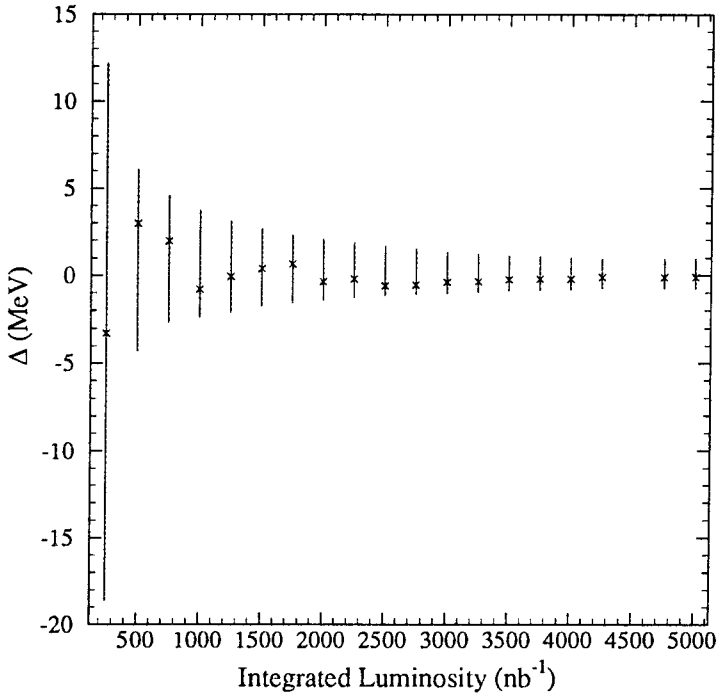

Figure 6.21 The progression of Δ with integrated luminosity for $m_\tau^{\text{true}} = 1776.9$ MeV, $m_\tau^0 = 1784.1$ MeV averaged over 1000 searches.

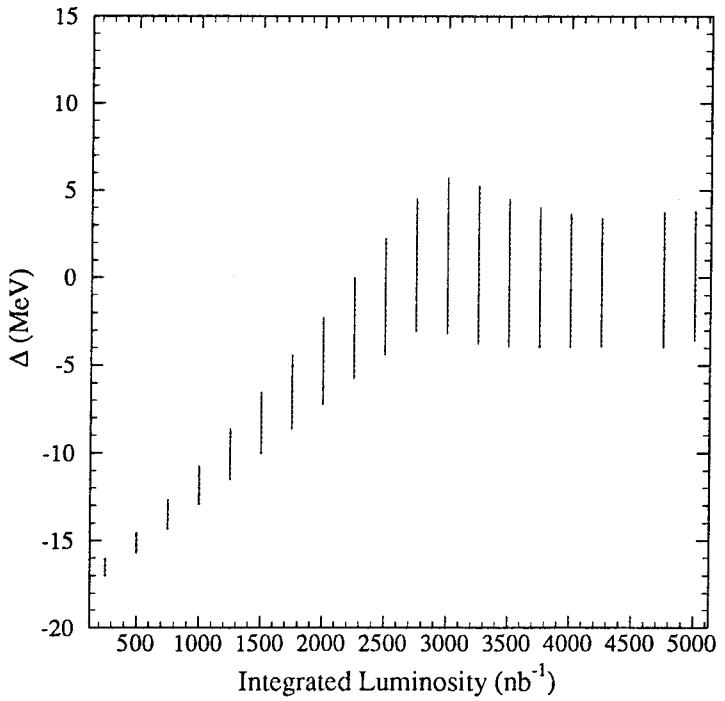

Figure 6.22 The progression of Δ with integrated luminosity for $m_\tau^{\text{true}} = 1776.9$ MeV, $m_\tau^0 = 1756.9$ MeV averaged over 1000 searches.

The progression of Δ with integrated luminosity is shown in Figure 6.21 where the same convention has been adopted for the error bars as for Figures 6.12 and 6.13, *i.e.*, the error bars represent the r.m.s.. Also included are the points of my typical search for comparison with the distribution as before.

The way in which the accuracy progresses is very much a function of $(m_\tau^0 - m_\tau^{\rm true})$ and, for comparison, Figure 6.22 shows the same plot for 1000 searches with $m_\tau^0 =$ 1756.9 MeV (all other parameters the same).

For $m_\tau^0 = 1784.1$ MeV the average accuracy starts slightly negative but rapidly approaches zero and the r.m.s. of the distribution shrinks as more integrated luminosity is accumulated. In contrast, for $m_\tau^0 = 1756.9$ MeV the average is initially well below zero and the r.m.s. is relatively small. The average only reaches zero around 3000 $\rm nb^{-1}$ and the r.m.s. increases up to this point. After that the r.m.s. remains fairly constant. The final values for the average and the r.m.s. are 0.08 and 0.87 MeV for Figure 6.21 and 0.15 and 3.71 MeV for Figure 6.22. This emphasizes that one should choose m_τ^0 high enough to avoid this problem.

Section 6.6 Correlations and Problem Likelihoods

It is important that the experiment have accurate measures of uncertainty. For instance if Δ is large and negative then our measure of the positive width should also be large; similarly for large, positive accuracies the negative width measure should be large. Here I consider correlations between Δ, σ^+ and σ^- and show why they are less suitable than the area-based measures.

An investigation of Algorithm 1 (see page 37) with unlimited energy domain exemplifies some of the problems which can occur with respect to Δ–σ^+–σ^- cor-

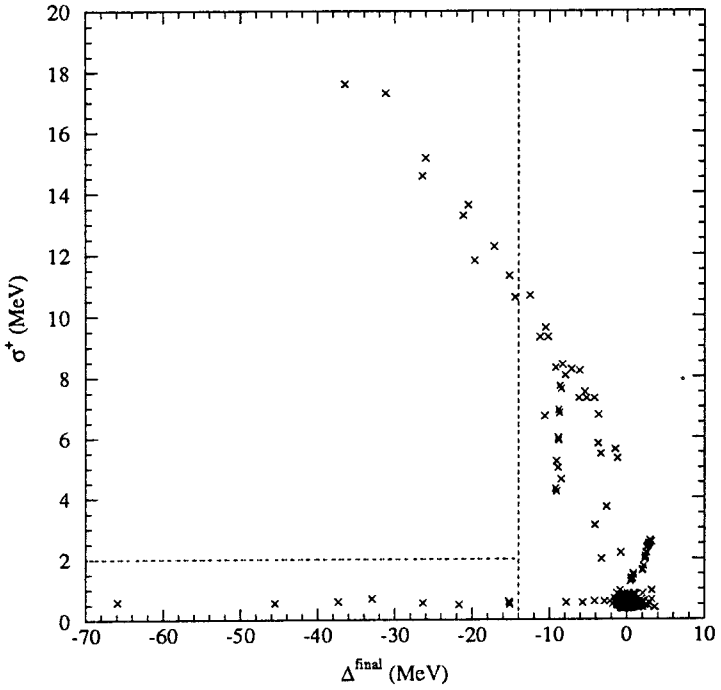

Figure 6.23 σ^+ versus Δ^{final} for 1000 searches with an unlimited energy domain.

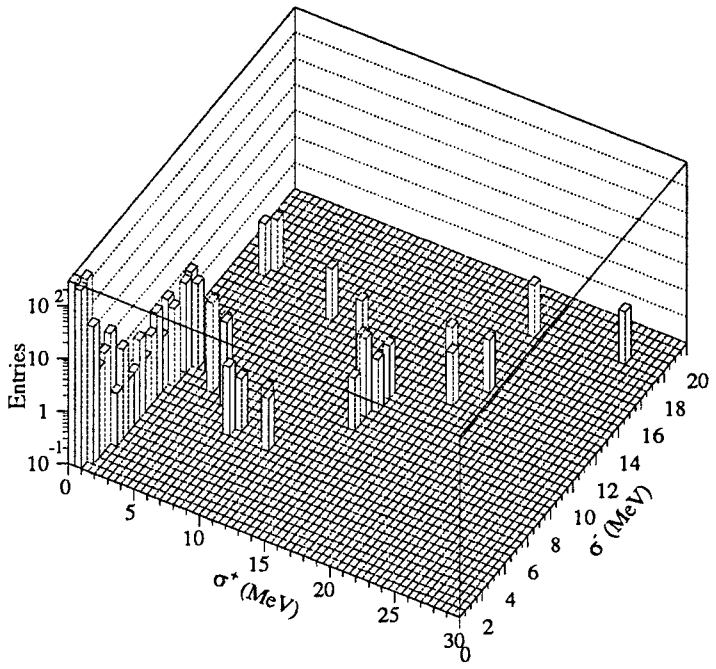

Figure 6.24 σ^+ versus σ^- for the same 1000 searches.

relations. Figure 6.23 shows a scatter plot of σ^+ versus Δ for 1000 searches with unlimited energy domain. Figure 6.24 shows the correlation of σ^+ with σ^- for the same 1000 experiments (note the logarithmic scale for the number of entries).

In Figure 6.23, most of the points are clustered around $\{\Delta = 0, \sigma^+ = 0.5\}$. However there are two groups with large, negative accuracies: one group has a very small σ^+ independent of Δ; the other has σ^+ negatively correlated with Δ. In References 75 and 76 F. C. Porter and myself investigated these tails in some detail and I will present the results below.

Figure 6.24 shows that the vast majority of experiments, 94.5%, lie within the region $\sigma^- < 2$ MeV, $\sigma^+ < 1$ MeV. These are correlated with the group of experiments I mentioned above with $\{\Delta = 0, \sigma^+ = 0.5\}$. However, there are some tails with large σ^+ which correspond to the correlated group mentioned in the last paragraph. Note that there are no experiments with a large value for σ^+ and a small value for σ^-.

To investigate these tails consider only those searches with $\Delta < -14.0$ MeV. Subdividing the remaining searches along the line $\sigma^+ = 2.0$ MeV as shown by the dashed lines in Figure 6.23 yields two groups clearly exhibiting the features that I wish to investigate: 13 in the correlated group (group 1) and 9 in the uncorrelated group (group 2). It is this latter group which are particularly worrisome—the accuracy is large and negative and so the algorithm has given a very bad result, yet the positive width would lead one to believe that this wrong result is a good one.

However, if one studies the final likelihood function for a typical such search, as shown in Figure 6.25, one sees immediately what the problem is: a large spike has appeared at a low mass. This spike is higher than the wide bump which has a peak closer to the correct mass. The peak of the likelihood was found at the spike

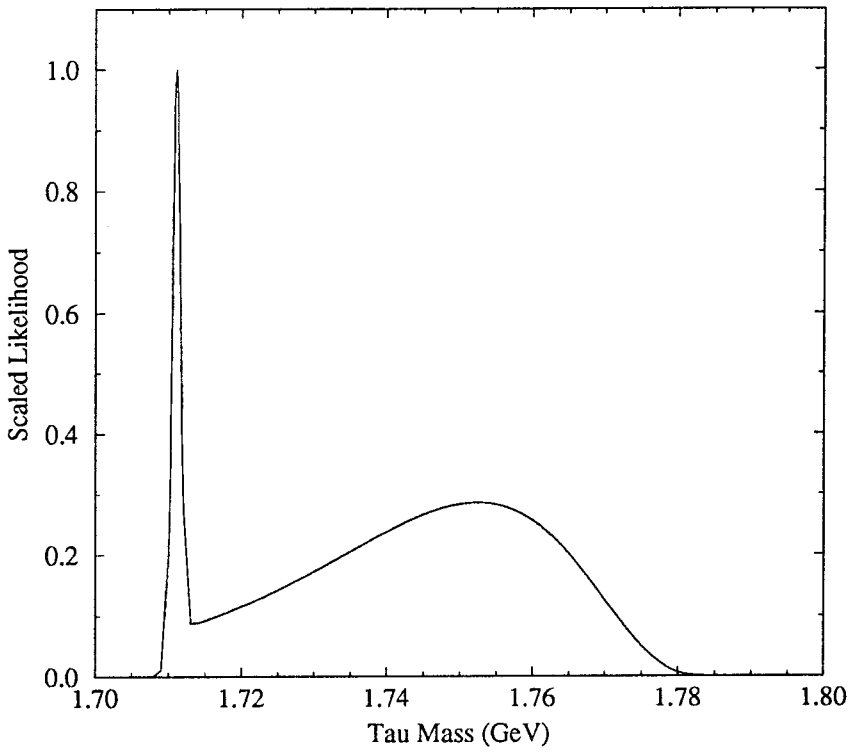

Figure 6.25 Typical likelihood function for a search resulting in σ^+ and Δ^{final} being uncorrelated.

and the likelihood was searched in both directions until the nearest points at which $\ln \mathcal{L} = \ln \mathcal{L}^{\text{peak}} - \frac{1}{2}$ were found; σ^+ and σ^- were calculated from those points. Hence σ^+ and σ^- only characterize the spike at the left and not the whole likelihood.

It is under these circumstances that the median can give a better estimate of m_τ than the peak and the area-based widths can give better results than σ^+ and σ^-. In this particular case we find $m_\tau^{\text{peak}} = 1711.0$ MeV, $\sigma^+ = 0.6$ MeV, and $\sigma^- = 0.5$ MeV whereas $\sigma_A^+ = 42.0$ MeV, $\sigma_A^- = 0.6$ MeV. Results around the median are $m_\tau^{\text{med}} = 1744$ MeV, $\sigma_B^+ = 16$ MeV, and $\sigma_B^- = 25$ MeV.

Whenever the peak and the median disagree by a large amount it is a signal to investigate the likelihood in more detail. Note also the considerable disagreement be-

tween σ_A^+ and σ^+. This is due to their different methods of calculation: σ_A^+ represents a measure of the positive width of the whole likelihood where σ^+ merely characterizes the peak. This too is a symptom of a likelihood function that requires investigation.

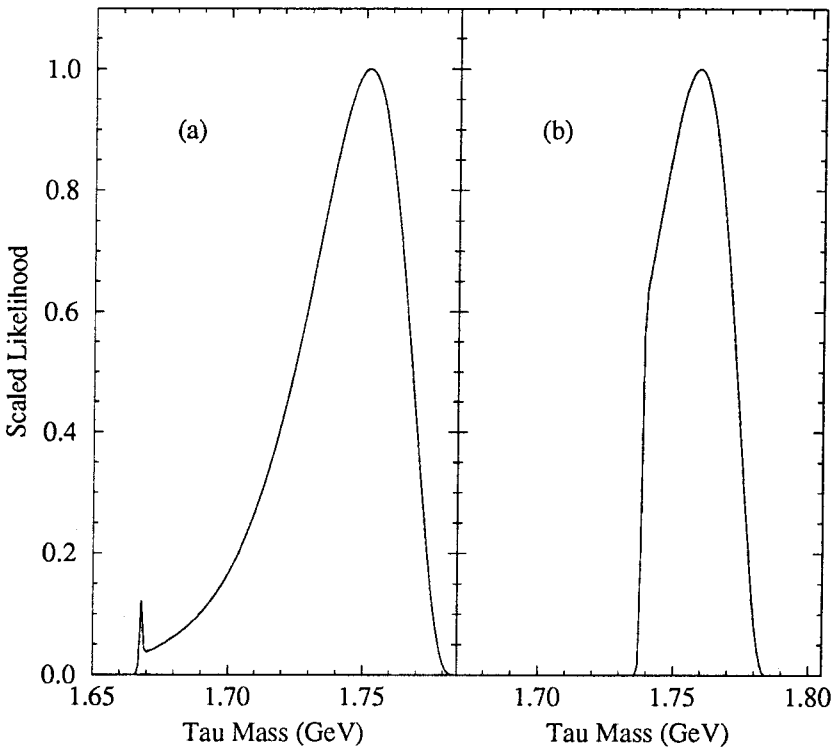

Figure 6.26 Typical likelihood functions from two searches resulting in σ^+ and Δ^{final} being correlated.

Group 1, those experiments which had σ^+ and Δ correlated, can be subdivided into two further groups, (a) and (b), by studying the likelihood functions. Typical examples of those two likelihoods are shown in Figure 6.26. Group 1(a) is similar to the likelihood for group 2 except that the spike is lower than the wider bump. Group 1(b) shows no spike of any sort but is still very wide for a final likelihood (tens of MeV).

Investigation of these three groups shows that they are caused by the following effects. All three groups show a disproportionately large number of events very early in the search (usually at the first search point). However, the groups can be distinguished by the number and distribution of background events* observed:

1(a). a background event is observed "early" in the search,

1(b). zero background events are observed in the whole search,

2. a background event is observed "late" in the search.

Note that all three groups depend on the unusually large number of events being found at search point 1 (or occasionally point 2), *i.e.*, a large, positive Poisson fluctuation in the number of events. This explains both (i) why there are so few such searches—because such a Poisson fluctuation has a very small probability, and (ii) why these searches have very large, negative accuracies—because with an unlimited energy domain a large number of events at search point 1 causes E_2 to be very low; in one case a value of $E_2 = 2(m_\tau^0 - 119)$ MeV was observed. The algorithm never recovers and the energy region in which data is accumulated is well below $m_\tau^{\rm true}$.

Given that a large Poisson fluctuation has taken place and that E_2 is very low, one would expect to observe zero events throughout the remainder of the search. If that happens one obtains a likelihood similar to that in Figure 6.26(b)—the accuracy is large and negative, but σ^+ is also large. Hence the uncertainty that one would quote using this quantity is large and the experiment, while not very successful, does not present unrealistic uncertainties.

If a background event is found "early" in the search then the algorithm has time to recover; the likelihood assumes a shape similar to that in Figure 6.26(a) with a

* A background event is one which is mistakenly detected as a $\tau^+\tau^-$ event, see Section 7.2.

spike smaller than the bump at higher mass, and once again the uncertainties quoted are realistic.

However, if the background event is found "late" in the search then a large spike is generated in the likelihood (see Reference 76 for details) and unrealistic uncertainties would be quoted.

The definitions of "early" and "late" in the above descriptions are somewhat loose—they depend on the size of the initial Poisson fluctuation and, to a lesser extent, on the numbers of events found at the two fixed, higher energies. But a definite analysis can be made by considering the shape of the likelihood function.

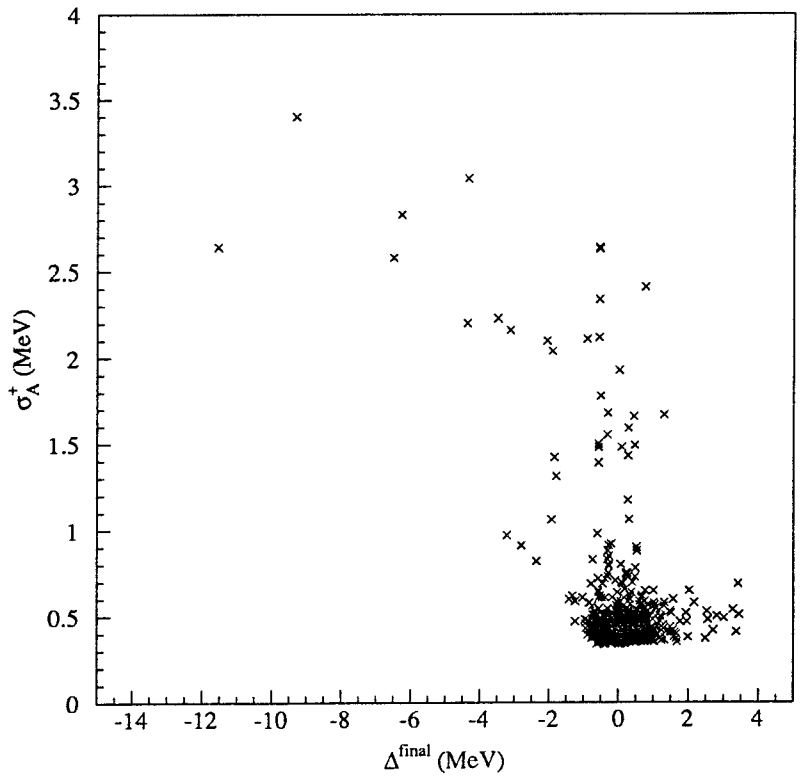

Figure 6.27 σ_A^+ versus Δ^{final} for 1000 searches using a limited energy domain.

Given these descriptions and remembering that they describe only a small percentage of the 1000 searches, one may observe that it is easy to tell whether the final likelihood from the real experiment falls into one of the above categories and to further investigate the size of the uncertainties if it does.

The necessity of limiting the energy domain for the algorithm and for using area-based widths is proven and Figure 6.27 shows the scatter plot of σ_A^+ versus Δ^{final} for Algorithm 2 with the expanding Gaussian method of limiting the energy domain. Comparing this plot with Figure 6.23 clearly shows the success of the restriction and also of using the area-based width σ_A^+ rather than σ^+. The whole scale of the plot is much smaller, *i.e.*, much smaller accuracies have resulted, and the tails at low positive width but large, negative accuracy have disappeared.

Section 6.7 Alternative Search Algorithms

As was mentioned in Section 5.1, the use of the likelihood function to define an estimate for m_τ is independent of how the energies for the various search points are selected. Here I present two methods of selecting the energies, both different from the likelihood-driven search used so far throughout this thesis. I also present a different method of limiting the energy domain; until now the expanding Gaussian method has been the only one mentioned.

In all cases the likelihood function is generated as detailed in Section 5.2 and the distributions for Δ^{final}, σ_A^+, and σ_A^- are compared.

A Progressive Scan

The simplest search is one which selects the next running energy via the formula $E_{i+1} = E_i + \Delta E$ where ΔE is a constant regardless of the number of events detected.

In this way one steps through the region each energy a constant from the one before. I shall call this type of search a progressive scan.

Monte Carlo Parameters			Final Accuracy	Widths	
$E_9/2$ (MeV)	m_τ^{true} (MeV)	ΔE (MeV)	Δ^{final} (MeV)	σ_A^+ (MeV)	σ_A^- (MeV)
1756.9	1776.9	1.25	0.05 ± 9.69	5.67 ± 3.15	6.98 ± 3.78
1769.7	1776.9	1.25	3.68 ± 5.64	3.97 ± 1.57	4.27 ± 2.99
1776.9	1776.9	1.25	0.20 ± 0.90	0.71 ± 0.50	1.02 ± 0.14
1784.1	1776.9	1.25	-0.20 ± 2.09	1.38 ± 0.61	3.56 ± 1.28
1796.9	1776.9	1.25	-0.19 ± 4.91	3.30 ± 0.70	7.25 ± 1.16
1756.9	1776.9	2.50	1.09 ± 8.32	5.14 ± 2.49	6.98 ± 3.78
1769.7	1776.9	2.50	0.97 ± 2.88	1.58 ± 1.81	1.85 ± 1.06
1776.9	1776.9	2.50	0.42 ± 1.39	0.91 ± 0.24	1.56 ± 0.30
1784.1	1776.9	2.50	0.48 ± 1.31	0.91 ± 0.28	1.64 ± 0.46
1796.9	1776.9	2.50	-0.19 ± 4.55	3.06 ± 0.75	6.93 ± 1.23

Table 6.5 Δ^{final}, σ_A^+, and σ_A^- for 20 and 40 MeV wide progressive scans at 5 different starting energies.

Table 6.5 shows the results for Δ^{final}, σ_A^+, and σ_A^- as were presented for the expanding Gaussian algorithm in Table 6.4. Each search has 17 search points with 250 nb^{-1} as before (the two additional points at higher energies are also added in for consistency). Each row in the table is an average over 1000 searches. The parameters describing each search are shown in the table. E_9 is the central energy of the search (since there are seventeen search points). The starting energies, E_1, are evaluated via $E_1 = E_9 - 8\Delta E$. The set of values for $E_9/2$ is $\{1756.9, 1769.7, 1776.9, 1784.1, 1796.9\}$,

the same set of values for m_τ^0 used for the expanding Gaussian algorithm in Table 6.4. This is so that the two can be directly compared.

The first set of five rows in Table 6.5 has $\Delta E = 1.25$ MeV corresponding to a total width for the scan of $(17-1)\Delta E = 20$ MeV. The second set has $\Delta E = 2.5$ MeV and hence a total width of 40 MeV.

On comparing the results with Table 6.4, one immediately observes that the expanding Gaussian yields far better results, particularly for σ_A^+ and σ_A^-, in all cases. Even if one is lucky enough to scan around exactly the correct mass the positive and negative widths have larger average values and wider distributions. The bias also has a wider distribution and is centred farther from zero. If one is not lucky the results become rapidly worse.

The major problem with this method is that the algorithm spends a lot of time outside of the region in which one is interested. Hence most of the data is insensitive to the true tau mass and the statistical uncertainty for any fixed luminosity is larger than that from the likelihood-driven method.

A Binary Search

A binary search can be defined as follows: pick two energies, E_a and E_b, which (one hopes) bracket the true tau mass. The first search energy is $E_1 = \frac{1}{2}(E_a + E_b)$. One runs long enough to accumulate a set integrated luminosity $\mathcal{L}$ (in this case 250 nb^{-1}) at this energy. If zero events are found one assumes threshold is higher than E_1 and the next energy is given by $E_2 = \frac{1}{2}(E_1 + E_b)$. Otherwise threshold is assumed lower than E_1 and E_2 is given by $\frac{1}{2}(E_a + E_1)$. One continues in this fashion hoping that at any given time the two endpoint energies bracket the true tau mass.

Monte Carlo Parameters			Final Accuracy	Widths	
$E_1/2$ (MeV)	m_τ^{true} (MeV)	ΔE_{binary} (MeV)	Δ^{final} (MeV)	σ_A^+ (MeV)	σ_A^- (MeV)
1756.9	1776.9	10.0	-0.65 ± 10.0	6.15 ± 3.81	7.51 ± 4.68
1769.7	1776.9	10.0	3.61 ± 5.53	3.96 ± 1.63	3.47 ± 3.15
1776.9	1776.9	10.0	0.33 ± 1.21	0.66 ± 0.98	1.18 ± 0.75
1784.1	1776.9	10.0	0.16 ± 1.97	1.36 ± 0.56	2.90 ± 1.16
1796.9	1776.9	10.0	-0.10 ± 4.40	3.04 ± 0.54	6.58 ± 1.04
1756.9	1776.9	20.0	0.21 ± 8.42	5.49 ± 2.95	5.65 ± 4.16
1769.7	1776.9	20.0	0.13 ± 0.82	0.55 ± 0.73	0.94 ± 0.39
1776.9	1776.9	20.0	0.39 ± 1.26	0.90 ± 1.15	1.49 ± 0.99
1784.1	1776.9	20.0	0.33 ± 1.80	1.00 ± 0.73	2.16 ± 1.57
1796.9	1776.9	20.0	-0.15 ± 3.85	2.69 ± 0.49	5.75 ± 1.10

Table 6.6 Δ^{final}, σ_A^+, and σ_A^- for binary search algorithms with $\Delta E_{\text{binary}} =$ 10 and 20 MeV for five different starting energies.

Table 6.6 shows the results for Δ^{final}, σ_A^+, and σ_A^- using this algorithm. For each set of 1000 simulated searches E_a was set $E_1 - \Delta E_{\text{binary}}$ and E_b was set to $E_1 + \Delta E_{\text{binary}}$. In this way binary searches were conducted in a region $2\Delta E_{\text{binary}}$ wide (in this case 20 and 40 MeV as for the progressive scan) around each of the list of values for m_τ^0, $\{1756.9, 1769.7, 1776.9, 1784.1, 1796.9\}$, that I mentioned before.

On comparing the results with Table 6.4, one again observes that the expanding Gaussian yields far better results in all cases. For values of $E_1/2$ far from m_τ^{true} there are no search points close to tau threshold. This causes Δ^{final}, σ_A^+, and σ_A^- to have very wide distributions as reflected by their values for the r.m.s. of their distributions in the table.

However, even for values of $E_1/2$ close to m_τ^{true}, this method has some fatal flaws: either a background event at an energy where one should detect zero events or a Poisson fluctuation of the number of detected events to zero at an energy where one would expect a non-zero number will cause the energy at that point to be the closest the algorithm ever comes to finding the true value of m_τ. The smaller one chooses $\mathcal{L}$, the more often this latter will occur.

Limiting the Search

As was noted in Section 5.4 the pure likelihood method described by Algorithm 1 requires limitations to be placed on the difference in energy between the first and second (and perhaps subsequent) search points; otherwise the algorithm is prone to provide too extreme a response to the number of events found. In effect some time is needed for the algorithm to "settle down." However one must be careful not to limit the algorithm too much or the correct energy will never be reached.

Two algorithms whose effect is to restrict $|E_{i+1} - E_i|$ were explored: the first was the expanding Gaussian algorithm used on page 39, the second depends upon limiting the maximum energy between one search energy and the next as explained in Algorithm 3 below (where $E_{\text{cand}} = 2m_\tau^{\text{peak}} - \delta$ as on page 37 and Δ_{max} is a constant).

The original procedure has the advantage of allowing an ever widening energy region to be explored while tending to concentrate the search around m_τ^0 at the beginning. Its disadvantage is that the function $g(m_\tau^*)$ is not really meaningful and hence its peak is somewhat artificial.

The alternative above has the advantages of simplicity both of use and understanding; its disadvantage is that it has hard cut-offs imposed by the energy restrictions.

Algorithm 3.

1. If a total of zero events have been observed in the search so far, define $E_{i+1} = E_i + \Delta_0$ where Δ_0 is a constant.
2. Otherwise if $|E_{\text{cand}} - E_i| > \Delta_{\text{max}}$ then $E_{i+1} = E_i + \text{sign}(E_{\text{cand}} - E_i)\ \Delta_{\text{max}}$.
3. Otherwise if $|E_{\text{cand}} - E_i| \geq s$ then $E_{i+1} = E_{\text{cand}}$.
4. Otherwise $E_{i+1} = E_i$.

Table 6.7 lists Δ^{final}, σ_A^+, and σ_A^- for a variety of limited energy step algorithms for comparison with Table 6.4 in Section 6.5. One may observe that for $\Delta_{\text{max}} = 100$ MeV the bias becomes large and negative for values of m_τ^0 above m_τ^{true}. This is to be expected because an energy step of 100 MeV is almost equivalent to an unlimited energy domain in the sense that almost all energy differences are smaller than 100 MeV anyway. I explored the results of an algorithm with unlimited energy domain in Section 6.6 and remarked there that a symptom was large, negative values for Δ^{final}.

However, for $\Delta_{\text{max}} = 10$ MeV, the values for the bias of the algorithm are comparable with those for the expanding Gaussian method in Table 6.4; the values for σ_A^+ and σ_A^- tend to be slightly higher. Both of these methods have the disadvantage that if the true tau mass is very far from the initial guess m_τ^0 then these algorithms will take longer to reach the m_τ^{true} energy region, but either of them can be made to avoid the disastrous effect of the first search point with suitable choices of $\{\Delta_{\text{max}}, \Delta_0\}$ or $\{\mu_{\text{exp}}, \alpha\}$. The expanding Gaussian algorithm was chosen for the real experiment as it yields slightly better results and was the method that had been most thoroughly

Monte Carlo Parameters				Final Accuracy	Widths	
m_τ^0 (MeV)	m_τ^{true} (MeV)	$\Delta_{\max}$ (MeV)	Δ_0 (MeV)	Δ^{final} (MeV)	σ_A^+ (MeV)	σ_A^- (MeV)
1756.9	1776.9	10.0	10.0	0.08 ± 2.43	0.91 ± 2.14	0.83 ± 0.86
1769.7	1776.9	10.0	10.0	0.17 ± 1.06	0.50 ± 0.76	0.67 ± 0.45
1776.9	1776.9	10.0	10.0	0.13 ± 0.71	0.52 ± 1.10	0.59 ± 0.26
1784.1	1776.9	10.0	10.0	0.14 ± 0.60	0.43 ± 1.02	0.64 ± 0.19
1796.9	1776.9	10.0	10.0	0.20 ± 0.80	0.47 ± 0.13	0.76 ± 0.28
1756.9	1776.9	100.0	10.0	0.07 ± 2.43	0.91 ± 2.14	0.82 ± 0.87
1769.7	1776.9	100.0	10.0	0.17 ± 1.06	0.51 ± 0.76	0.67 ± 0.45
1776.9	1776.9	100.0	10.0	0.08 ± 0.89	0.54 ± 1.12	0.60 ± 0.28
1784.1	1776.9	100.0	10.0	-0.78 ± 3.88	1.06 ± 2.01	0.99 ± 1.10
1796.9	1776.9	100.0	10.0	-0.50 ± 4.03	1.74 ± 2.67	1.52 ± 2.10

Table 6.7 Δ^{final}, σ_A^+, and σ_A^- for two limited energy step algorithms with five different values for m_τ^0.

studied at the time.

For both algorithms, with the exception of a few extreme cases, the algorithm is equivalent to Algorithm 1 after approximately 1000 nb^{-1}, *i.e.*, the limitations imposed generally have no effect after this point as the difference between E_{i+1} and E_i has become small naturally.

Chapter 7 Event Selection

Section 7.1 Overview

In order to calculate $P(n_i\,;\mu_i)$ in Equation (5.2) one needs to measure n_i, the number of $\tau^+\tau^-$ events detected at each search point. Unfortunately taus represent only about 0.006% of the events which trigger the detector at this energy. So one would like to retain as many of the tau events as possible while discarding any others. In order to maximize the signal-to-background ratio we consider only selected decay modes of the tau. These modes have certain characteristics which make them more easily distinguishable from background than others.

The most obvious characteristic of any tau decay is that it includes at least one neutrino which will leave no trace in the detector. Hence there will be missing energy and momentum. Secondly a large fraction (approximately 86%) of tau decays have only one charged particle in them. I shall restrict myself to those decays only; this implies a charged multiplicity for the event of two. Together these two considerations imply an acollinearity of the two charged tracks for the great majority of the detected $\tau^+\tau^-$ events.

For two-body decay modes the momentum of both daughter particles in the τ rest frame is a constant. In particular for the pion decay channel, $\tau \rightarrow \pi\nu_\tau$, the pion is monochromatic. Near threshold the τ is almost at rest in the laboratory frame. So the momentum distribution is smeared only slightly by boosting to that frame and is still characteristic of the decay.

In summary, a $\tau^+\tau^-$ event can be distinguished as a two-prong event with

acollinear tracks both of which emanate from the interaction point (IP). One of them will, for the case of pion decay, be approximately monochromatic.

Throughout this thesis these modes will be identified by listing the charged daughter particles without reference to whether that charge is positive or negative. For instance, both the decay mode $\tau^+ \rightarrow e^+\nu_e\bar{\nu}_\tau$, $\tau^- \rightarrow \mu^-\bar{\nu}_\mu\nu_\tau$ and its charge conjugate $\tau^- \rightarrow e^-\bar{\nu}_e\nu_\tau$, $\tau^+ \rightarrow \mu^+\nu_\mu\bar{\nu}_\tau$ will be referred to as the $e\mu$ mode.

A study of the background to these events follows, after which the implementation of the above characteristics to distinguish $\tau^+\tau^-$ events is explained in detail.

Section 7.2 Background Estimation

Background events are those events which could be mistaken as deriving from the decay one wishes to study. Backgrounds to a particular decay of the $\tau^+\tau^-$ pair fall into three groups:

1. Events in which tracks from one tau decay mode are misidentified as particles from a different tau decay mode.

2. Events in which tracks are *correctly* identified as the expected particles but which do not derive from tau decay. Direct quark production and two-photon processes contribute to this background. Also the ee decay channel will suffer backgrounds from radiative Bhabha events and the $\mu\mu$ channel from radiative di-muon decays.

3. Non-tau events in which the tracks are misidentified as the expected particles. The sources of these backgrounds are as for group 2 above.

Beam-gas and cosmic-ray events are not mentioned above as they are usually very easily distinguished from tau decays: the former by the fact that they generally

have only one track which does not necessarily come from the IP; the latter by the collinearity of the reconstructed tracks, from time-of-flight measurements, and again that they need not pass close to the IP.

Non-radiative Bhabha and di-muon events are also easily distinguished from true tau events. A discussion of their elimination will be included when I consider Group 2 below.

Group 1 will affect only the overall normalization of the number of events expected at any one search point. It will not affect the shape. Since, at the end of the search, we fit to the normalization via the κ^* parameter (see Section 8.2) this will not affect the measurement of the tau mass.

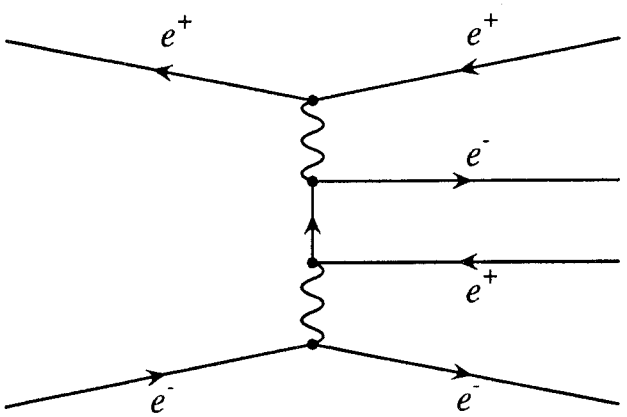

Figure 7.1 A two-photon event.

Group 2 represents a more serious problem. As mentioned above, the largest source of backgrounds of this type is two-photon processes. An example, which is a source of background to the ee mode, is shown in Figure 7.1. The problem is that the beam particles have $\cos\theta$ distributions strongly peaked towards ± 1. Hence the probability that two particles escape detection by passing along the beam pipe is

higher than one would wish. The remaining two particles can then masquerade as a tau decay.

A study of this type of event is undertaken on page 109 by selecting data which otherwise look like ee events but for which the two tracks have the same charge. Since in two-photon processes there will be an equal number of "same-sign" events as "opposite-sign" this provides a good opportunity to investigate this background.

Two quantities were found to distinguish background events from tau decays:

(i) acoplanarity, where $\theta_{\rm acop}$ is defined via

$$\cos(\theta_{\rm acop}) = -\frac{(\vec{p}_1 \times \hat{z}) \cdot (\vec{p}_2 \times \hat{z})}{|\vec{p}_1||\vec{p}_2|}, \tag{7.1}$$

where $\hat{z}$ is a unit vector along the direction of the e^- beam and $\vec{p}_i$ is the momentum of the $i^{\rm th}$ track, and

(ii) PTES, defined as

$$\text{PTES} = \frac{|\sum_i \vec{p}_i^{\,T}|}{E - \sum_i |\vec{p}_i|}\ , \tag{7.2}$$

where $\vec{p}_i^{\,T}$ is the transverse momentum of the $i^{\rm th}$ track and E is the centre of mass energy of the event.

These quantities are used in Sections 7.3 and 7.4 to reject background events. The distributions of these quantities for both tau events (from Monte Carlo) and background (from data) will be studied there.

Non-radiative Bhabha and di-muon events and can be distinguished from tau

decays by the collinearity of the two tracks. If we define $\theta_{\rm acol}$ via

$$\cos(\theta_{\rm acol}) = -\frac{\vec{p_1} \cdot \vec{p_2}}{|\vec{p_1}||\vec{p_2}|} \tag{7.3}$$

then, excluding resolution effects, both Bhabha and di-muon events have $\theta_{\rm acol} = 0°$ whereas tau events show no such concentration.

For radiative Bhabha and di-muon events, however, the two tracks will not be quite back-to-back due to the emitted photon. If the energy of the photon E_γ is large $\theta_{\rm acol}$ will be large, but, unless the photon escapes along the beam pipe, we are likely to detect the photon in the shower counter. Hence selection criteria which discriminate against events with $\theta_{\rm acol} \approx 0°$, against photons in the shower counter, and against missing momentum along the beam pipe will help reject radiative events.

Group 3 is found to contribute very little background. Studies of 5 million J/ψ decays show seven events which pass the relevant $e\mu$ selection criteria. This corresponds to 0.12 $e\mu$ events expected for the 5 pb^{-1} of the whole scan. During the search the program `runtau` was used to calculate the next running energy (see Section A.2). In this program the σ_B^* parameter was set to a fixed value independent of energy. The value used was 0.024 pb. After the search, however, the σ_B^* parameter is fitted as explained in Section 8.2 to take into account any differences between background at the J/ψ resonance and at tau threshold.

Section 7.3 During the Search

Only the $e\mu$ mode,

$$\tau^+ \rightarrow e^+\nu_e\bar{\nu}_\tau, \quad \tau^- \rightarrow \mu^-\bar{\nu}_\mu\nu_\tau \quad + \quad \text{charge conjugate}, \tag{7.4}$$

was used to detect $\tau^+\tau^-$ production during the search. This mode is referred to as

the "driving" mode throughout this thesis. This mode was the one used to originally discover the taus (see Chapter 2) and it still has one of the lowest background levels and one of the highest detection efficiencies (see Section 8.4). It is therefore ideal for detecting tau production. The selection criteria used during the search to detect this decay mode are outlined below.

1. Exactly two oppositely charged tracks having momentum between 350 MeV and the maximum for an electron from tau decay.*
2. Each track's point of closest approach to the interaction point of the detector satisfy the requirements $|x| < 1.5$ cm, $|y| < 1.5$ cm, and $|z| < 15$ cm.
3. $2.5° < \theta_{\rm acol} < 177.5°$.
4. $\theta_{\rm acop} > 10°$.
5. $\theta_{\rm acol} + \theta_{\rm acop} > 50°$.
6. No isolated photons, where a photon is is defined as isolated if it has a measured energy > 60 MeV and the angle to the nearest charged track is $> 12°$.
7. One of the tracks is well identified as a muon, the other well identified as an electron. For muon identification the criteria were:
   (*i*) Require, associated with the track, at least one muon layer with at least two tubes hit. (This automatically implies $|\cos\theta| < 0.68$.)
   (*ii*) $E_{\rm sc} < 0.5$ GeV where $E_{\rm sc}$ is the energy in the shower counter associated with the track.

$\star$ The value assumed for m_τ was 1770 MeV. Also the maximum allows for drift chamber resolution by extending 3σ in that quantity.

For electron identification the criteria were:

(*i*) $|\cos\theta| < 0.80$ and that the energy associated with the track, if any, is in the barrel shower counter rather than the endcap.

(*ii*) No muon counter hits associated with the track.

(*iii*) $0.8 < \beta < 1.5$, where β is measured by the TOF system.

(*iv*) For $p > 0.7$ GeV, we require $E_{sc} > 0.6$ GeV.

(*v*) For $0.6 < p \leq 0.7$ GeV, we require $E_{sc} > 0.55$ GeV and XSE > 0 or XSPI $> 3|$XSE$|$.†

(*vi*) For $0.35 < p \leq 0.6$ GeV, we require XSE > 0 or XSPI $> 3|$XSE$|$ and the lower bound on β is increased to 0.9.

Figure 7.2 shows the momentum distribution for all tracks from a Monte Carlo[77] generating $e\mu$ events at a centre of mass energy of 3.554 GeV. Only those events which are reconstructed as having two charged tracks are included. Figure 7.3 shows the corresponding plot for all data from a typical run at 3.5529 GeV. The shaded regions show the excluded tracks. One may easily observe that the percentage of tracks discarded from the typical run is much higher than that from the Monte Carlo. The signal-to-background ratio is thus increased.

Figures 7.4–7.6 show the x-, y-, and z-distributions of the point of closest approach to the IP for all tracks from a typical run. For the z-distribution, one may observe that it is strongly peaked towards zero, that there is a plateau region in which the distribution slowly diminishes until about ± 30 cm where the number of tracks drops

† XSE and XSPI are, respectively, the number of sigma from the electron and pion hypotheses reported by the dE/dx sub-system.

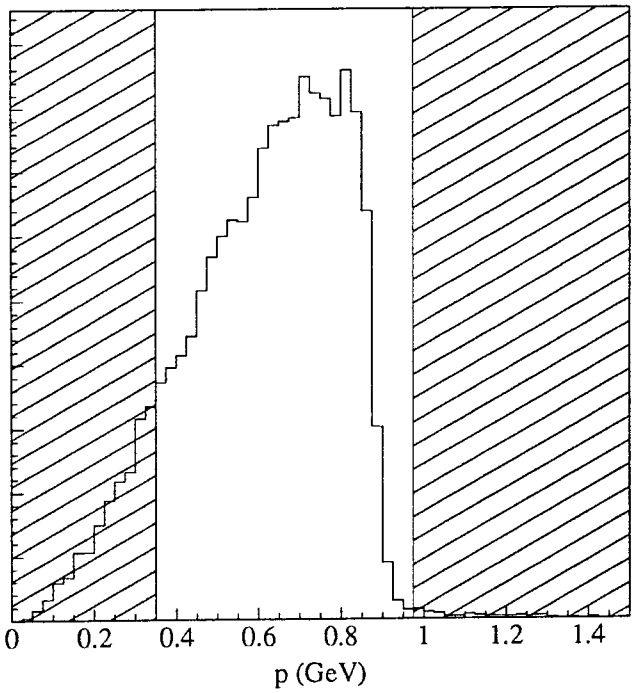

Figure 7.2 The momentum distribution for all 2-prong events from Monte Carlo data at a centre of mass energy of 3.554 GeV.

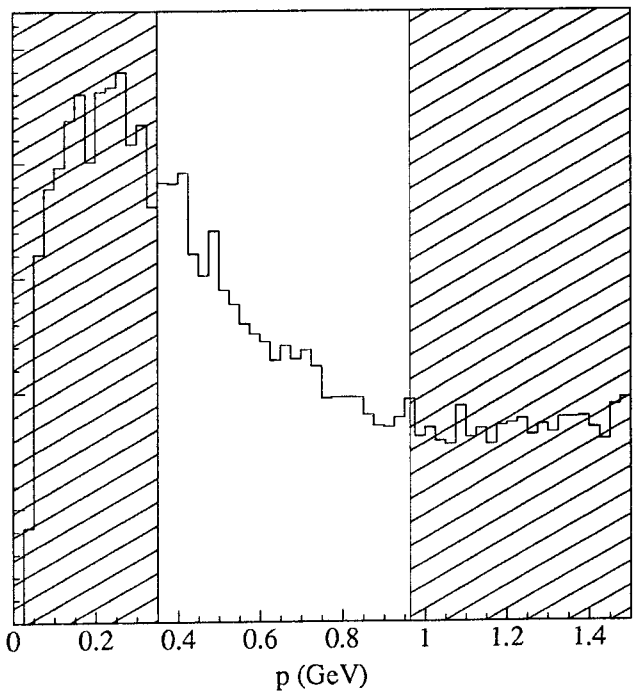

Figure 7.3 The momentum distribution for all 2-prong events from a typical run.

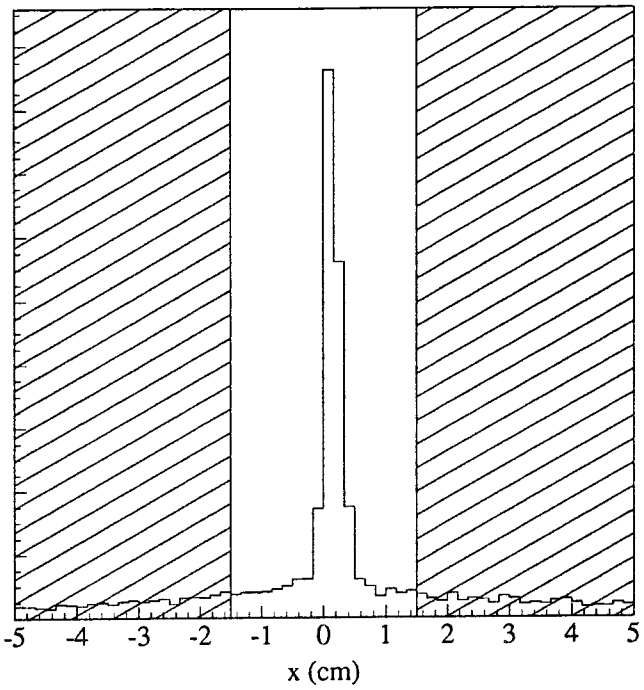

Figure 7.4 x coordinate at point of closest approach to the IP for a typical run.

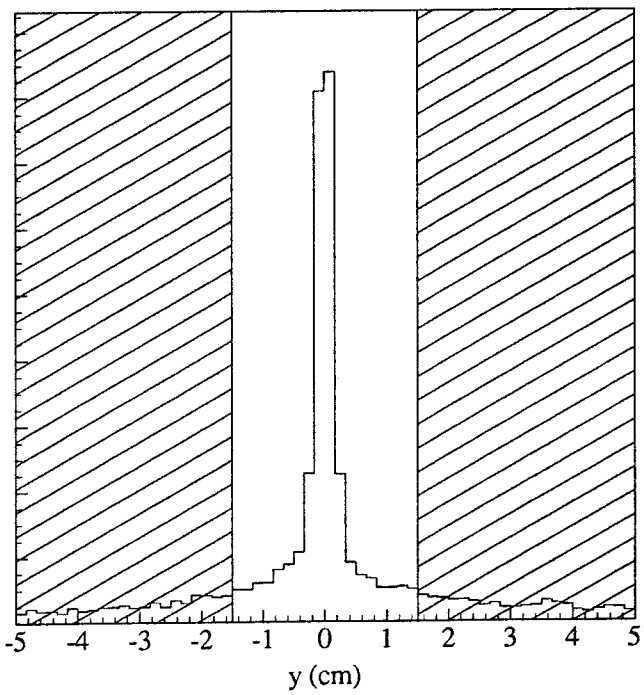

Figure 7.5 y coordinate at point of closest approach to the IP for a typical run.

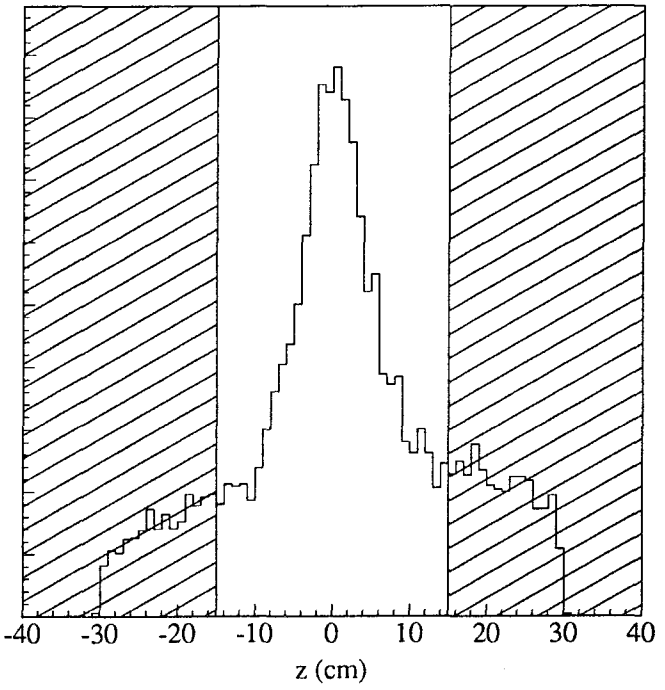

Figure 7.6 z coordinate at point of closest approach to the IP for a typical run.

sharply to zero. The cut-off at ± 30 cm is caused by track reconstruction software and trigger selection criteria. The central peak is caused by physics events due to e^+e^- collisions. The plateau background is due to cosmic-ray and beam-gas events. Similar central peaks are observed in the x- and y-distributions. The shaded areas are once again the excluded regions and we can see that the selection criteria based on x, y, and z clearly keep all events due to collisions while discarding most of the remaining events. Note that the IP was slightly offset from zero in the x direction during the run. This does not affect our identification as the selection criterion on x are set sufficiently wide.

Figure 7.7 and 7.8 show scatter plots of θ_{acol} versus θ_{acop} for the same Monte Carlo events and for a few typical runs respectively. One may observe the striking

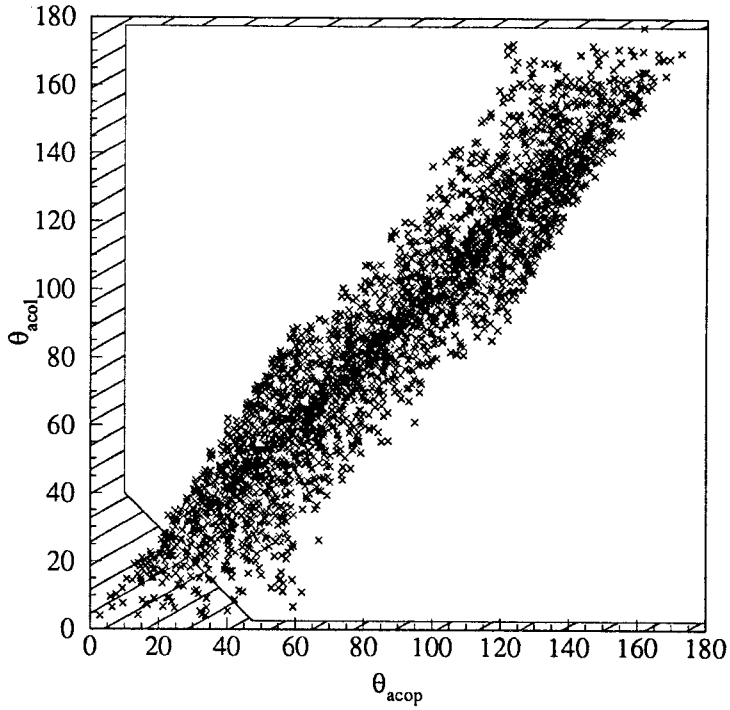

Figure 7.7 A scatter plot of acollinearity versus acoplanarity for Monte Carlo $e\mu$ events at $E = 3.554$ GeV.

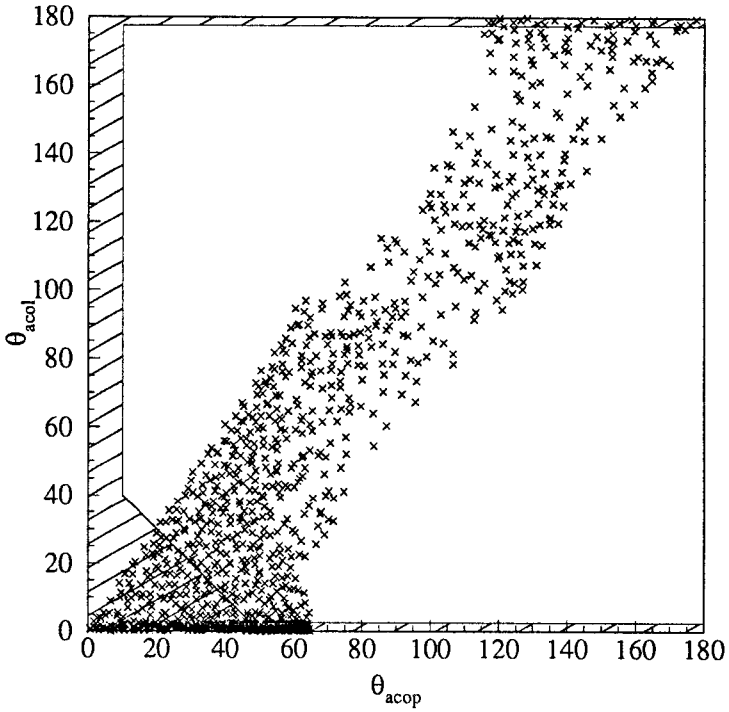

Figure 7.8 A scatter plot of acollinearity versus acoplanarity for data at $E = 3.55290$ GeV.

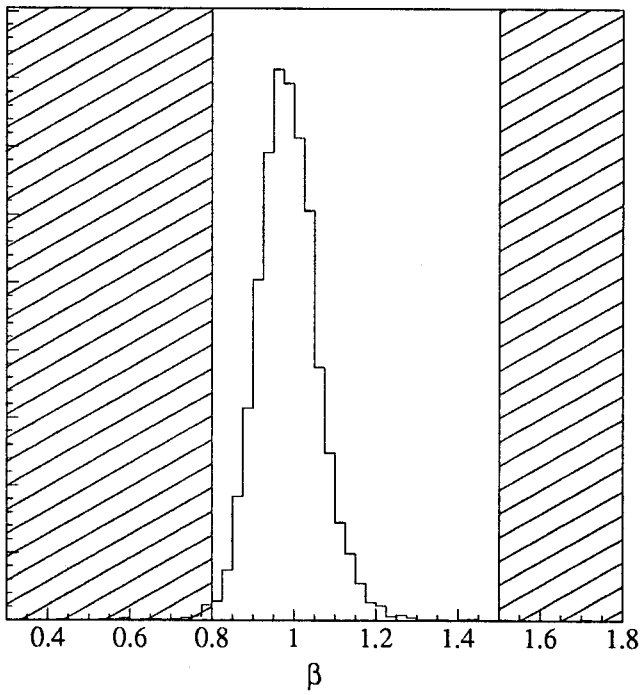

Figure 7.9 β distribution for all electron tracks from $e\mu$ Monte Carlo events.

difference in the distribution of events: the Monte Carlo events are concentrated in a line from the bottom left hand corner to the top right whereas the majority of events for the data are concentrated in the bottom left hand corner. The selection criteria capitalize on these differences to reject background events.

Figure 7.9 shows the distribution of β for all electron tracks from $e\mu$ Monte Carlo data at a centre of mass energy of 3.554 GeV. Only those tracks which pass all event selection criteria plus the first two electron identification criteria are included. β is calculated from the time at which the charged track crosses the TOF system, the path length to that point and the momentum of the track as reported by the drift chamber. Theoretically, of course, the maximum value for β is one. Due to measurement resolutions in both the drift chamber and the TOF system, however,

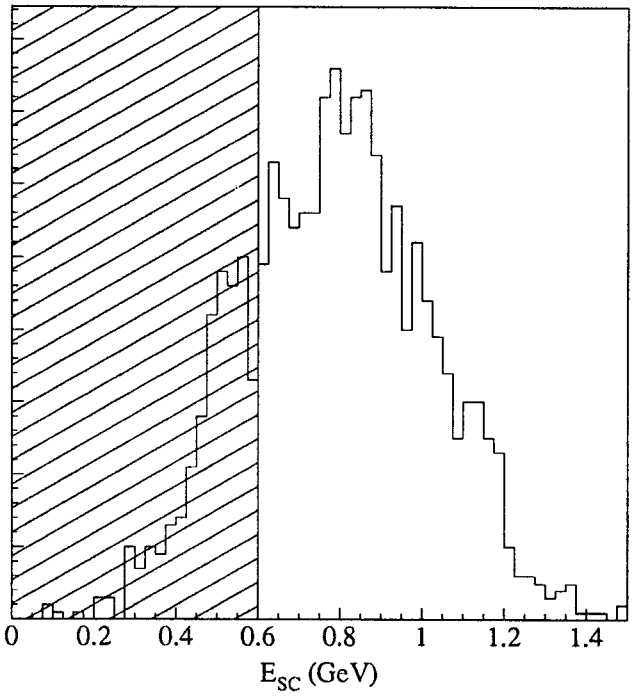

Figure 7.10 The energy distribution for electron tracks from $e\mu$ Monte Carlo events for $p > 0.7$ GeV.

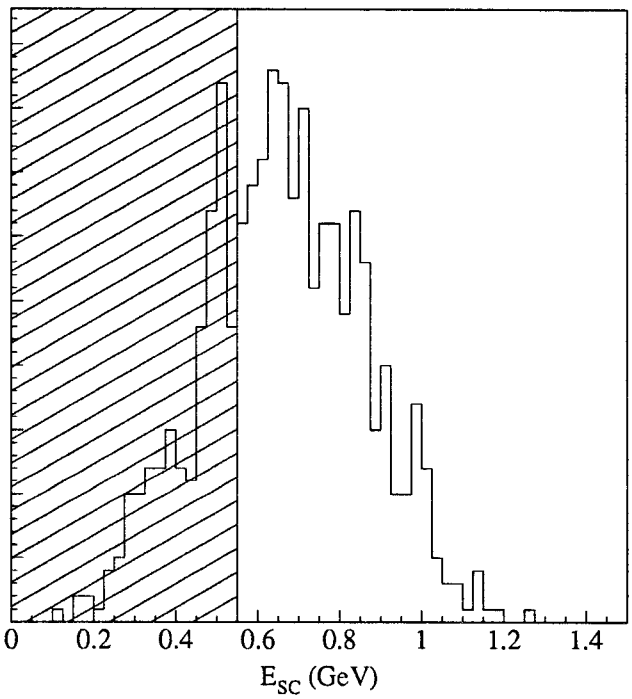

Figure 7.11 The energy distribution for electron tracks from $e\mu$ Monte Carlo events for $0.6 < p \leq 0.7$ GeV and XSE > 0 or XSPI $> 3|$XSE$|$.

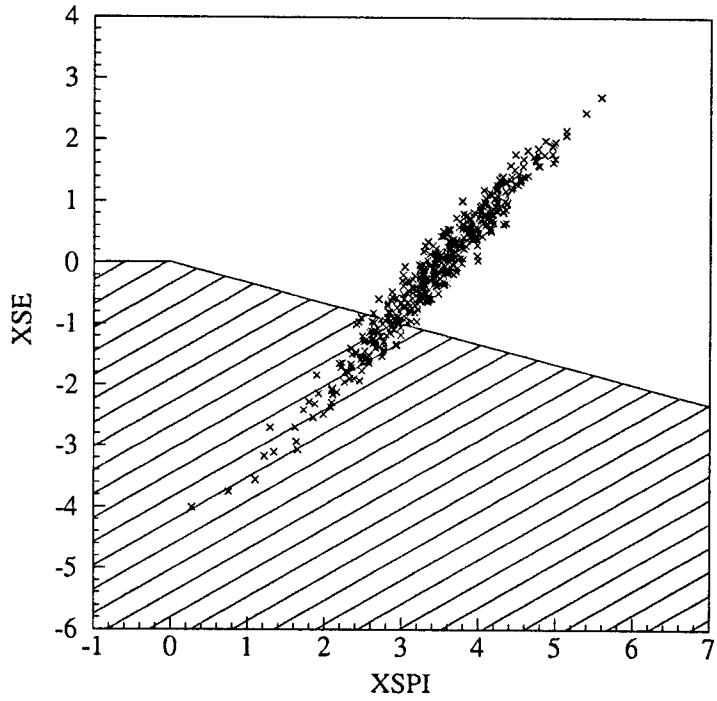

Figure 7.12 A scatter plot of XSE *vs.* XSPI for $0.6 < p \leq 0.7$ GeV and $E_{sc} > 0.55$ GeV for electron tracks from $e\mu$ Monte Carlo events.

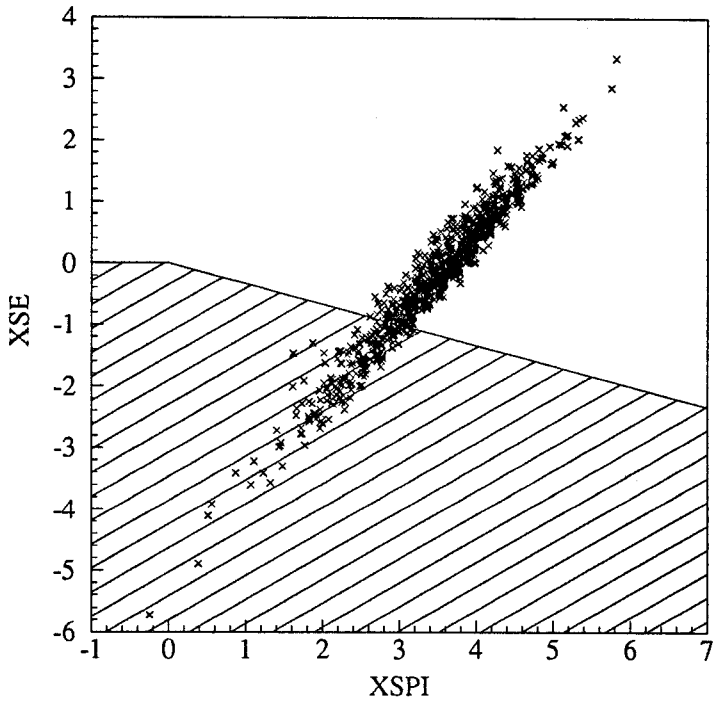

Figure 7.13 A scatter plot of XSE *vs.* XSPI for $0.35 < p \leq 0.6$ GeV for electron tracks from $e\mu$ Monte Carlo events.

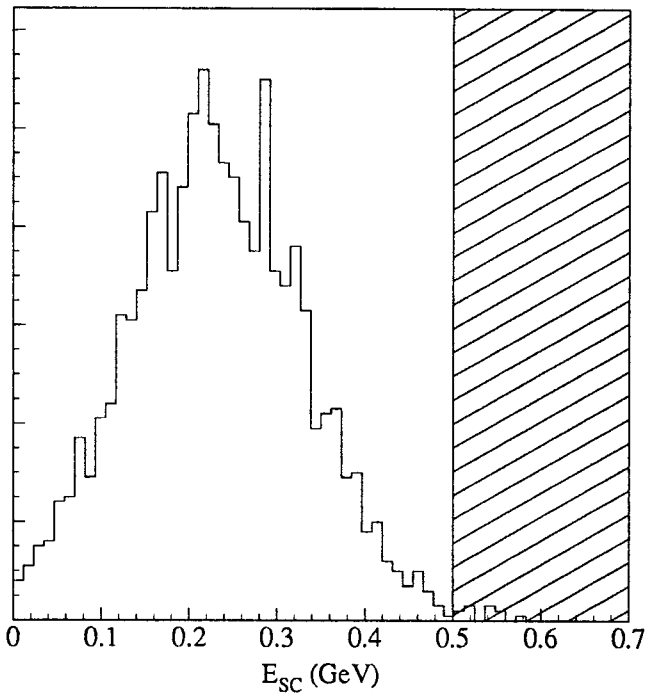

Figure 7.14 The energy distribution for muon tracks from $e\mu$ Monte Carlo events.

the value reported can easily exceed this. The shaded areas on the figure show the region excluded by electron identification criterion (*iii*). One may observe that the vast majority of electron tracks pass this criterion.

Figures 7.10–7.14 show distributions for electron and muon tracks from the same Monte Carlo data (only those tracks from events which pass the event criteria 1–6 listed previously are shown). Figure 7.10 shows the energy distribution for tracks which pass the electron identification criteria (*i*)–(*iii*) and is plotted for tracks with $p > 0.7$ GeV only. Similarly Figure 7.11 shows the energy distribution for tracks which satisfy $0.6 < p \leq 0.7$ GeV and the dE/dx criteria XSE > 0 or XSPI $> 3|$XSE$|$. The shaded areas on the figures show the tracks discarded by the selection criteria.

Figures 7.12 and 7.13 show scatter plots for XSE versus XSPI for electron tracks

which satify the electron identification criteria (i)-(iii) and all criteria except the dE/dx requirements for, respectively, the momentum ranges $0.6 < p \leq 0.7$ and $0.35 < p \leq 0.6$.* Again the shaded areas represent the regions which are discarded. We can see that the criteria are efficient for real electron tracks.

Figure 7.14 depicts the energy distribution for Monte Carlo muons which cause a double-hit in one of the muon tubes. Once again the efficiency of the selection criterion is demonstrated.

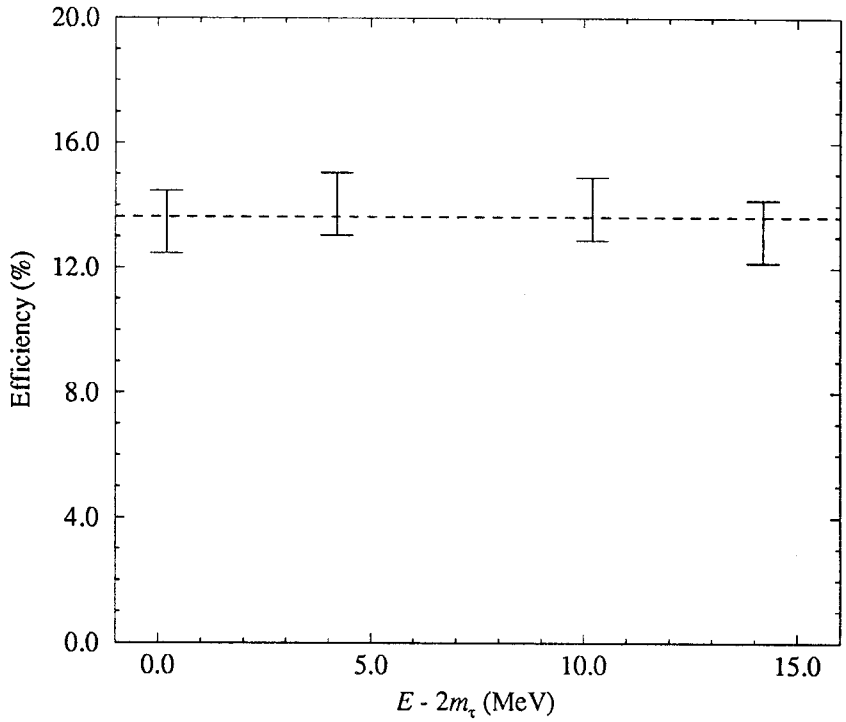

Figure 7.15 The efficiency of the selection criteria as a function of $E - 2m_\tau$ for $m_\tau = 1776.9$ MeV.

Figure 7.15 shows the value of the event identification efficiency ϵ as a function of $E - 2m_\tau$ throughout the range covered by the search. ϵ is estimated from the

* Note that the lower bound on β is also increased to 0.9 for the lower momentum range to prevent kaon misidentification.

number of events identified from a Monte Carlo model of tau decays via the $e\mu$ mode. The data fit well the hypothesis that the efficiency is independent of centre of mass energy. A fit yields $\epsilon = 13.64 \pm 0.50\%$ as depicted by the dashed line in the figure.

Section 7.4 After the Search

After the search all the data was re-analysed. In addition the measurement was expanded to include the following decay modes:

$$\tau^+\tau^- \rightarrow e\pi,\ \mu\pi,\ ee,\ \mu\mu,\ \pi\pi \text{ plus undetected neutrinos.} \tag{7.5}$$

These modes give independent estimates of the mass for cross checking purposes and are combined in the final result to produce an overall estimate with lower uncertainties.

A new analysis for all modes was developed using the data accumulated to re-calibrate and to investigate identification criteria. The re-analysis involved the development of a confidence-level based identification. For each track and each identification hypothesis, each of the three sub-systems—TOF, SC, and dE/dx—returned (i) a number of degrees of freedom 0 or 1 (0 implies that this sub-system does not have enough information to return a χ^2), and (ii) a χ^2 that the track satisfies the hypothesis. A confidence level is then constructed from the χ^2's and the number of degrees of freedom.

The drift chamber is used to measure the momentum on which selection criteria were based, and to estimate the point of closest approach to the interaction point. The muon system is only used to identify muons, *i.e.*, it acts as a veto over the other systems.

The following sub-sections catalogue each sub-system and itemize their contributions to the particle identification scheme.

Drift Chamber

Information from the drift chamber is used to check that the quality of the fitted track is good and to require limits on the momentum p of each track. The minimum and maximum momentum depend on the identification hypothesis and the centre of mass energy E. They are calculated via the minimum and maximum theoretical value for the momentum for each tau decay minus or plus $3\sigma_p$ where σ_p is the momentum resolution in the main drift chamber.[⋆] The theoretical momenta are calculated using a tau mass of 1775.9 MeV, where we subtract 1 MeV from our previous best estimate of the tau mass in order to maintain the detection efficiency uniform across the centre of mass energy range used in the experiment.

Table 7.1 shows the minimum and maximum momenta for four identification hypotheses assuming a centre of mass energy of 3.56838 GeV; the proton hypothesis is ignored at this stage. 3.56838 GeV is the highest centre of mass energy during the search (see Section 8.1), hence the momentum intervals are at their widest. Figure 7.16 shows the values of $p_{\rm min}$ and $p_{\rm max}$ for the pion hypothesis as a function of centre of mass energy for $m_\tau = 1.7759$ GeV.

The drift chamber also provides information about the point of closest approach to the IP (x, y, z) for each track.

Time-of-Flight

The TOF system checks that the appropriate quality flag for the track is set and

⋆ If the minimum momentum is less than zero, zero is assumed.

Identification Hypothesis	$p_{\min}$ (GeV)	$p_{\max}$ (GeV)
e	0	1.064
μ	0	1.061
π	0.736	1.059
K	0.674	0.994

Table 7.1 Limits on momentum for the four particle identification hypotheses for $E = 3.56838$ GeV.

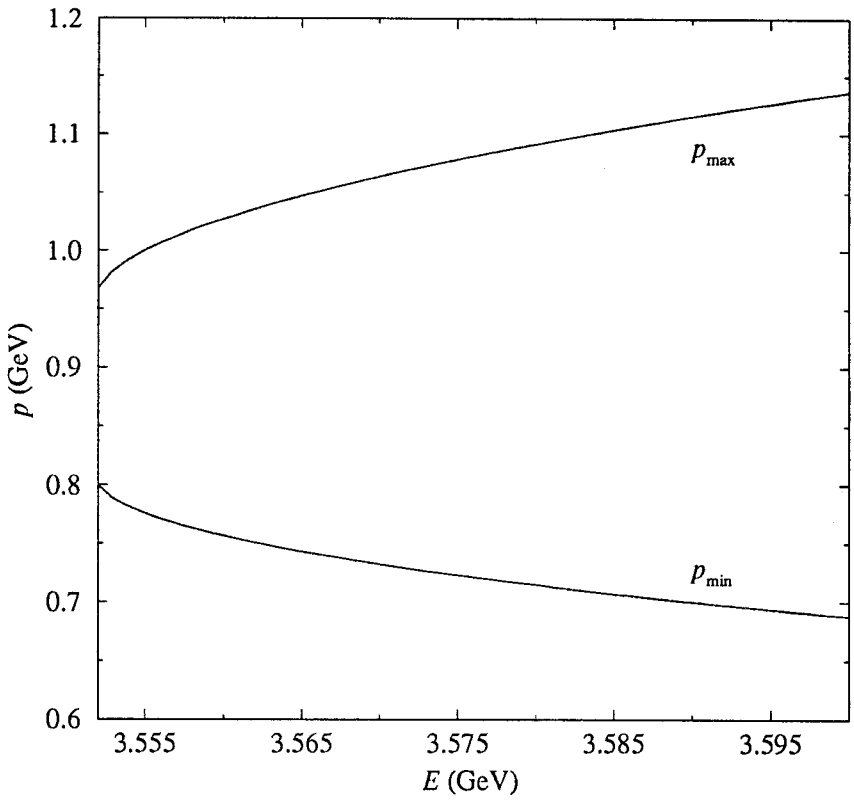

Figure 7.16 $p_{\min}$ and $p_{\max}$ for the pion identification hypothesis as a function of centre of mass energy.

returns a χ^2 based on the expected time t_0 and the expected width σ_t for each hypothesis

$$\chi^2_{\rm TOF} = \left(\frac{t - t_0(J,p)}{\sigma_t(J)}\right)^2. \tag{7.6}$$

t_0 is defined as $l/\beta c$, where l is the path length and $\beta = p/\sqrt{p^2 + m_J^2}$. σ_t has been fitted to the data accumulated during the tau run and is 400 ps for the electron hypothesis, 450 ps otherwise. J refers to the particle identification hypothesis.

Shower Counter

The shower counter code returns a χ^2 based on the variable λ where

$$\lambda = \begin{cases} E_{\rm sc}/p, & \text{for the electron hypothesis,} \\ E_{\rm sc}\sin\theta/p, & \text{otherwise.} \end{cases} \tag{7.7}$$

Here $E_{\rm sc}$ is the energy deposited in the shower counter associated with the charged track under consideration and p is the momentum from the drift chamber as before.

Electrons are the only charged particles that shower in the shower counter. Hence this variable only distinguishes electrons from other particles; the χ^2 returned for all non-electron hypotheses is identical.

The definition of $\chi^2_{\rm SC}$ is

$$\chi^2_{\rm SC} = \left(\frac{\lambda - \lambda_0(J)}{\sigma_\lambda(E_{\rm sc}, p, J)}\right)^2 \tag{7.8}$$

where

$$\lambda_0 = \begin{cases} 1.0, & \text{for electrons,} \\ 0.21, & \text{otherwise.} \end{cases} \tag{7.9}$$

σ_λ is given by

$$\sigma_\lambda = \left[\left(\frac{\sigma_{E_{\rm sc}}}{p}\right)^2 + \left(\frac{E_{\rm sc}\sigma_p}{p^2}\right)^2\right]^{\frac{1}{2}}. \tag{7.10}$$

For electrons $\sigma_{E_{sc}} = 0.25\sqrt{p}$ GeV whereas for all other hypotheses $\sigma_{E_{sc}} = 0.09$ GeV. σ_p/p is $0.021\sqrt{1+p^2}$ as mentioned on page 20. The coefficients 1.0 and 0.21 for λ_0 and 0.25 and 0.09 for $\sigma_{E_{sc}}$ are fitted to data.

dE/dx System

The dE/dx system returns a χ^2 based on the most probable pulse height ξ. ξ is calculated via a truncated mean of the pulse heights measured on the wires in the main drift chamber.

$$\chi^2_{dE/dx} = \left(\frac{\xi - \xi_0(J,p)}{\sigma_\xi(J)}\right)^2 \tag{7.11}$$

where $\sigma_\xi(J)$ is defined as

$$\sigma_\xi(J) = \alpha(J)\,\xi_0 \left(\frac{35}{N_{\text{hits}}}\right)^{0.423}. \tag{7.12}$$

N_{hits} is the number of dE/dx samples, α is 0.10 for the e and μ identification hypotheses, 0.12 for all others. Both the coefficients in the equation describing σ_ξ and the expected truncated mean pulse height ξ_0 were fitted to data.

Muon Chamber

If there are hits in the muon chamber associated with a track and at least one of those hits is in the first layer then the normalized hit radius r_μ is constructed as follows:

$$r^2_\mu = \frac{1}{N_\mu}\sum\left((x_{\text{hit}} - x_{\text{proj}})^2 + (y_{\text{hit}} - y_{\text{proj}})^2\right) \tag{7.13}$$

where the sum is over the layers which have hits and N_μ is the number of such layers. x_{hit} is the x coordinate of the hit, x_{proj} is the x coordinate predicted for the track projected from the drift chamber and similarly for y_{hit} and y_{proj}.

This quantity is not formulated in terms of a χ^2, but is used as a veto to distinguish muons from other identification hypotheses.

Track Identification

Given these χ^2's one can calculate a total χ^2 for the event via:

$$\chi^2(J) = \sum_s \chi^2_s(J) \tag{7.14}$$

where the sum is over the n sub-systems which return one for their number of degrees of freedom. A confidence level C for each identification hypothesis can then be constructed via the normal method:

$$C(J) = \int_{\chi^2(J)}^{\infty} \frac{1}{2^{n/2}\Gamma(n/2)} z^{n/2-1} e^{-z/2} dz. \tag{7.15}$$

Thence a track can fall into one of three categories:

(a) The track is identified as a muon if $p > 500$ MeV, $C(\mu) > 0.05$ and $r_\mu < 0.5$ m.

(b) The track is identified as particle hypothesis J when $C(J) > 0.05$ and $C(J) > C(K)$ for all $K \neq J$ where $J, K \in \{e, \pi, K, p\}$ and the track has not been identified as a muon and $p_{\min} < p < p_{\max}$ where $p_{\min}$ and $p_{\max}$ were defined on page 97.

(c) Otherwise the track is unidentified.

Selection Criteria

Given these identifications of all the tracks in an event we require the following selection criteria to identify any tau event.

1. Exactly two oppositely charged tracks.

2. The transverse momentum for each track must be at least 100 MeV. This prevents us from considering tracks which never reach the TOF or SC systems due to the magnetic field.

3. $|z| < 15$ cm and $r < 1$ cm for both tracks, where $r = \sqrt{x^2 + y^2}$. We also require $|z_1 - z_2| < 5$ cm.

4. $|\cos\theta| \leq 0.75$ for both tracks.

5. We require no isolated photons as before (see page 85).

6. Both tracks must be positively identified via the track identification criteria above. For instance in the case of the $\mu\pi$ decay mode we require that one of the two tracks be identified as a muon the other as a pion. Other decay modes are defined in a similar fashion.

7. Events must pass a scan by eye which checks for any extra unreconstructed charged tracks or photons.

8. For each mode we require PTES $>$ PTES_{min} where the PTES minima are shown in Table 7.2 below.

Event Type	PTES_{min}
$e\mu$	0.2
ee	0.4
$e\pi$	0.2
$\mu\pi$	0.2
$\mu\mu$	0.2
$\pi\pi$	0.2

Table 7.2 PTES limits for event identification criteria.

The above criteria were selected in order to provide a well identified sample of $\tau^+\tau^-$ events. The remainder of this section shows how the criteria were selected.

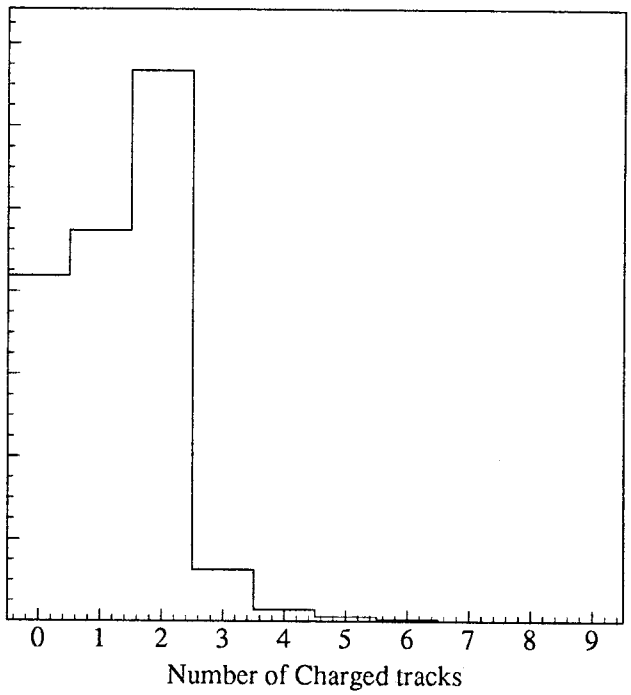

Figure 7.17 Distribution of the number of charged tracks for all events from a typical run.

Figure 7.17 shows the distribution of the number of charged tracks for a typical run. By restricting ourselves to only those events with two charged tracks we select 41% of the total number of events. However, after making allowance for track detection inefficiency, about 72% of $\tau^+\tau^-$ events have two charged tracks. So this criterion increases the signal-to-background ratio.

The z-distribution for a typical run from our data was shown in Figure 7.6. Figure 7.18 shows the r distribution for all tracks from the same run. In this case the distribution is strongly peaked at zero with a small tail out to almost 15 cm. The shaded area in the figure shows the excluded region.

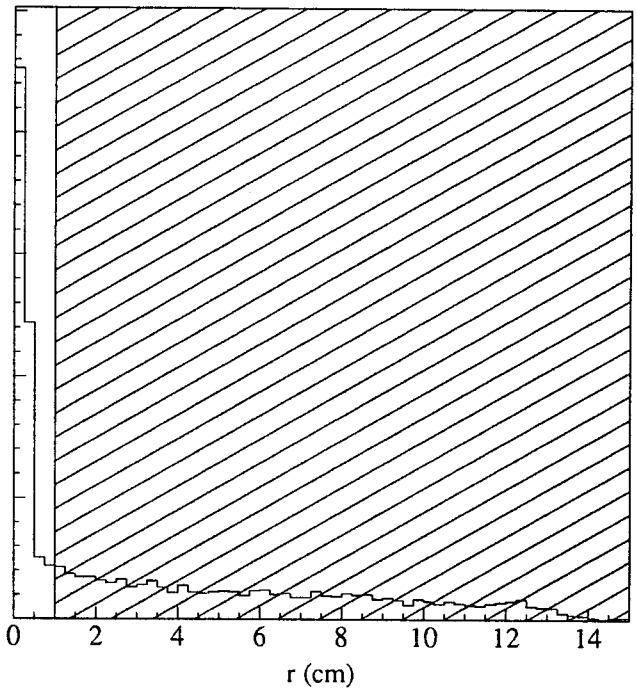

Figure 7.18 r distribution for all tracks from a typical run.

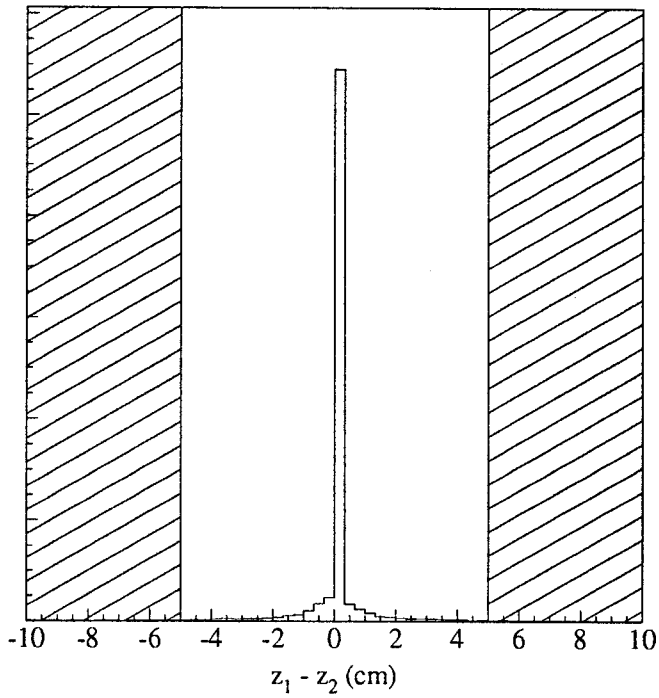

Figure 7.19 Distribution of $z_1 - z_2$ for all events with two charged tracks from a typical run.

Figure 7.19 shows the distribution of $z_1 - z_2$. Once again the distribution is very strongly peaked towards zero with only small tails extending outwards. The three selection criteria based on z, r, and $|z_1 - z_2|$ have the effect of including all $\tau^+\tau^-$ events but excluding most of the cosmic-ray and beam-gas backgrounds whose tracks are not concentrated around the IP as mentioned in Section 7.3.

The $\cos\theta$ selection criteria prevent us from considering any charged tracks which pass only partially or not at all through the barrel shower counter. During our data-taking the endcap shower counter was not fully calibrated and hence was only used to spot neutral tracks during the hand scan.

Figure 7.20 shows a scatter plot of the energy deposited in the shower counter E_γ and the minimum angle to the nearest charged track $\theta_{\rm min}$ for all reconstructed neutral tracks from 10,000 Monte Carlo decays $\tau^+\tau^- \rightarrow e\mu +$ neutrinos. Only those events which pass selection criteria 1–4 are included. Figure 7.21 shows the same information for the same number of events for data taken at the J/ψ energy (well below tau threshold).

The minimum angle for each charged track is calculated separately based on the momentum of the charged track at the distance of closest approach to the IP, and based on the momentum of the track at its entrance to the shower counter. The minimum of this quantity over both charged tracks and over both methods of calculation becomes $\theta_{\rm min}$. In addition we ignore all showers which start after layer 12 of the shower counter.* Such showers are usually due to electronic noise or to high energy secondary particles produced by the shower but not contained within it.

The excluded region is shaded in both figures. We see that the majority of the

$\star$ This is half way through the shower counter and corresponds to 6 radiation lengths.

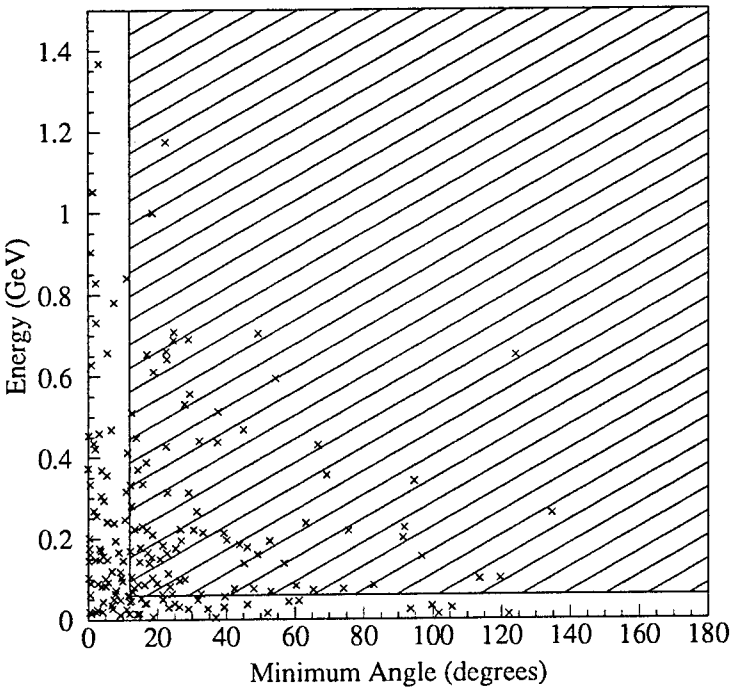

Figure 7.20 E_γ versus $\theta_{\min}$ from a Monte Carlo model of the decay $\tau^+\tau^- \rightarrow e\mu +$ neutrinos.

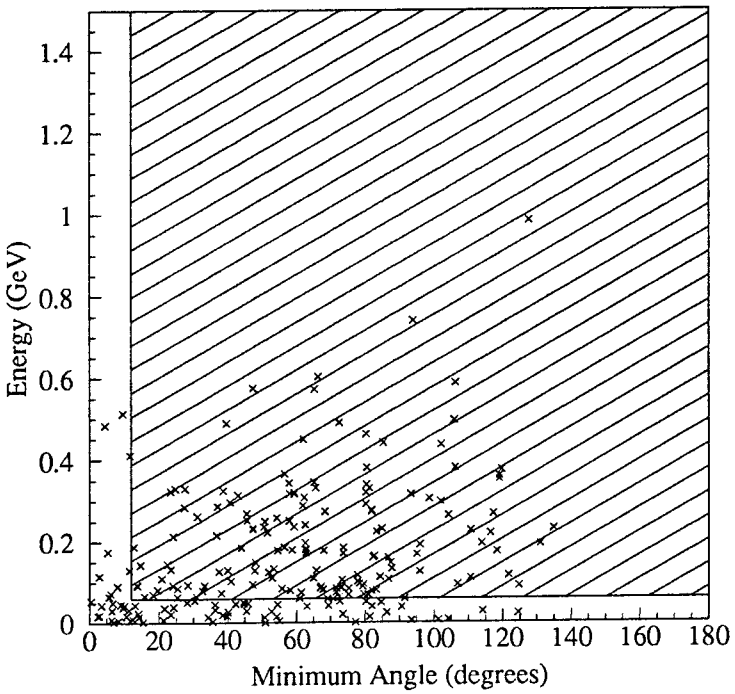

Figure 7.21 E_γ versus $\theta_{\min}$ from data taken at the J/ψ energy.

neutral tracks in Figure 7.20 (due to final or initial state radiation or to electronic noise in the calorimeter) are concentrated in the regions $E_\gamma \leq 60$ MeV and $\theta_{\rm min} \leq 12°$ and so have no effect on the event reconstruction. In the J/ψ data, however, the distribution is more evenly spread and a much greater proportion of events will fail this criterion. Hence the signal-to-background ratio is increased.

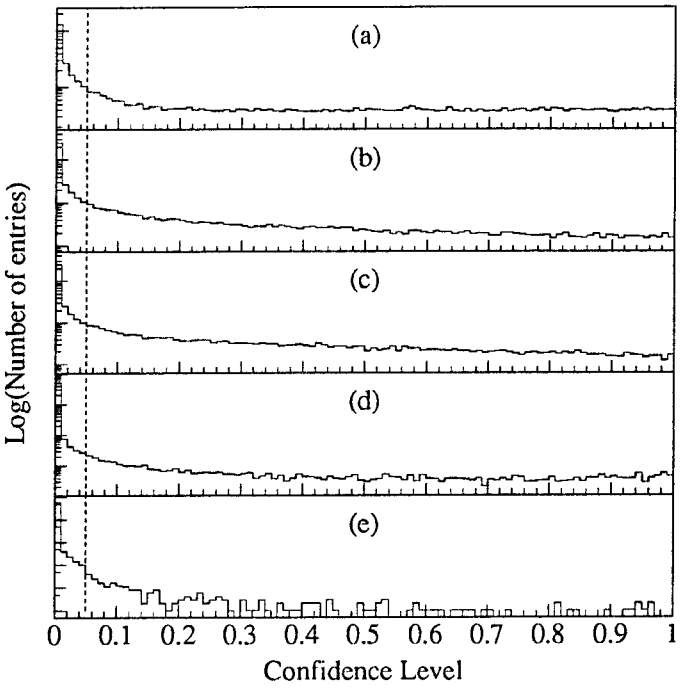

Figure 7.22 A comparison of the confidence level distributions for (a) electrons, (b) muons, (c) pions, (d) kaons, and (e) protons for all events after the isolated photon selection criterion.

Figure 7.22 shows a comparison between the confidence level distributions for all five different kinds of charged track identification hypotheses, where the distributions include all tracks from our data which pass the selection criteria up to and including the isolated photon criterion. Note that the scale for the number of entries axis is logarithmic.

The confidence levels are as one would expect with a large peak at zero plus an almost flat distribution out to one for well identified tracks. The selection criterion of $C(J) > 0.05$ for each hypothesis is indicated by the dashed line. One may observe that the value 0.05 successfully excludes the badly identified tracks while keeping the great majority of well identified tracks.

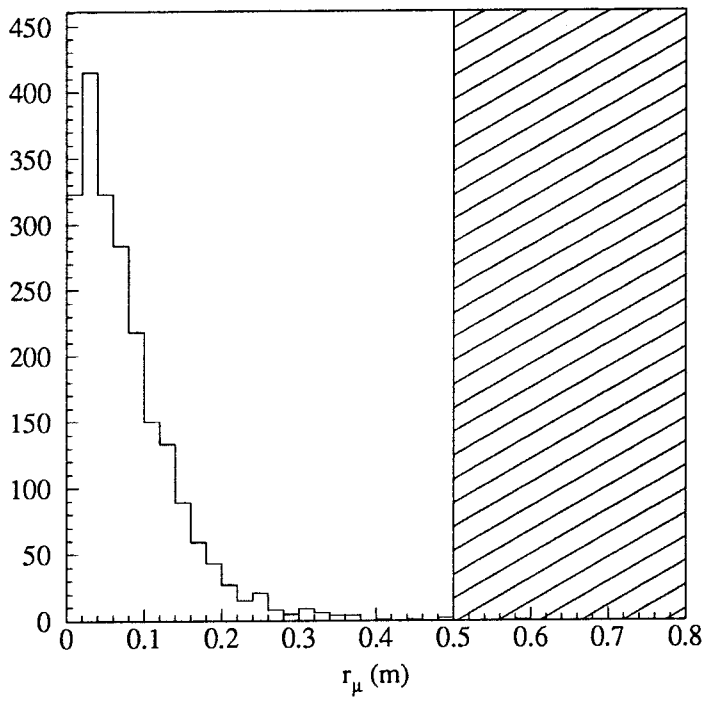

Figure 7.23 Showing the distribution of r_μ for muons from a Monte Carlo model of the $e\mu$ decay mode.

Figure 7.23 shows the distribution of r_μ for the muon tracks from Monte Carlo data. The centre of mass energy was 3.554 GeV. The shaded area shows the region excluded by the definition of a muon for track identification purposes (see page 101). However, only about 25% of real muon tracks have a value for r_μ calculated at all due to the momentum lower bound, of 500 MeV, for muons to reach the muon cham-

bers plus inefficiencies of reconstruction in both the drift and muon chambers. For comparison, the efficiencies with which Monte Carlo electrons and pions pass their respective identification criteria are approximately 50% and 35%.

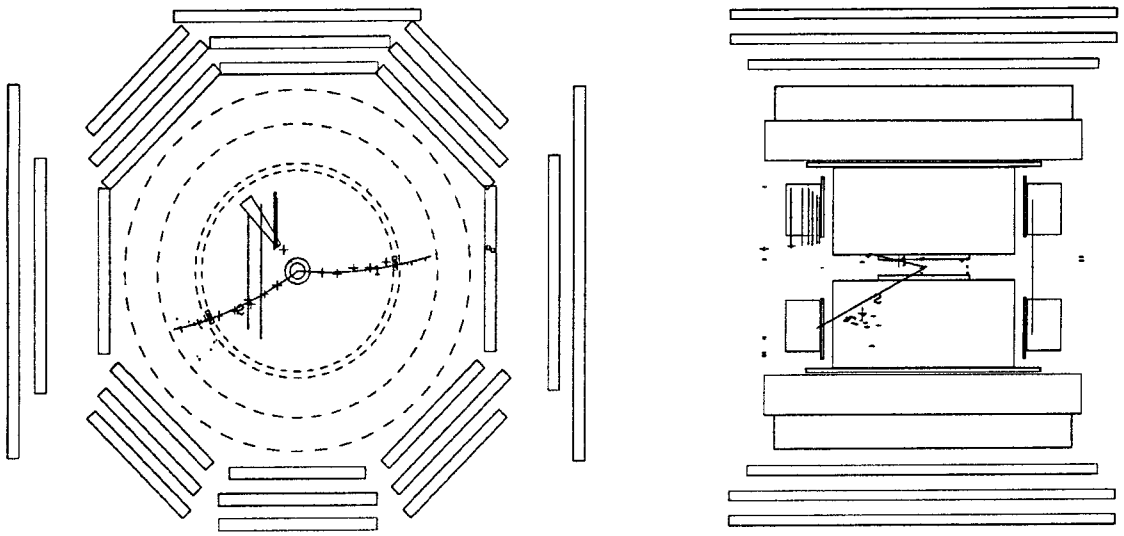

Figure 7.24 Showing an event which failed the hand scan due to a third unreconstructed charged track.

At the end of the selection the remaining events are scanned by eye for evidence which might suggest that the reconstruction was incorrect. A typical problem found at this stage was an extra charged or neutral track which had few hits on it (and hence had not been reconstructed) but which was confirmed by TOF and/or shower counter hits. Figure 7.24 shows an example of an event which failed the hand scan. One can clearly see a third charged track which was not found by the reconstruction software but which is supported by endcap TOF and SC hits.

Figure 7.25 shows the distribution of PTES for ee events where I have required that the sum of the charges of the two tracks ($Q_1 + Q_2$) not equal zero, but which would otherwise pass all criteria up to and including selection criterion 6. This type

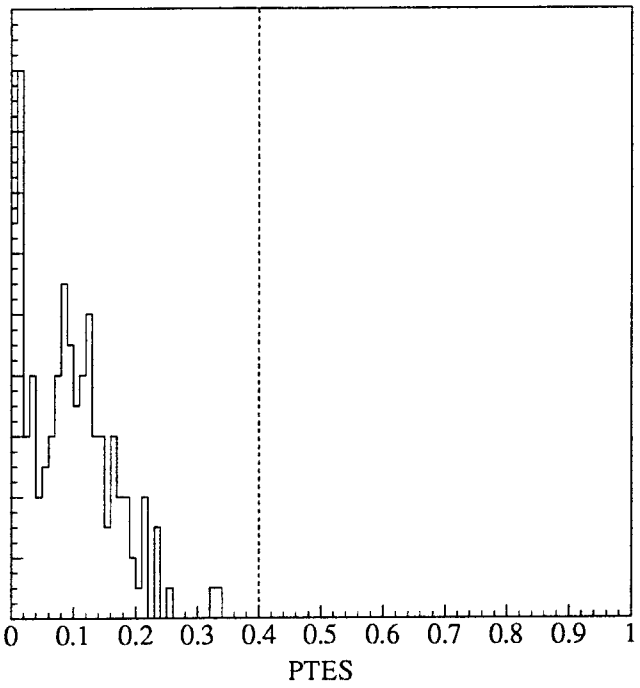

Figure 7.25 The PTES distribution for ee events with $Q_1 + Q_2 \neq 0$.

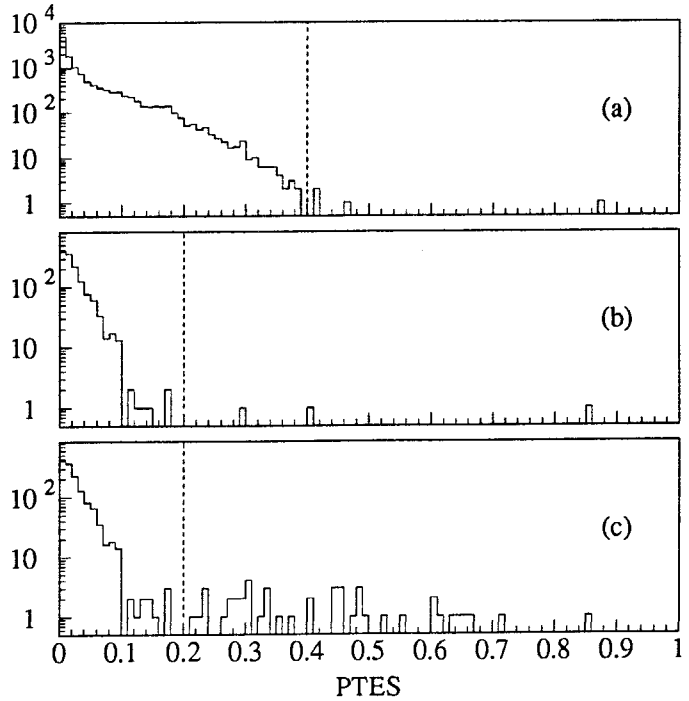

Figure 7.26 The PTES distribution for $Q_1 + Q_2 = 0$ for (a) ee events, (b) $\mu\mu$ events, (c) all other identified events.

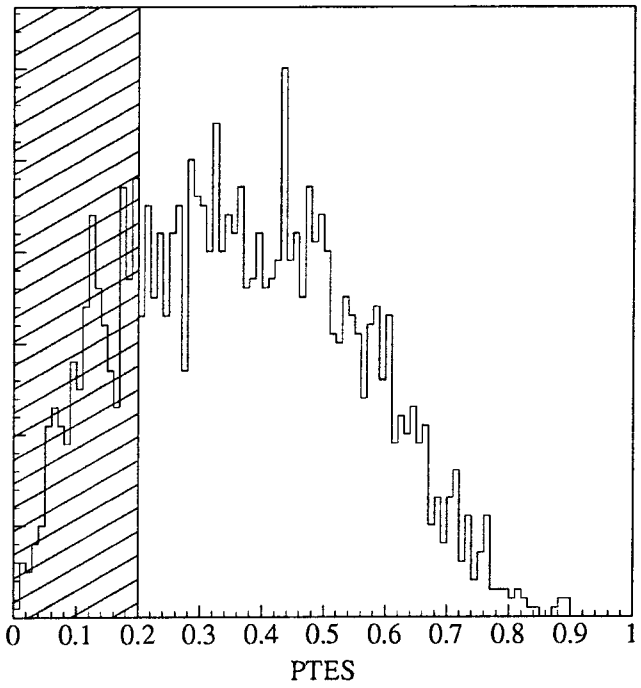

Figure 7.27 The PTES distribution for 10,000 Monte Carlo generated $e\mu$ events.

of event most probably derives from two-photon background processes (see page 82). We see that placing the minimum PTES at 0.4, as given in Table 7.2, would exclude these events.

The method above yields only one event for all the other decay modes. This implies that the two-photon backgrounds are low for those modes, but prevents us from establishing minima for PTES to distinguish backgrounds. It is, however, possible to study the PTES distribution for events having $Q_1 + Q_2 = 0$.

Figure 7.26 shows a comparison between the PTES distributions for such events for (a) ee, (b) $\mu\mu$, and (c) all other event types grouped together. The events included passed all selection criteria up to and including the track identification and it was necessary to group together all event types other than ee and $\mu\mu$ to provide enough

statistics to set a minimum.*

For each group one observes a peak at zero with a positive tail. In order to establish PTES minima we estimated where the tail approached zero and set the minima at that point. This method confirms the PTES minimum at 0.4 for the ee mode and can be used to set the minima for the other channels as well. The dashed lines in the figure show the values of PTES_{min} chosen, corresponding to Table 7.2.

Figure 7.27 shows the distibution of PTES for 10,000 $e\mu$ events generated by Monte Carlo at an energy of 3.554 GeV. 79% of the events which pass the previous selection criteria also pass the PTES criterion. As we have observed from Figures 7.25 and 7.26 the vast majority of background events will fail this criterion, greatly increasing the signal-to-background ratio.

Note that the PTES selection criteria also solve the problems mentioned on page 84 associated with radiative background events. Missing momentum along the beam pipe implies $|\vec{p}^{\,T}| \approx 0$ and, since p_1 and p_2 cannot be approximately equal in size to the beam energy due to the momentum selection criteria, this implies that PTES ≈ 0. Radiative events have either $\vec{p_1} \approx -\vec{p_2}$ implying $|\vec{p}^{\,T}| \approx 0$ which again yields PTES ≈ 0 or have a detectable photon in the shower counter. Both types of events would fail our selection criteria.

Figure 7.28 shows the value for κ, the product of the branching fractions and the efficiency, as a function of $E - 2m_\tau$ throughout the range of interest. κ is estimated from the number of events identified from a Monte Carlo model of all tau decays where branching fractions for the various decay channels were fixed at their best estimates

---

$\star$ Noting the logarithmic scale, the numbers of events are much larger for the ee and $\mu\mu$ modes in comparison to any other single event type. This is due to the large cross section of the two-photon process $e^+e^- \rightarrow e^+e^-e^+e^-$ and of radiative Bhabha and di-muon production.

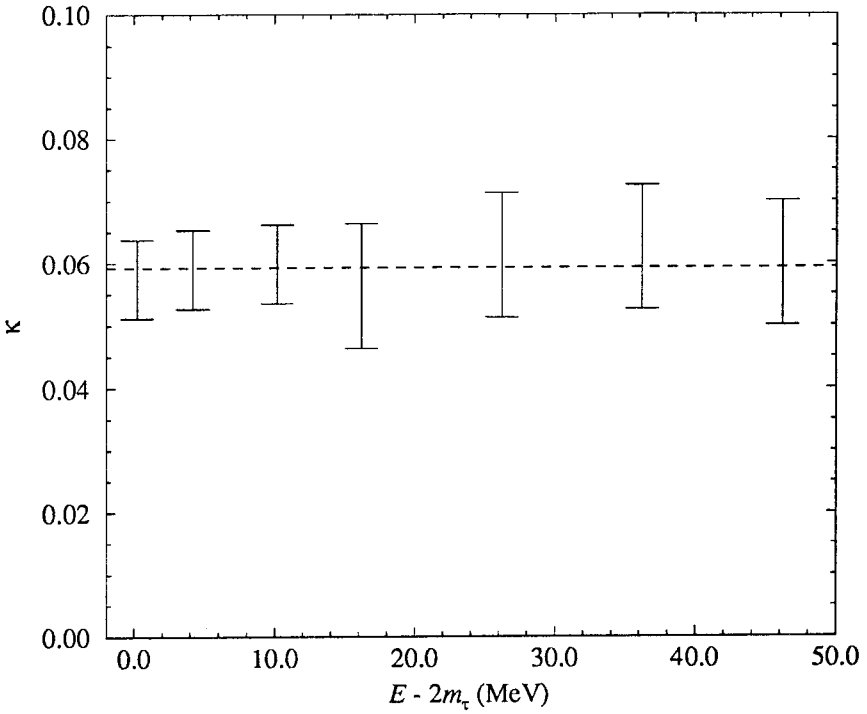

Figure 7.28 κ as a function of $E - 2m_\tau$ for $m_\tau = 1776.9$ MeV.

from the Review of Particle Properties.[66] A fit to a constant value for κ is depicted by the dashed line in the figure. It yields $\kappa = 0.059 \pm 0.003$.

Part IV
Results

"It is one thing to show a man that he is in an error,
And another to put him in possession of truth."

John Locke
An Essay concerning Human Understanding

Chapter 8 Results

Section 8.1 During the Search

The search was carried out in accordance with the algorithm shown on page 39, using $m_\tau^0 = 1784.1$ MeV, $\alpha = 0.04$ MeV/nb^{-1}, and $\mu_{\rm exp} = m_\tau^0$, with the exception of search point 3 which, due to a misunderstanding, was taken at a lower energy. The results are shown in Table 8.1.

Search Point	Energy (GeV)	Energy Spread (MeV)	Integrated Luminosity (nb^{-1})	Number of $e\mu$ Events
1	3.56838	1.34	245.8	2
2	3.56198	1.33	248.9	1
3	3.54418	1.36	232.8	0
4	3.55314	1.37	323.0	0
5	3.55698	1.44	322.5	2
6	3.55190	1.43	296.9	0
7	3.55350	1.47	384.0	0
8	3.55396	1.47	360.8	1
9	3.55290	1.44	794.1	0
10	3.55324	1.40	1109.1	1
11	3.59902	1.44	499.7	5
12	3.57910	1.43	250.0	2

Table 8.1 Results of the search using the $e\mu$ mode.

Note that the decision to move to a different energy was taken while data was still

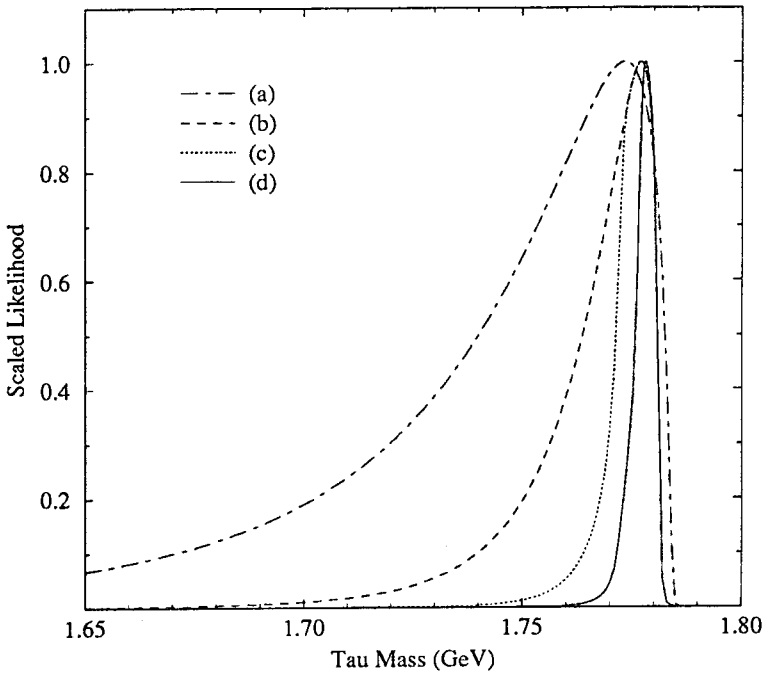

Figure 8.1 The likelihood after search points (a) 1, (b) 2, (c) 3, and (d) 4.

being taken at the present energy. Hence the integrated likelihood and, to a lesser extent, the numbers of events may be different from those used at the time of the decision.

The search points designated 11 and 12 are the extra data taken at higher energy in order to better measure κ^*. Note that the last two points of the true search (points 9 and 10) acquired far more than the standard ≈ 250 nb^{-1} integrated luminosity without the energy changing. This is because the likelihood had become very narrow and hence the peak very well defined. The algorithm predicted a change of less than the stepsize s and we continued to accumulate data at that point.

The progression of the likelihood with integrated luminosity is shown in Figures 8.1–8.3. One may again observe that the two higher energy points make negli-

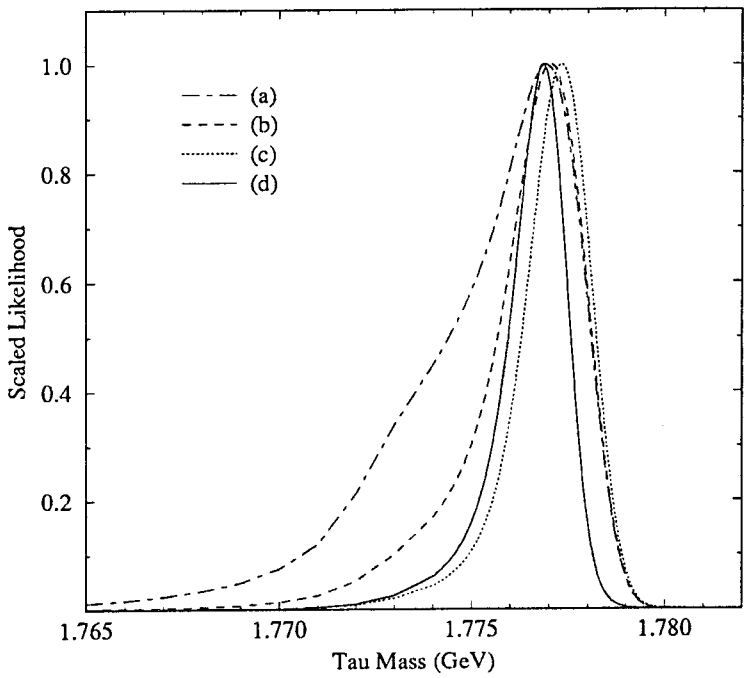

Figure 8.2 The likelihood after search points (a) 5, (b) 6, (c) 7, and (d) 8.

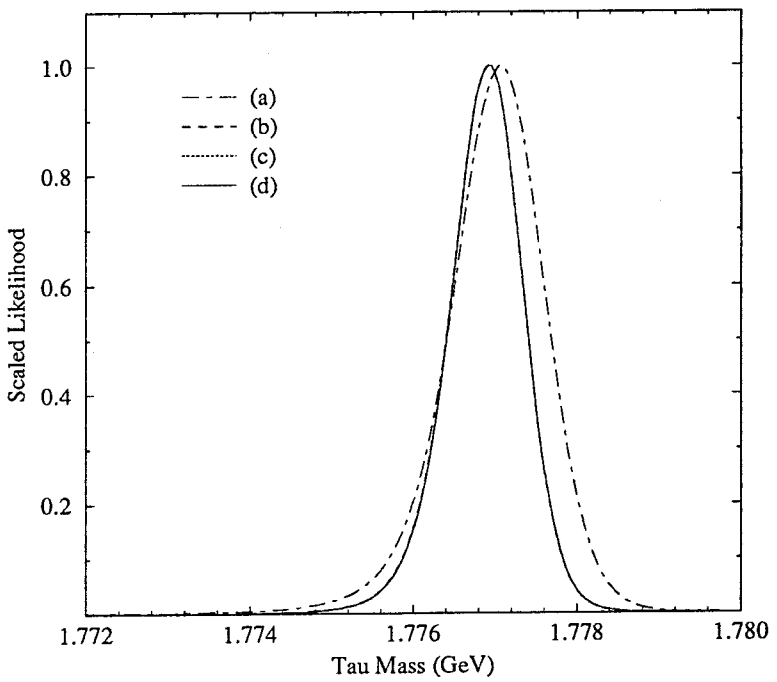

Figure 8.3 The likelihood after search points (a) 9, (b) 10, (c) 11, and (d) 12.

gible difference to the likelihood function: likelihoods (b), (c), and (d) in Figure 8.3 are indistinguishable.

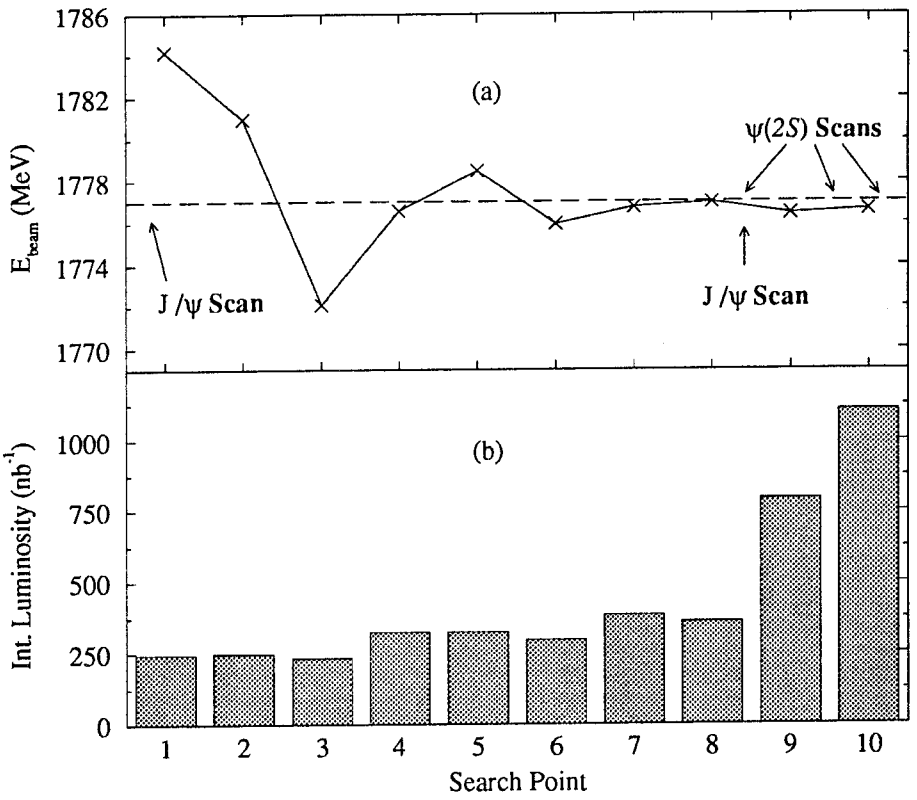

Figure 8.4 (a) The convergence of the predicted mass with each search point. (b) The integrated luminosity accumulated at each search point.

Figure 8.4 shows the chronological change of both the beam energy and the integrated luminosity. It also shows the points at which J/ψ and $\psi(2S)$ scans were taken. The horizontal, dashed line in Figure 8.4(a) is the final value of m_τ for the $e\mu$ mode. The convergence of the algorithm around this value is clearly demonstrated.

Figure 8.5 shows a typical event display for one of the detected $e\mu$ events. One may observe the energy deposited in the shower counter for track 1 and the clear

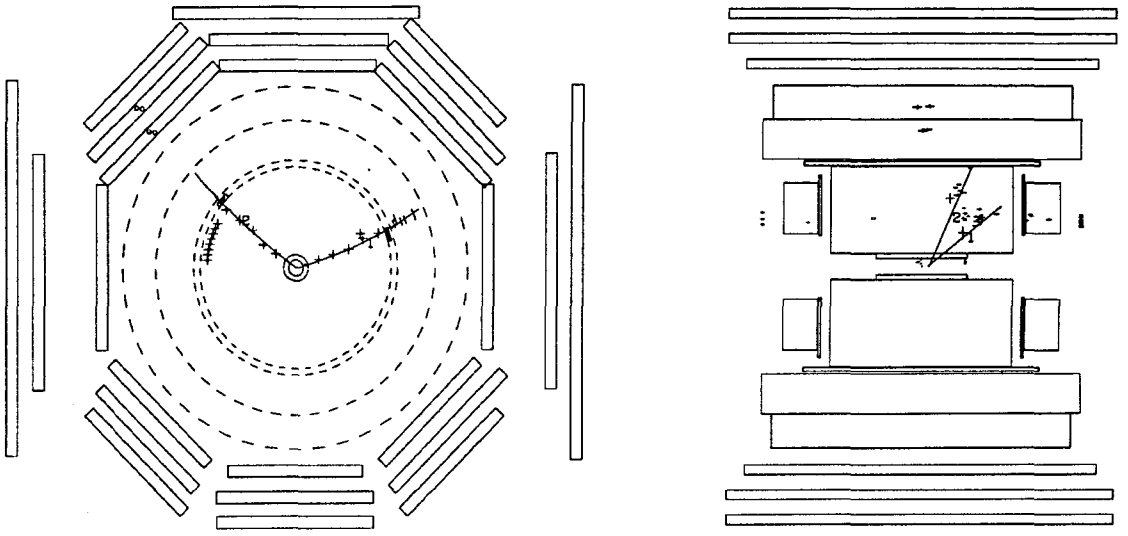

Figure 8.5 A typical $e\mu$ event.

muon hits associated with track 2. There are also some extraneous hits in the main drift chamber unassociated with any track. These were successfully ignored by the reconstruction software and did not affect the event identification.

Section 8.2 After the Search

As discussed in Chapter 6, one finds that the likelihood analysis of the numbers of events, energies, energy spreads, and integrated luminosities described in this thesis introduces small biases in the final value for m_τ dependent on the algorithm under which the search is conducted. An estimate for the uncertainty in the bias of the experiment is included in the systematic uncertainty (see Sections 6.5 and 8.4).

Nevertheless, one is not prevented from re-analysing the data once the search has been conducted and re-calculating the likelihood function based on the new numbers of events.

Such a re-analysis took place with our data, not only to search for $e\mu$ events more

Search Point	Number of Events						
	$n_{e\mu}$	$n_{e\pi}$	n_{ee}	$n_{\mu\pi}$	$n_{\mu\mu}$	$n_{\pi\pi}$	Combined
1	4	3	0	1	0	0	8
2	2	1	0	1	1	0	5
3	0	0	0	0	0	0	0
4	0	0	0	0	0	0	0
5	2	2	0	0	0	0	4
6	0	0	0	0	0	0	0
7	0	1	0	1	0	0	2
8	1	1	0	0	0	0	2
9	0	0	0	0	1	0	1
10	1	2	0	0	0	0	3
11	5	8	2	0	1	3	19
12	1	1	2	1	0	1	6

Table 8.2 Numbers of events found after re–analysis.

thoroughly but also to search for different decay modes. It was necessary during the search to determine the number of $e\mu$ events quickly in order that the accelerator could be set to the new energy and data accumulated. This haste was unnecessary after the search. Re-calibration of the data and better analysis methods based on accumulated data rather than Monte Carlo provide a more accurate estimate of the number of events at each point. The numbers of events found in the re-analysis are reported in Table 8.2. The "Combined" column shows the number of events for all modes added together. The energies, energy spreads and integrated luminosities are identical to those in Table 8.1.

As mentioned in Section 5.1 κ^* and σ_B^* are kept fixed during the search. At the end of the search, however, all three parameters, m_τ^*, κ^*, and σ_B^*, are allowed to vary. A likelihood as a function of all three parameters is generated using the data accumulated at the search energies. The MINUIT[78] program is then used to find the maximum of $L(m_\tau^*, \kappa^*, \sigma_B^*)$. The values of the parameters at this point are the best estimates of those quantities: m_τ, κ, and σ_B respectively.

Using the numbers of $\tau^+\tau^-$ events in Table 8.2 and fitting via the three-dimensional likelihood method described above yields the values for m_τ given in Table 8.3.

Decay Mode	m_τ (MeV)
$e\mu$	1777.01
ee	1785.02
$e\pi$	1776.67
$\mu\mu$	1778.53
$\mu\pi$	1776.53
$\pi\pi$	1785.69
Combined	1776.87

Table 8.3 Fitted values for m_τ.

Section 8.3 Statistical Uncertainties

Statistical uncertainties are estimated via the following method. The three-dimensional likelihood is reduced to a one-dimensional likelihood by fixing κ^* and σ_B^* at their values at the peak of the likelihood. The uncertainty in m_τ is then estimated by defining σ_A^+ and σ_A^- as detailed in Equations (6.5) and (6.6).

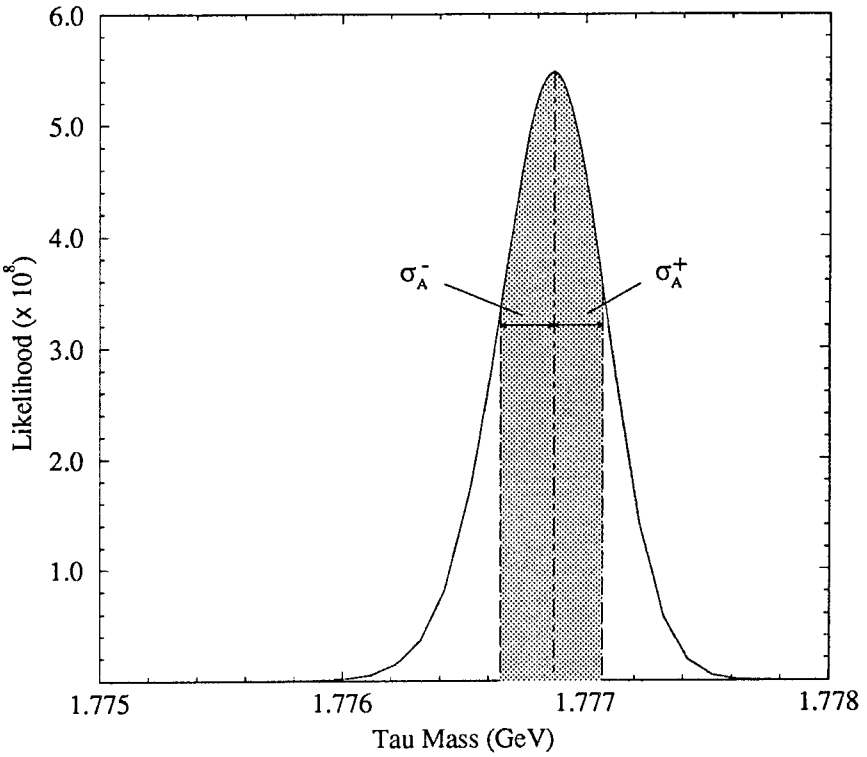

Figure 8.6 The final likelihood function for the combined mode.

Decay Mode	Statistical Uncertainty (MeV)
$e\mu$	$^{+0.36}_{-0.42}$
ee	$^{+2.32}_{-3.47}$
$e\pi$	$^{+0.32}_{-0.44}$
$\mu\mu$	$^{+3.82}_{-3.77}$
$\mu\pi$	$^{+0.68}_{-2.18}$
$\pi\pi$	$^{+2.52}_{-3.42}$
Combined	$^{+0.20}_{-0.22}$

Table 8.4 Statistical uncertainties in m_τ.

The unscaled final likelihood for the combined mode is shown in Figure 8.6 with σ_A^+ and σ_A^- indicated. Table 8.4 shows the statistical uncertainty, calculated in this way, for all the decay modes considered.

Section 8.4 Systematic Uncertainties

There are five sources of systematic uncertainty:

1. Uncertainty in the absolute energy scale with which we measure E_i.
2. Uncertainty in the energy spread Δ_E we assume for the cross section calculation.
3. Uncertainty in the absolute normalization of the cross section curve.
4. Uncertainty in the background σ_B.
5. Uncertainty in the bias of the algorithm used in the search.

The first two of these are independent of which channel we are considering. The next two can be calculated from the three-dimensional likelihood generated after the search is completed for whichever channel or combination of channels is under consideration. The last must be estimated from Monte Carlo simulations of many experiments. All five estimates will be combined in quadrature to produce our final estimate of the systematic uncertainty. Details of each of these sources of uncertainty are given below.

The J/ψ and $\psi(2S)$ Calibrations

Both the absolute energy scale and the energy spread of the BEPC accelerator were calibrated by two scans of the J/ψ resonance and three scans the $\psi(2S)$ resonance taken at convenient intervals during the search (see Figure 8.4). The events counted were those that, within some loose criteria, were considered hadron events, *i.e.*,

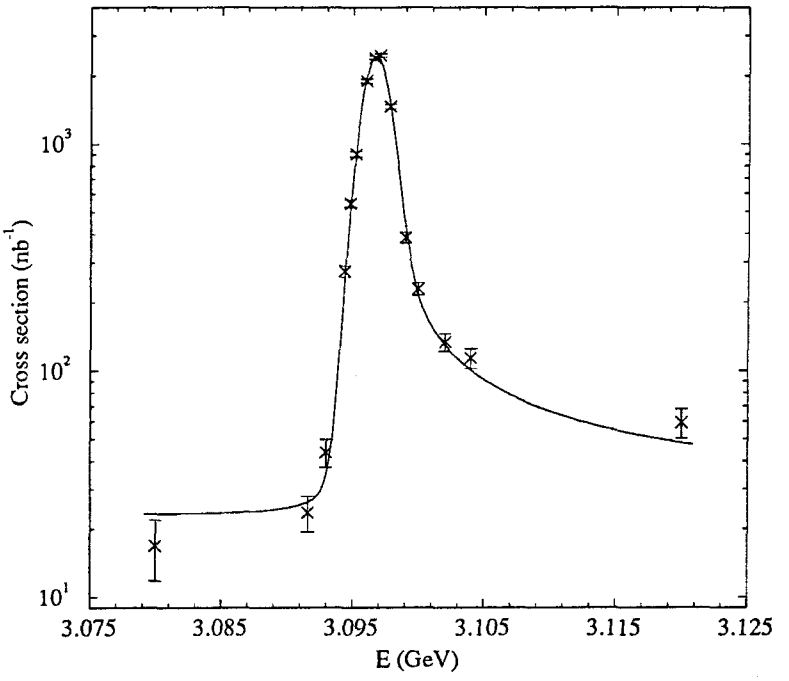

Figure 8.7 A scan of the J/ψ resonance.

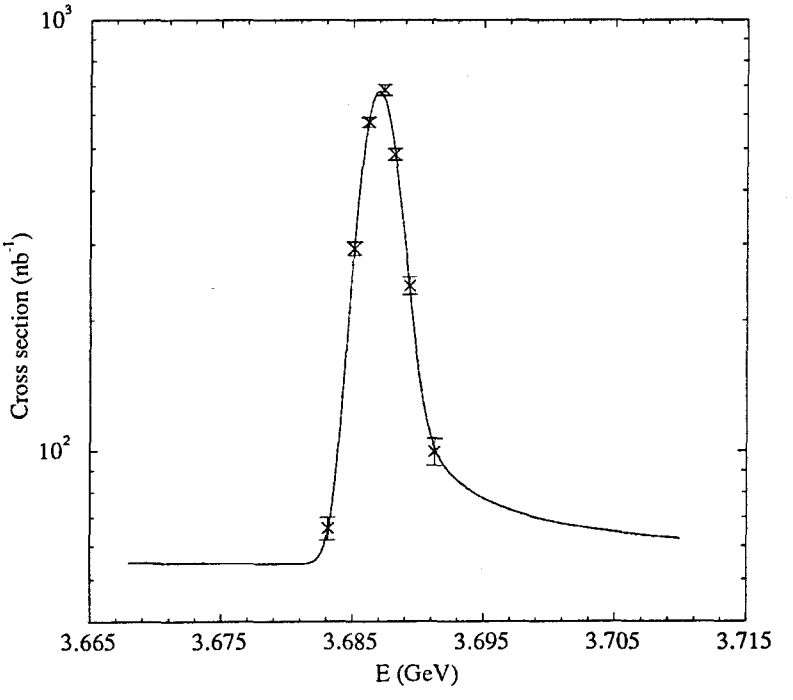

Figure 8.8 A scan of the $\psi(2S)$ resonance.

J/ψ or $\psi(2S) \rightarrow$ hadrons. These were simple, progressive scans of the two energy regions; their energies were not decided via the likelihood method used for the tau threshold search. Figures 8.7 and 8.8 show examples of such scans.

The resonances are independently fitted to their expected theoretical shapes via a three-parameter fit to their respective masses, widths,* and heights. Radiative corrections are taken into account. The results for the mass and width for each of the scans are shown in Tables 8.5 and 8.6.

	Mass (MeV)	Width (MeV)
Scan 1	3097.32 ± 0.02	1.04 ± 0.017
Scan 2	3097.07 ± 0.02	1.20 ± 0.016
Average	3097.20	1.12

Table 8.5 Results of the J/ψ scans.

	Mass (MeV)	Width (MeV)
Scan 1	3687.03 ± 0.03	1.49 ± 0.043
Scan 2	3686.88 ± 0.03	1.34 ± 0.038
Scan 3	3686.74 ± 0.03	1.40 ± 0.024
Average	3686.88	1.41

Table 8.6 Results of the $\psi(2S)$ scans.

Absolute Energy Scale

Assuming a linear relation between the measured energy E_M and the corrected

* Note that the intrinsic widths of the J/ψ and $\psi(2S)$ are 86 and 278 keV respectively. Therefore the width measured here is completely dominated by the centre of mass energy spread Δ_E.

value† E of the form

$$E = T_\psi + (E_M - M_\psi)\left(\frac{T_{\psi'} - T_\psi}{M_{\psi'} - M_\psi}\right), \tag{8.1}$$

one may calculate the systematic uncertainty in the energy scale from the following formula:

$$\begin{aligned}\delta E = \delta E_M\left(\frac{T_{\psi'} - T_\psi}{M_{\psi'} - M_\psi}\right) \oplus \delta T_\psi\left(\frac{M_{\psi'} - E_M}{M_{\psi'} - M_\psi}\right) \oplus \delta T_{\psi'}\left(\frac{E_M - M_\psi}{M_{\psi'} - M_\psi}\right) \\ \oplus \delta M_\psi\left(\frac{(T_{\psi'} - T_\psi)(E_M - M_{\psi'})}{(M_{\psi'} - M_\psi)^2}\right) \oplus \delta M_{\psi'}\left(\frac{(T_{\psi'} - T_\psi)(M_\psi - E_M)}{(M_{\psi'} - M_\psi)^2}\right)\end{aligned} \tag{8.2}$$

where $\oplus$ implies addition in quadrature followed by taking the square root and the notation is explained in Table 8.7.

Quantity	Symbol	Uncertainty (MeV)
BEPC measured centre of mass energy	E_M	0.10
BEPC value for the J/ψ mass	M_ψ	0.18
BEPC value for the $\psi(2S)$ mass	$M_{\psi'}$	0.14
World average value for the J/ψ mass	T_ψ	0.09
World average value for the $\psi(2S)$ mass	$T_{\psi'}$	0.10

Table 8.7 Contributions to the uncertainty in the absolute energy scale at BEPC.

The fits to the masses of the two resonances provide estimates for M_ψ and $M_{\psi'}$. δM_ψ and $\delta M_{\psi'}$ are calculated from the unbiased estimator of the r.m.s. of the measured values $1/(n-1)\sum(M - \bar{M})^2$ where n is the number of samples and M is the

† Corrected energies have been quoted throughout this thesis.

measurement. The values of T_ψ , δT_ψ, $T_{\psi'}$, and $\delta T_{\psi'}$ were known from Reference 4. δE_M was estimated by measuring the maximum difference between the nominal energy and the true energy for any search point. E_M is known to vary between 3.54418 and 3.56838 GeV[‡] (see Table 8.1). The uncertainties are tabulated in Table 8.7.

Using these results we find $\delta E = \pm 0.17$ MeV which implies a contribution to the systematic uncertainty in m_τ of

$$\delta m_\tau = \pm 0.085 \text{ MeV}. \tag{8.3}$$

Energy Spread

Δ_E was determined by a fit to

$$\Delta_E = (A\bar{I} + B)(CE^2 + D) \tag{8.4}$$

where $\bar{I}$ is the average beam current and A, B, C, and D are fitted to the beam current measurements and to measurements of the energy spreads at the J/ψ and $\psi(2S)$ resonances from Tables 8.5 and 8.6. Uncertainties in the values of the fit parameters lead to an uncertainty in Δ_E of ± 0.08 MeV. As shown in Figure 8.9 this implies a contribution to the systematic uncertainty in m_τ of

$$\delta m_\tau = \pm 0.02 \text{ MeV}. \tag{8.5}$$

Absolute Normalization and Background

The absolute normalization of the cross section is the coefficient of σ in Equation (5.3), *i.e.*, $\kappa^* \mathcal{L}_i$. We can establish the uncertainty in m_τ, δm_τ, due to the absolute normalization by estimating uncertainties in the κ, the value of κ^* at the peak of the

‡ Any value for E_M in this interval may be used with negligible effect on δE.

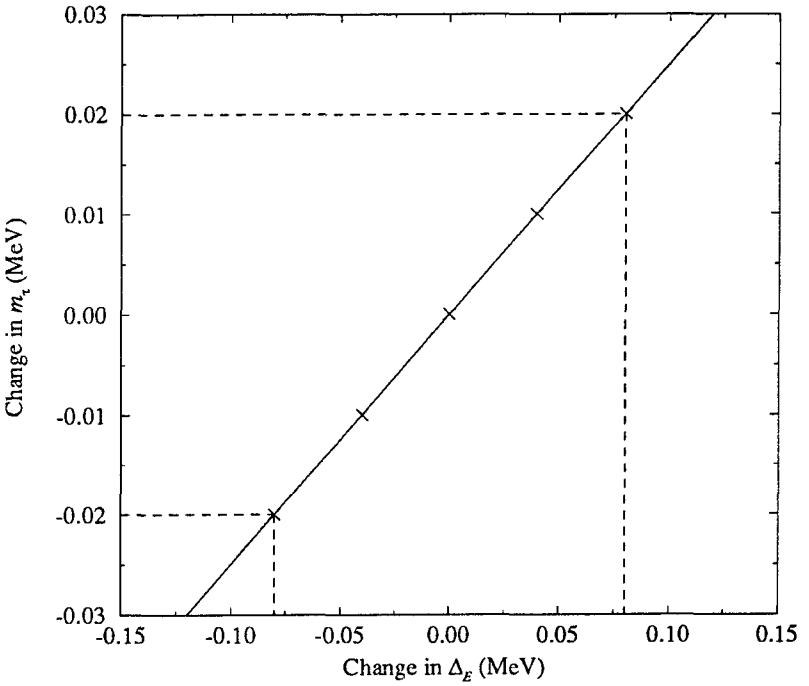

Figure 8.9 Showing the variation in m_τ with changes in Δ_E.

three-dimensional likelihood. Any uncertainty in the overall scale for $\mathcal{L}_i$ is transferred by means of this fit into uncertainties in κ.

The MINUIT program is then used again to estimate the uncertainties in κ via the MINOS routine keeping all other parameters fixed at their values at the peak of the three-dimensional likelihood. These uncertainties and the corresponding uncertainties in m_τ are reported in Table 8.8.

A similar analysis is presented for the background σ_B. The uncertainties are again estimated using MINOS keeping all parameters other than σ_B^* fixed at their values at the peak of the three-dimensional likelihood. Note that fit to the background was constrained to the physical region $\sigma_B \geq 0$. Table 8.9 shows the fits to σ_B, the uncertainty in σ_B, and the corresponding uncertainty in m_τ for the various modes.

Decay Mode	κ ($\times 100$)	δm_τ (MeV)
$e\mu$	$1.05^{+0.29}_{-0.24}$	$^{+0.16}_{-0.20}$
ee	$0.60^{+0.35}_{-0.25}$	$^{+1.03}_{-0.91}$
$e\pi$	$1.12^{+0.28}_{-0.24}$	$^{+0.12}_{-0.24}$
$\mu\mu$	$0.13^{+0.15}_{-0.09}$	$^{+15.88}_{-2.93}$
$\mu\pi$	$0.22^{+0.13}_{-0.09}$	$^{+0.35}_{-0.64}$
$\pi\pi$	$0.62^{+0.36}_{-0.26}$	$^{+2.38}_{-0.96}$
Combined	$3.15^{+0.47}_{-0.42}$	$^{+0.09}_{-0.10}$

Table 8.8 Uncertainty in m_τ due to absolute normalization of the cross section.

Decay Mode	σ_B (pb)	δm_τ (MeV)
$e\mu$	$0^{+0.39}_{-0}$	$^{+0.26}_{-0}$
ee	$0^{+0.12}_{-0}$	$^{+0.04}_{-0}$
$e\pi$	$0^{+0.49}_{-0}$	$^{+0.22}_{-0}$
$\mu\mu$	$0.30^{+0.36}_{-0.20}$	$^{+12.37}_{-2.39}$
$\mu\pi$	$0^{+0.35}_{-0}$	$^{+1.89}_{-0}$
$\pi\pi$	$0^{+0.12}_{-0}$	$^{+0.13}_{-0}$
Combined	$0^{+0.60}_{-0}$	$^{+0.14}_{-0}$

Table 8.9 Uncertainty in m_τ due to background.

Bias of the Algorithm

Since the third search point was taken at an energy which did not follow the algorithm put forward on page 39, we cannot simply subtract the value of the bias from the

previous fit to m_τ. Instead we find the variation in the bias between several algorithms similar to the one used and include this variation in bias in the systematic uncertainty.

F. C. Porter studied these effects in Reference 75 and concluded that an estimate of the uncertainty in m_τ due to variation in the bias over a suitable range of algorithms was

$$\delta m_\tau = \pm 0.1 \text{ MeV} \tag{8.6}$$

for the driving ($e\mu$) mode, the non-driving modes, and for the combined mode.

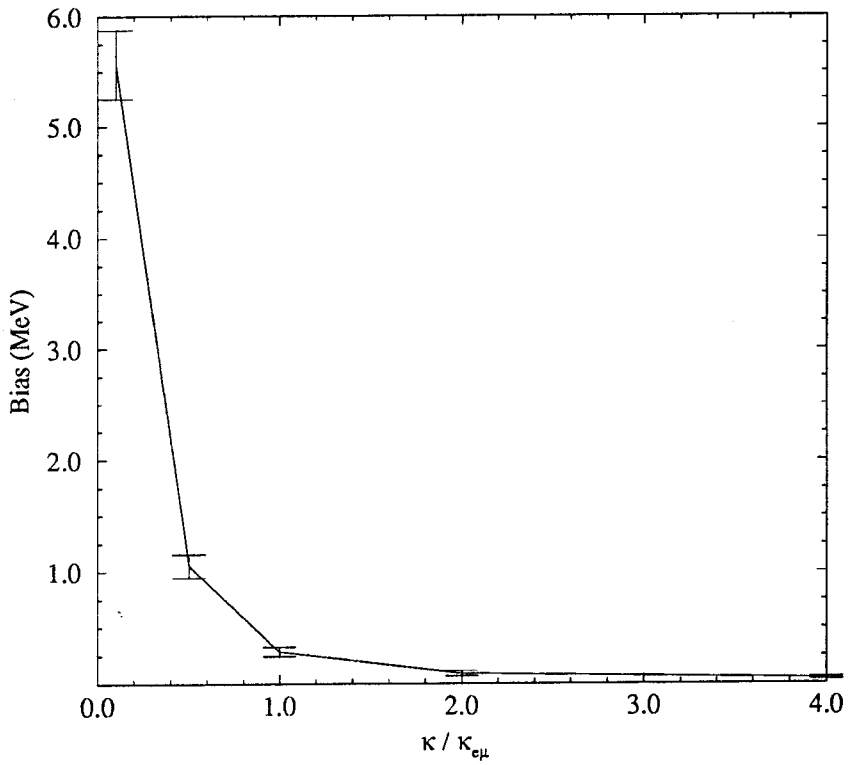

Figure 8.10 Showing the variation in b as a function of $\kappa/\kappa_{e\mu}$ for a non-driving mode.

Figure 8.10 shows the variation of the expected bias with $\kappa/\kappa_{e\mu}$, the ratio of the true efficiency-branching-fraction product for the non-driving mode in question

to that for the $e\mu$ mode. For the modes where relatively small numbers of detected events are expected, there is a large correction which should be subtracted from the estimated value for m_τ independent of the variation between algorithms. The result of this thesis depends solely on the combined mode which has a theoretical expectation for $\kappa/\kappa_{e\mu}$ of approximately four. This implies that there will be negligible effect on that mode and I will not attempt to take this effect into account for the other modes.

Section 8.5 Final Results

Table 8.10 shows the final results for m_τ for all considered decay channels. The statistical uncertainties are given first and systematic uncertainties second. All of the sources of statistical and systematic uncertainty mentioned in the preceding sections, with the exception of the bias offset mentioned above, have been included.

Decay Mode	Fitted value for m_τ (MeV)
$e\mu$	$1777.01^{+0.36+0.34}_{-0.42-0.25}$
ee	$1785.02^{+2.32+1.05}_{-3.47-0.93}$
$e\pi$	$1776.67^{+0.32+0.29}_{-0.44-0.28}$
$\mu\mu$	$1778.53^{+3.82+20.17}_{-3.77-3.78}$
$\mu\pi$	$1776.53^{+0.68+1.93}_{-2.18-0.66}$
$\pi\pi$	$1785.69^{+2.52+2.38}_{-3.42-0.97}$
Combined	$1776.87^{+0.20+0.22}_{-0.22-0.18}$

Table 8.10 A comparison of the final results for m_τ.

The value for the combined channel, *i.e.*, where the events from all modes are

used to estimate m_τ, is

$$m_\tau = 1776.87^{+0.20+0.22}_{-0.22-0.18} \text{ MeV}. \tag{8.7}$$

In order to estimate of the quality of the fit the likelihood ratio Λ may be calculated:

$$\Lambda = \prod_{i=1}^{N} \frac{P(n_i\,;\mu_i)}{P(n_i\,;n_i)} = \prod_{i=1}^{N} e^{n_i-\mu_i} \left(\frac{\mu_i}{n_i}\right)^{n_i} \tag{8.8}$$

where $P(n_i\,;\mu_i)$ is defined in Equation (5.2) and $(\mu_i/n_i)^{n_i} = 1$ for $n_i = 0$ by definition.

In the limit of large statistics the quantity $-2\ln\Lambda$ would obey a χ^2 distribution for 9 degrees of freedom and hence is a measure of the quality of the fit.[79] For the combined mode we find

$$-2\ln\Lambda = 4.03. \tag{8.9}$$

If this value were a χ^2 this would imply that the functional form of the cross section form fits the data with a confidence level greater than 90%.

Part V
Conclusions

"More are men's ends mark'd than their lives before:
The setting sun, and music at the close,
As the last taste of sweets, is sweetest last,
Writ in remembrance more than things long past."

William Shakespeare
Richard II

Chapter 9 Conclusions

Section 9.1 Comparisons of Values for m_τ

A comparison of the final results for m_τ for all considered decay modes was presented in Table 8.10. One may observe that, with the exception of the ee and $\pi\pi$ modes for which no events were observed during the likelihood-driven part of the search, the values for m_τ are in agreement with one another and with the combined mode within uncertainties. The values for the ee and $\pi\pi$ modes may be explained by the bias offset effect mentioned in section 8.4. The uncertainties for all individual modes except $e\mu$ and $e\pi$ are large due mainly to the large uncertainties in the value of κ estimated from the fit. Nevertheless, the result for the combined mode represents the most accurate measurement of the mass of the tau lepton to date.

The result for the tau mass published previously by the BES collaboration,[68] $1776.9^{+0.4}_{-0.5} \pm 0.2$ MeV, was based solely on the $e\mu$ mode. For comparison, the value from this thesis based solely on the $e\mu$ mode is:

$$m_\tau(e\mu) = 1777.01^{+0.36+0.34}_{-0.42-0.25} \text{ MeV}. \tag{9.1}$$

The final value for the mass of the tau lepton as measured in this thesis is that given for the combined channel in Equation (8.7):

$$m_\tau = 1776.87^{+0.20+0.22}_{-0.22-0.18} \text{ MeV}. \tag{9.2}$$

This value is in good agreement with the most recent results published by other collaborations: the ARGUS and CLEO collaborations found values for m_τ of $1776.3 \pm 2.4 \pm 1.4$[80] and $1777.8 \pm 0.7 \pm 1.7$ MeV[81] respectively.

Comparing the final result with the 1992 world average, $1784.1^{+2.7}_{-3.6}$ MeV, the uncertainties have been decreased by a factor of approximately ten and the central value is lower by two standard deviations.

Section 9.2 Lepton Universality Revisited

Using the final value for m_τ from the previous section one may consider the lepton universality disagreement discussed in Section 1.3. Figure 9.1 shows the region of the τ_τ–B^e_τ plane consistent with the value of m_τ quoted in Equation (9.2) where m_τ is allowed to vary by plus or minus one standard deviation. The point with error bars shows the most recent results[82] for τ_τ and B^e_τ, $(292.2 \pm 2.4) \times 10^{-3}$ ps and $17.90 \pm 0.16\%$ respectively.

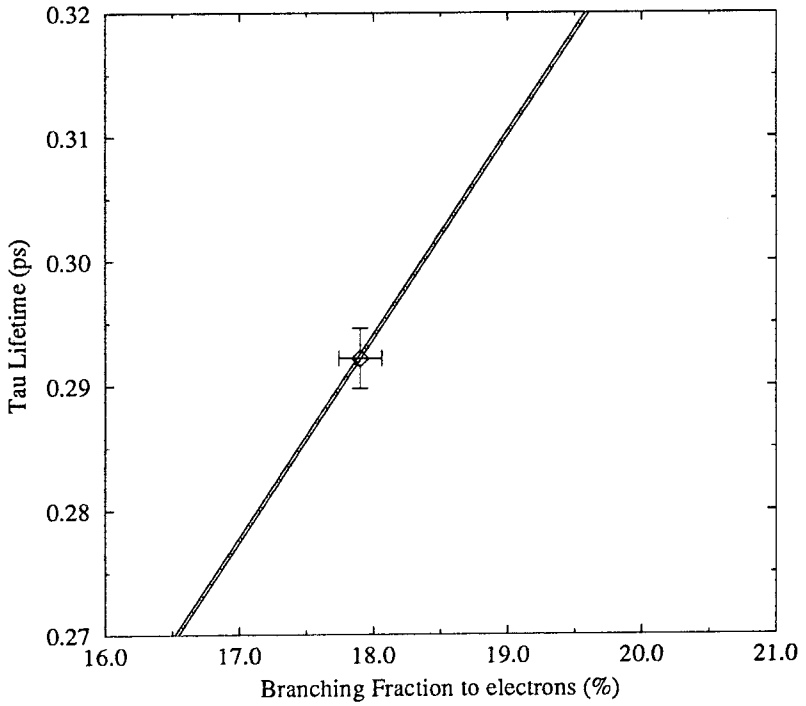

Figure 9.1 The variation of τ_τ with B^e_τ for $m_\tau = 1776.87^{+0.20+0.22}_{-0.22-0.18}$ MeV compared with the most recent results.

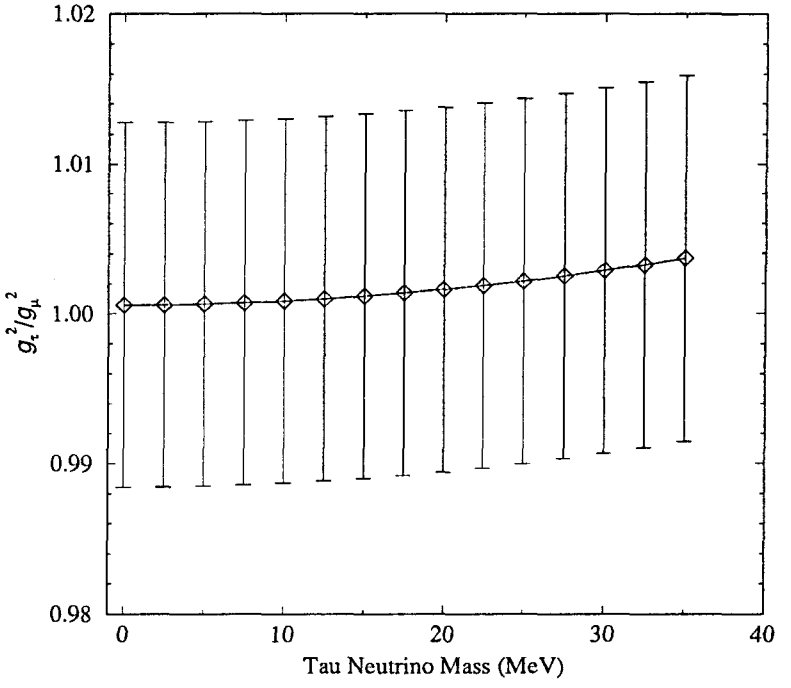

Figure 9.2 g_τ^2/g_μ^2 as a function of tau neutrino mass.

Figure 9.2 shows the value for g_τ^2/g_μ^2 as a function of the tau neutrino mass. The value for a massless neutrino,

$$g_\tau^2/g_\mu^2 = 1.001 \pm 0.012, \tag{9.3}$$

is now my best estimate. Note that the contribution of m_τ to the uncertainty in g_τ^2/g_μ^2 has been reduced from 38% to approximately 5%. Also, since g_τ^2/g_μ^2 is now greater than one, a massive tau neutrino would decrease the agreement with the Standard Model.

On comparing Figure 9.1 with Figure 1.2 and considering the value for g_τ^2/g_μ^2 above, one may see that we now have excellent agreement with the Standard Model including the lepton universality hypothesis.

Part VI
Appendices

"Merely corroborative detail, intended to give artistic verisimilitude to an otherwise bald and unconvincing narrative."

W. S. Gilbert
The Mikado

Appendix A The Code

Section A.1 mctau

The code used to generate a large number of experiments with the number of detected events chosen randomly from the appropriate Poisson distribution is called `mctau`. It is written in the C language and is available via anonymous ftp from `ftp.cithep.caltech.edu` in the file `pub/ljones/mctau.tar.gz`. Installation requires access to `CERNLIB` routines, in particular `HBOOK`.[83] The wrapper routines for calling the `HBOOK` routines from C are architecture dependent and may need re-writing.

The usage message for `mctau` is given below:

```
mctau   [-D output_directory] [-o output_file] [-n ntuple_file]
        [-m true tau mass] [-i initial energy] [-N # expts]
        [-t total int. lum.] [-B # bins per expt] [-d driving_mode]
        [-k kappa(driving mode)] [-b bkgnd_xsec(driving mode)]
        [-L like. low limit (GeV)] [-H like. high limit (GeV)]
        [-S like. step (MeV)] [-p precision (MeV)]
        [-R ratio to peak] [-A median area to width ratio]
        [-P peak area to width ratio] [-M energy_method]
        [-O offset] [-z zerodelt] [-x max_step_size]
        [-g gaussian_mean] [-G gaussian_expansion_rate]
        [-c prog. scan step (MeV)] [-r binary scan range (MeV)]
        [-s random number seed]
```

Reasonable defaults are provided for all quantities. However should you want to override the defaults the following lists the purpose of each flag.

The `-D` argument is the output directory for both the output file and the ntuple file. Using a dot to mean current directory is acceptable.

The `-o` and `-n` arguments are the output files for the text and for the ntuple respectively.

The `-m` argument defines the true mass m_τ^{true}. The default is 1776.9 MeV.

The `-i` argument describes the initial energy = $2m_\tau^0$. The default is 3.5682 GeV.

The `-N` argument describes how many experiments to run. The default is 1.

The `-t` and `-B` arguments control the total integrated luminosity and the number of bins (search points) in the search respectively. The last two bins are automatically set to the values used for the higher energy points provided the number of bins is at least two. The defaults are 5 pb^{-1} and 19 respectively.

The `-d` argument describes the driving mode: 0 through 7 imply the $e\mu$, $e\pi$, $\mu\pi$, ee, $\mu\mu$, $\pi\pi$, $e\rho$, and $\mu\rho$ modes respectively. At the moment only the $e\mu$ mode is implemented.

The `-k` and `-b` arguments provide a way to override the default values for κ^* and σ_B^* for the driving mode if necessary. The defaults are 0.008889 and 0.024 pb respectively.

The `-L`, `-H`, `-S`, and `-p` flags are used to define the points at which the likelihood function is calculated. The `-L` and `-H` arguments yield the lower and upper limits for m_τ^*. The argument to the `-S` flag denotes the size of the interval between each likelihood evaluation point. Around the peak of the likelihood this interval is decreased in size. The `-p` argument controls this size. The present defaults are 1.5 GeV, 1.8 GeV, 1 MeV, and 0.05 MeV respectively.

The `-R` argument controls the ratio between the likelihood at the points where σ^+ and σ^- are evaluated and the likelihood at the peak. The default is $e^{-\frac{1}{2}}$.

The `-A` argument controls the fraction af the area underneath the likelihood between the median and the points at which σ_B^+ and σ_B^- are evaluated. The default is 0.3413.

The `-P` argument controls the ratio of the area between $m_\tau^{\rm peak}$ and $m_\tau^{\rm peak} + \sigma_A^+$ to that above $m_\tau^{\rm peak}$. The default is 0.6826. The ratio of the area between $m_\tau^{\rm peak} - \sigma_A^-$ and the peak to the total area below the peak is the same.

The `-M` argument controls how the next energy at which searching will take place is chosen. Respectively, 0 through 4 represent the unlimited energy step, the limited energy step, the expanding Gaussian, the progressive search, and the binary search algorithms.

The `-O` argument is the offset δ. The default is 0.3 MeV.

The `-s` argument is the seed for the random number generation. The default is 1234567. If an argument of less than or equal to zero is passed a time dependent seed will be generated.

The remaining flags have arguments describing the various algorithms which were mentioned in Chapter 6. See the `mctau.README` file in the installation package for details.

Section A.2 `runtau`

The code used to generate the one–dimensional likelihood function of m_τ given a single set of energies, energy spreads, integrated luminosities, and numbers of detected $\tau^+\tau^-$ events is called `runtau`. It too is written in C and is available via anonymous ftp from the same file as `mctau`.

The usage message is listed below:

```
runtau  [-i input_file] [-o output_file] [-l likelihood_file]
        [-D output dir] [-n # bins] [-d driving_mode]
        [-k kappa(driving mode)] [-b bkgnd_xsec(driving mode)]
        [-L like. low limit (GeV)] [-H like. high limit (GeV)]
        [-S like. step (MeV)] [-p precision (MeV)]
        [-R ratio to peak] [-A median area to width ratio]
        [-P peak area to width ratio] [-N scale likelihood]
```

The flags for `runtau` have identical functionality to those in `mctau` except for the following.

The `-i` argument names the input file which, at its most basic, is a file containing four numbers per line. These four will be interpreted as centre of mass energy E in GeV, energy spread Δ_E in MeV, number of $\tau^+\tau^-$ events n (an integer), and integrated luminosity $\mathcal{L}$ in nb^{-1} respectively. The number of lines implies the number of search points. Any line starting with the character # will be ignored. Any character which is not a number, the period, the plus sign, or the minus sign between the four numbers will be ignored, hence exponential notation is not supported at this time. Also any number after the fourth will be ignored.

The `-l` argument is the name of the file to which you want the final likelihood outputted. The likelihood file consists of comma–separated pairs—m_τ^*, L—one per line.

The `-n` argument controls the number of bins to be used. This argument must be smaller than or equal to the number of bin description lines in the input file.

The `-N` flag takes no argument. If it is present the outputted likelihood is scaled to a height of 1, otherwise the likelihood is outputted at its natural height.

Bibliography

1. The LEP Collaborations, *Phys. Lett.* **276B** (1992), 247.
2. G. S. Abrams *et al.*, *Phys. Rev. Lett.* **63** (1989), 2173.
3. Fermilab **PUB–94/097–E**.
4. K. Hikasa *et al.*, "Review of Particle Properties," *Phys. Rev.* **D45** (1992) Part II.
5. R. Abela *et al.*, *Phys. Lett.* **146B** (1984), 431.
6. H. Albrecht *et al.*, *Phys. Lett.* **202B** (1988), 149.
7. B. C. Barish & R. Stroynowski, *Phys. Rep.* **157** (1988), 13.
8. W. J. Marciano & A. Sirlin, *Phys. Rev. Lett* **61** (1988), 1815.
9. Y. S. Tsai, *Phys. Rev.* **D4** (1971), 2821. Erratum *ibid.* **D13** (1976) 771.
10. For a description of the Mark I detector see, *e.g.*, John E. Zipse, "Quantum Electrodynamics with the Spear Magnetic Detector," Ph.D. Thesis, **LBL–4281**, (1975).
11. M. L. Perl *et al.*, *Phys. Rev. Lett.* **35** (1975), 1489.
12. M. Cavalli–Sforza *et al.*, *Phys. Rev. Lett.* **36** (1976), 558.
13. J. Burmester *et al.*, *Phys. Lett.* **68B** (1977), 297.
14. G. Alexander *et al.*, *DESY Rept.* **77/78** (1977).
15. A. Barbro–Galtieri *et al.*, *Phys. Rev. Lett.* **39** (1977), 1058.
16. R. Brandelik *et al.*, *Phys. Lett.* **70B** (1977), 125.

17. M. L. Perl *et al.*, *Phys. Lett.* **63B** (1976), 466.

18. G. J. Feldman *et al.*, *Phys. Rev. Lett.* **38** (1977), 117.

19. J. Burmester *et al.*, *Phys. Lett.* **68B** (1977), 301.

20. M. L. Perl *et al.*, *Phys. Lett.* **70B** (1977), 487.

21. R. Brandelik *et al.*, *Phys. Lett.* **73B** (1978), 109.

22. W. Bartel *et al.*, *Phys. Lett.* **77B** (1978), 331.

23. W. Bacino *et al.*, *Phys. Rev. Lett.* **41** (1978), 13.

24. G. Alexander *et al.*, *Phys. Lett.* **81B** (1979), 84.

25. G. Feldman *et al.*, *Phys. Rev. Lett.* **49** (1982), 66.

26. W. T. Ford *et al.*, *Phys. Rev. Lett.* **82** (1982), 106.

27. H. Behrend *et al.*, *Nucl. Phys.* **B211** (1983), 369.

28. J. Jaros *et al.*, *Phys. Rev. Lett.* **51** (1983), 955.

29. M. Althoff *et al.*, *Phys. Lett.* **141B** (1984), 264.

30. E. Fernandez *et al.*, *Phys. Rev. Lett.* **54** (1985), 1624.

31. H. R. Band *et al.*, *Phys. Rev. Lett.* **59** (1987), 415.

32. C. Bebeck *et al.*, *Phys. Rev.* **D35** (1987), 2747.

33. C. Bebeck *et al.*, *Phys. Rev.* **D36** (1987), 690.

34. S. Abachi *et al.*, *Phys. Rev. Lett.* **59** (1987), 2519.

35. H. Albrecht *et al.*, *Phys. Lett.* **199B** (1987), 580.

36. D. Amidei *et al.*, *Phys. Rev.* **D37** (1988), 1750.

37. N. Qi, "Measurement of the Tau Lepton Lifetime," Ph.D. thesis, **UMI–87–23495–mc** (1987), 78pp.

38. P. Abreu *et al.*, *Phys. Lett.* **267B** (1991), 422.

39. P. D. Acton *et al.*, *Phys. Lett.* **273B** (1991), 355.

40. D. Decamp *et al.*, *Phys. Lett.* **279B** (1992), 411.

41. M. Battle *et al.*, *Phys. Lett.* **291B** (1992), 488.

42. D. Buskulic *et al.*, *Phys. Lett.* **297B** (1992), 432.

43. S. Behrends *et al.*, *Phys. Rev.* **D32** (1985), 2468.

44. S. D. Holzner, "The Tau-Neutrino Mass and the Michel Parameter in Tau Decay," Ph.D Thesis, **UMI-87-15600-mc**, 1987, 111pp.

45. H. Janssen *et al.*, *Phys. Lett.* **228B** (1989), 273.

46. H. Albrecht *et al.*, *Phys. Lett.* **246B** (1990), 278.

47. D. C. Drewer, "Measurement of the Michel Parameter for Leptonic Tau Decay," Ph.D. Thesis, **JHU–HEP–90–0928**, (1990), 112pp.

48. H. Albrecht *et al.*, *Phys. Lett.* **316B** (1993), 608.

49. E. W. Kolb & T. J. Goldman, *Phys. Rev. Lett.* **43** (1979), 897.

50. R. R. Sharma & N. K. Sharma, *Phys. Rev.* **D29** (1984), 1533.

51. H. Albrecht *et al.*, *Phys. Lett.* **163B** (1985), 404.

52. G. B. Mills *et al.*, *Phys. Rev. Lett.* **54** (1985), 624.

53. B. G. Bylsma, "Tau Decays to Five and Seven Charged Particles and the Tau Neutrino Mass," Ph.D. Thesis, **PU–87–606**, 1987, 103pp.

54. D. A. Bryman & C. E. Picciotto, *Phys. Rev.* **D36** (1987), 3514.

55. S. E. Csorna *et al.*, *Phys. Rev.* **D35** (1987), 2747.

56. A. J. Weinstein & R. Stroynowski, *Annu. Rev. Nucl. Part. Sci.* **43** (1993), 457.

57. T. N. Truong, *Phys. Rev.* **D30** (1984), 1509.

58. P. Burchat *et al.*, *Phys. Rev.* **D35** (1987), 27.

59. J. J. Gomez–Cadenas, C. A. Heusch & A. Seiden, *Particle World* (1989), 1.

60. K. G. Hayes, "Status of the One-Prong Problem," **SLAC–PUB–5061** (1989), 23pp.

61. J. Repond, "The Tau One-Prong Problem and Recent Measurements by the HRS Collaboration," **ANL–HEP–CP–89–53**, 1989, 10pp.

62. P. D. Acton *et al.*, *Phys. Lett.* **273B** (1991), 355.

63. P. D. Acton *et al.*, *Phys. Lett.* **288B** (1992), 373.

64. D. Decamp *et al.*, *Z. Phys.* **C54** (1992), 211.

65. B. Adeva *et al.*, *Phys. Lett.* **265B** (1991), 451.

66. M. Aguilar-Benitez *et al.*, "Review of Particle Properties," *Phys. Rev.* **D50** (1994) Part I, 1173.

67. M. H. Ye & Z. P. Zheng, "Proceedings of the 1989 International Symposium on Lepton and Photon Interactions at High Energies, Stanford," (1989) 122.

68. J. Z. Bai *et al.*, *Phys. Rev. Lett.* **69** (1992), 3021.

69. D. Bernstein *et al.*, *Nucl. Instr. and Methods* **226** (1984), 301.

70. H. L. Ni *et al.*, *Nucl. Instr. and Methods* **A336** (1993), 542.

71. See, for instance, J. E. Freund, "Mathematical Statistics," 223pp.

72. M. B. Voloshin, "Topics in Tau Physics at a Tau-Charm Factory," **TPI–MINN–89/33–T**, 1989, 8pp.

73. É. A. Kuraev & V. S. Fadin, *Sov. J. Nucl. Phys.* **41**(3) (1985), 466.

74. F. A. Berends & G. J. Komen, *Phys. Lett.* **63B** (1976), 432.

75. F. C. Porter, "Analysis of Statistical Bias in Tau Mass Measurement," BES Collaboration Note 93–013, 1993.

76. L. A. Jones, "A Study of Tau Mass Likelihood Experiments with Large, Negative Errors," BES Collaboration Note 94–002, 1994.

77. KORALB by S. Jadach & Z. Wąs, *Comput. Phys. Commun.* **36** (1985), 191.

78. CERN Program Library Entry **D506**.

79. See, for instance, A. G. Frodesen, O. Skjeggestad, & H. Tøfte, "Probability and Statistics in Particle Physics," 388pp.

80. H. Albrecht *et al.*, *Phys. Lett.* **292B** (1992), 221.

81. R. Balest *et al.*, *Phys. Rev.* **D47** (1993), 3671.

82. T. Skwarnicki, "Summary of Tau Results at the Heavy Flavor Session," presented at the Eighth Meeting of the Division of Particles and Fields of the American Physical Society, 1994.

83. CERN Program Library Entry **Y250**.